Interfacing fluorescent DNA oligonucleotides with graphene oxide and metal oxides: from adsorption to sensing

by

Anand Lopez

A thesis

presented to the University of Waterloo

in fulfilment of the

thesis requirement for the degree of

Doctor of Philosophy

in

Chemistry

Waterloo, Ontario, Canada, 2022

Examining Committee Membership

The following served on the Examining Committee for this thesis. The decision of the Examining Committee is by majority vote.

External Examiner	Dr. Leyla Soleymani Associate Professor, School of Biomedical Engineering, McMaster University, Hamilton, Canada
Supervisor	Dr. Juewen Liu Professor, Department of Chemistry, University of Waterloo, Waterloo, Canada
Internal Member	Dr. Thorsten Dieckmann Associate Professor, Department of Chemistry, University of Waterloo, Waterloo, Canada
Internal Member	Dr. Vivek Maheshwari Associate Professor, Department of Chemistry, University of Waterloo, Waterloo, Canada
Internal-external Member	Dr. Boxin Zhao Professor, Department of Chemical Engineering, University of Waterloo, Waterloo, Canada

Author’s Declaration

This thesis consists of material all of which I authored or co-authored: see Statement of Contributions included in the thesis. This is a true copy of the thesis, including any required final revisions, as accepted by my examiners.

I understand that my thesis may be made electronically available to the public.

Statement of Contributions

The experiments performed in this work were formed by the author and several collaborators. These resulted in the publications outlined in Chapters 2 – 5 and the contributions are summarized below.

The work in Chapter 2 has been published as Anand Lopez and Juewen Liu. Nanomaterial and Aptamer-Based Sensing: Target Binding versus Target Adsorption Illustrated by the Detection of Adenosine and ATP on Metal Oxides and Graphene Oxide. ***Analytical Chemistry***, 2021, 93, 5, 3018–3025. All of the experiments were performed by the first author. The manuscript was written by Anand Lopez and Juewen Liu.

The work in Chapter 3 has been published as Anand Lopez, Biwu Liu, Zhicheng Huang, Fang Zhang and Juewen Liu. Fluorescein-Stabilized i-Motif DNA and Its Unfolding Leading to a Stronger Adsorption Affinity. ***Langmuir***, 2019, 35, 36, 11932–11939. All experiments except concentration-dependent melting curves were performed by Anand Lopez. Biwu Liu performed concentration dependent melting curves, along with calculation of their rate of change as shown in Figures 3.3A, 3.3B, 3.3C and 3.3D. Zhicheng Huang assisted with circular dichroism experiments as well as experimental design. Fang Zhang assisted with experimental design. The manuscript was written by Anand Lopez and Juewen Liu.

The work in Chapter 4 has been published as Anand Lopez, Yu Zhao, Zhicheng Huang, Yifan Guo, Shaokang Guan, Yu Jia, Juewen Liu. Poly-Cytosine Deoxyribonucleic Acid Strongly Anchoring on Graphene Oxide Due to Flexible Backbone Phosphate Interactions. ***Advanced Materials Interfaces***, 2021, 8, 2001798. Anand Lopez performed the DNA– dependent desorption assays and Yu Zhao performed all molecular dynamics simulations. Zhicheng Huang and Yifan Guo, Shaokang Guan and Yu Jia assisted with experimental design. The manuscript was written by Anand Lopez, Yu Zhao and Juewen Liu.

The work in Chapter 5 has been published as Anand Lopez and Juewen Liu. Fluorescence Polarization for Probing DNA Adsorption by Nanomaterials and Fluorophore/DNA Interactions. ***Langmuir***, 2019, 35, 30, 9954–9961. All of the experiments were performed by the first author. The manuscript was written by Anand Lopez and Juewen Liu.

Abstract

DNA, apart from being the mode of genomic information storage, has found several uses in catalysis (DNAzymes) and target detection (aptamers). Developing novel biosensors utilizing these properties has therefore been a significant avenue for research in recent decades. Of these avenues, interfacing fluorescent dye-labelled DNA with various nanomaterials has birthed many sensors which have been implemented in several environments such as lake water, food, and even within the cell. In this thesis, we provide an improved understanding of DNA adsorption on such nanomaterials and interpretation of sensor results.

In Chapter 1, background information related to DNA, fluorescence and nanomaterials are introduced, with associated examples of different biosensor design. The fundamental questions arising from these sensor designs are also stated, along with thesis objectives. In Chapter 2, a comparison is made between graphene oxide and inorganic metal oxides for aptamer-based fluorescence sensing. It was found that, for graphene oxide, target/aptamer interactions dominate the sensor response. This is in contrast to the metal oxide nanoparticles, where sensing is achieved through the target simply displacing DNA from the nanomaterial surface. In Chapter 3, the properties of carboxyfluorescein-labelled poly-C DNA are explored in detail. Through fluorescence and circular dichroism experiments, it was seen that carboxyfluorescein stabilizes i-motif formation in poly-C DNA, even at neutral pH. This folding was irreversible upon heating. Unfolding of the structure led to improved adsorption on GO demonstrated through fluorescence desorption experiments. In Chapter 4, the anomalously high affinity of poly-C adsorption was investigated using both fluorescence experiments and simulations. It was found that the arrangement of cytosines within the chain did not affect affinity, merely their total number. Through simulations, it was determined that poly-C DNA spreads out on the GO surface due to its lack of intrastrand interactions. This results in more phosphate-backbone hydrogen bond sites and a more favourable bond. At lower pH, i-motif formation drastically reduces poly-C affinity to GO; intrastrand interactions dominate over GO/DNA binding. In Chapter 5, fluorescence polarization was used to characterize labelled DNA interactions with various nanomaterials. First, it was determined that, at low labelled-DNA concentrations, polarization is artificially increased by scattering of incident polarized light. Polarization is also increased with the addition of GO to this DNA. Through a simple mathematical derivation, it was shown that the increase in polarization

with this kind of surface was due to low concentration of free DNA, rather than adsorption to the GO surface. This was compared to a low-quenching surface (Y_2O_3), in which the total polarization observed was dominated by the binding DNA rather than free DNA.

Overall, the work presented in this thesis improves the current understanding of both fundamental DNA/nanomaterial interactions, as well as its implementation in fluorescence-based sensor designs. Future biosensor construction can incorporate these concepts for better sensitivity, specificity and signal interpretation.

Acknowledgements

Well – what a journey! It feels like just yesterday when I started working in Professor Liu's group 10 years ago as a co-op student. His guidance and hands-on approach to supervision, along with the ground-breaking research occurring in his group drew me in. This led me to pursue a Masters degree, and now a PhD, with his group after completing my undergraduate program. I would like to extend special thanks to Dr. Liu for his mentorship over the past 10 years; I could not ask for a better supervisor! I would also like to extend my deepest thanks to Dr. Vivek Maheshwari, Dr. Thorsten Dieckmann and Dr. Boxin Zhao for agreeing to be on my advisory committee, providing crucial advice in evaluating my project and serving on my examining committee. I would also like to thank Dr. Leyla Soleymani for agreeing to be my external examiner for my thesis oral examination.

I would also like to thank the past and present members of my group who helped to make my graduate research efforts successful: Dr. Biwu Liu, Dr. Po-Jung Jimmy Huang, Dr. Feng Wang, Dr. Rhunjun Saran, Dr. Lingzi Ma, Dr. Zhicheng Huang, Dr. Zijie Zhang, Dr. Yuqing Li, Dr. Yibo Liu, Dr. Wenhu Zhou, Dr. Fang Zhang, Dr. Chang Lu, Mohamad Zandieh, Jennifer Moon, Yichen Zhao, Tianmeng Yu, Yu Zhao, Sarah Labas and many other visiting scholars and students who made the Liu Lab a great place to work. It has been a pleasure working with you all and – who knows? – maybe we will work together again in the future. Special thanks are extended to Dr. Biwu Liu, Dr. Po-Jung Jimmy Huang, Dr. Zhicheng Huang and Mohamad Zandieh for productive discussions regarding my research, as well as their help with learning and using equipment.

My experience in Waterloo would not be complete without mentioning the many friends I have made along the way – from undergraduate to graduate levels. First, I would like to thank my undergraduate friends who have been there with me through it all since I arrived in Canada 12 years ago: Matthew Mulvale, Geoff Deignan, Rachel Pautler, Jacob Terry, Matthew Ewertowski, Rana Ahmed, Johan Israelian, Jared Lenos, Brent McCleave, Noorin Samji, Nigel Clarke and James MacLean. Though distance has separated some of us, that we continue to maintain a contact is a testament to the bonds formed over the years. In graduate school, I was fortunate to form friendships with several students in the Institute for Quantum Computing (and IQC-adjacent) who are very close to me: Nachiket Sherlekar, Chris Warren, Jeremy Bejanin, Claire Phelps, Manjit Grewal, Daniel Kruger, Laura Edmonds, Kimia Mohammadi, Noura Bayat, Evan Peters, Nikhil

Kotibhaskar, Irene Melgarejo Lermas, Aditya Jain, Julia Amorós Binefa, and Rahul Deshpande. Although I never understand what your research is about, your passion when discussing your experiments has always inspired me in my own work. Special thanks to Nachiket Sherlekar for being a great roommate over the past 4 years.

I am also fortunate enough to be a board member of the Grand River Jazz Society, which runs the Jazz Room in Waterloo. Through involvement with this organization, I have enjoyed great music, met amazing people, and grew in ways that I did not expect. I would like to thank past and present board members for their involvement in my journey: Stephen Preece, Cameron Bates, Ruth Harris, Janet Dawson Brock, Kim Wakeford, Janine Sharpe, Colin Reed, John Lord, Sam Ogilve, Kim Sutherland, among many others.

Though the pandemic has separated us for quite a few years, I would like to thank my high school friends who have continued remain in contact with me while being over 2000 km away: Sharaine Best, Mahesh Bhajan, Tonya King and Stephon Rayside. I hope one day soon we can meet up for good times like we used to!

Finally, I would like to thank my family for their encouragement and love. Without them, I could not envision myself being close to the person I am, as well as being in this privileged position.

Dedication

I dedicate this thesis to my parents (Francis and Vyju), for their unwavering support and love.

Table of Contents

List of Figures

List of Tables

List of Abbreviations

ATP: Adenosine triphosphate

AuNPs: Gold nanoparticles

BSA: Bovine serum albumin

CD: Circular Dichroism

cDNA: Complementary DNA

CNTs: Carbon nanotubes

CSA: Contact surface area

Cy3: Cyanine 3

DLVO: Derjaguin Landau Verwey Overbeek

DNA: Deoxyribonucleic acid

DNAzymes: DNA enzymes

FAM: Carboxyfluorescein

FITC: Fluorescein isocyanate

FP: Fluorescence polarization

FRET: Förster resonant energy transfer

GO: Graphene Oxide

GTP: Guanosine triphosphate

HBs: Hydrogen bonds

HEPES: 4-(2-hydroxyethyl)-1-piperazineethanesulfonic acid

IM: Telomeric i-motif DNA

ITC: Isothermal calorimetry

Kd: Dissociation constant

L-J: Lennard Jones

MD: Molecular dynamics

MES: 2-(N-morpholino) ethanesulfonic acid

MONPs: Metal oxide nanoparticles

mRNA: Messenger RNA

NTPs: Nucleotide triphosphates

PEG: Polyethylene glycol

PME: Particle-mesh Ewald

RNA: Ribonucleic acid

ssDNA: single-stranded DNA

TEM: Transmission electron microscopy

Tm: DNA melting temperature

Tris: tris(hydroxymethyl) aminomethanesodium

USEPA: United States Environmental Protection Agency

UV: Ultraviolet

WHO: World Health Organization

Chapter 1 - Introduction

As industrialization powers on, its toxic by-products have leeched into rivers, oceans and agricultural lands which supply our food and water. For example, 10 heavy metals have worldwide concentrations higher than the World Health Organization (WHO) or United States Environmental Protection Agency (USEPA) thresholds in the 2010s, compared to just 2 in the 1970s.[1] In many cases, sensitive detection of these toxic ions requires expensive equipment (e.g., mass spectrometry) which does not lend itself to portability and ease-of-access. Apart from environmental concerns, new developments in disease research and pharmacology have found biological targets (e.g., antibiotics, viral polynucleotides, proteins associated with cancer) which are clinically relevant.[2–4] Monitoring of these targets can also be difficult without sophisticated equipment, which is not desirable in scenarios or geographic locations where action is needed quickly.

To address these issues, sensors and biosensors have been developed which rely on chemical and biochemical reactions that provide a simple signal (e.g., fluorescence, absorbance or electric) describing the presence or absence of the target analyte.[5,6] Of these, deoxyribonucleic acid (DNA)-based sensors have showed extensive promise due to DNA's relative stability (compared to proteins), decreasing manufacturing cost and customizability in design.[7,8]

Simultaneously, research in nanotechnology in the last few decades have yielded materials (called "nanomaterials") that exhibit unique electrical and optical properties.[9–11] Researchers have developed DNA/nanomaterial hybrid sensors which have the benefits of both systems. Initial research in the late 1990s to early 2000s focused on gold nanoparticles (with their unique optical properties) and DNA in colourimetric sensors.[12–14] Later, as they became more popular and less costly, DNA was interfaced with carbon nanotubes (CNTs),[15,16] graphene oxide (GO) and metal oxide nanoparticles.[17,18] These nanomaterials have been integrated with DNA mostly in the development of fluorescent sensors for a variety of targets. However, there is a need for further fundamental insight into how these sensors work, from DNA/nanomaterial interactions to the signal response itself.

In this thesis, I address some of these problems which ultimately can be used to improve sensor design. To understand the nature of these problems, as well as my explanations provided in

Chapters 2-5, the following sections will be used to introduce the chemistry of DNA, fundamentals of fluorescence, and properties of the specific nanomaterials used in this work.

1.1 DNA – Versatile and Robust

Deoxyribonucleic acid (DNA) is a polymer that stores the genetic information of every living organism.[19–21] In this context, it is normally referred to as a "genome" and is the main constituent of the cell nucleus. The information in the genome is decoded in two steps: transcription and translation. The end result is the formation of proteins, which have various biological functions either within a cell (intracellular) or outside the cell (extracellular). Outside of the storage of genetic information, DNA was not seen as a useful or functional polymer until around three decades ago with the development with aptamers and DNAzymes. Before discussing these concepts, however, we need to explore the composition and chemical properties of DNA.

1.1.1 Chemical properties of DNA

The monomeric unit of DNA is referred to as a nucleoside and is composed of a deoxyribose ring with a base on the 1′ carbon (Figure 1.1A). This monomeric unit is linked to another through a phosphodiester bond between the 3′ carbon of the previous monomer and the 5′ carbon of the following monomer. Ribonucleic acid (RNA) is very similar to DNA, except there is a ribose ring instead of a deoxyribose ring. Generally, DNA has two termini: the 5′ carbon of the first deoxyribose ring, and on the 3′ carbon of the last deoxyribose ring. There is only one ionizable proton within each phosphodiester linkage and its pK_a is very low (~ 1).[22] Therefore, at neutral pH, the phosphate backbone is negatively charged.

The base at the 1′ carbon can be either adenine, guanine, thymine (uracil in the case of RNA) or cytosine (Figure 1.1B). Each base has their own pK_a (or in the case of guanine, two pK_as). For adenine, cytosine and guanine, there is an acidic pK_a where the N1, N3 and N7 (respectively) are protonated, and the base has a positive charge.[23] For thymine and guanine, there is also a basic pK_a where deprotonation occurs at the N3 and N1 position (respectively), and the base has a negative charge. Despite all this nuance, at neutral pH, all bases are uncharged. When the charge of the phosphate backbone is considered, all DNA strands are negatively charged at neutral pH.

Hydrogen bonding between two bases gives rise to an interaction known as a "base pair".[21] The canonical Watson-Crick interactions occur between adenine and thymine (the A – T base pair)

and guanine and cytosine (the G – C base pair). One can therefore imagine that, for a given single-stranded DNA, there exists another strand that can perfectly base pair with it. This strand is called the "complementary strand" and the process of base pairing is called "hybridization". The result of hybridization is the formation of the DNA duplex (Figure 1.1C). While hydrogen bonding is a key factor in the formation of the DNA duplex, favourable stacking interactions between neighbouring bases also confer stability to the structure.[24,25] Furthermore, the stability of duplexes increases with strand length (more hydrogen bonds, stacking interactions) and G-C content (3 hydrogen bonds vs. 2 in A-T base pairs).[26,27] In nature, there are 3 major forms of the duplex: A-DNA, B-DNA and Z-DNA. Of these, B-DNA is believed to be the predominant form of DNA in cells.[21]

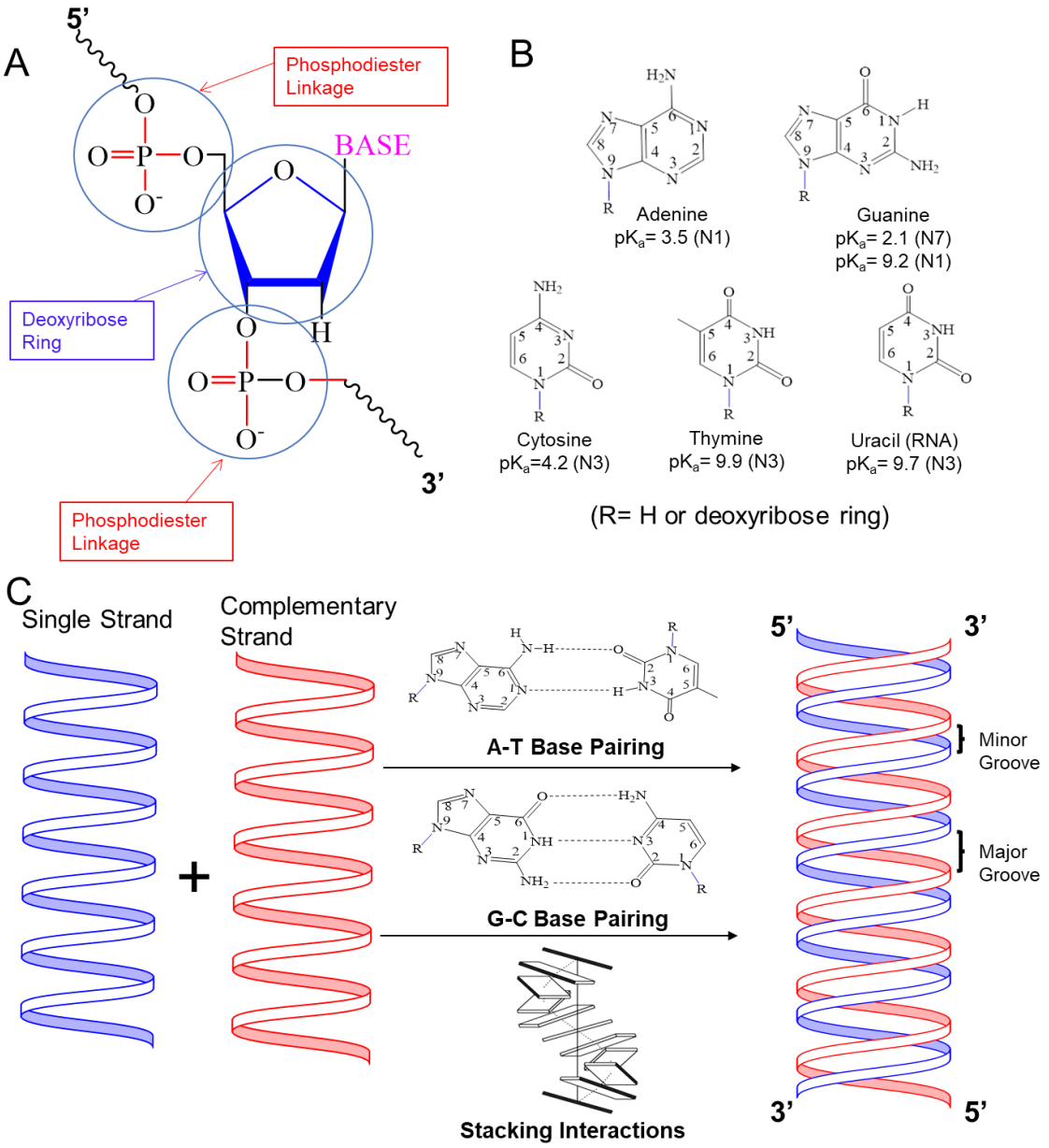

Figure 1.1. Physicochemical properties of DNA.(A) The structural unit of DNA including the phosphate backbone, deoxyribose ring and the base. (B) Chemical structures of the DNA/RNA bases and their associated pKa values. (C) The process of DNA hybridization by Watson-Crick base pairing and stacking interactions.

The DNA duplex has several interesting features that are consistent despite sequence variations. For example, there are two unequally spaced regions between the two strands called

the major and minor grooves.[28,29] The groove spacings are different depending on the DNA form (A – DNA, B – DNA, etc.) and can provide binding sites for several chemical moieties, such as drugs, dyes or proteins. Indeed, such a mechanism is used in clinical therapeutics, especially in chemotherapy. The DNA duplex is typically modelled as a "rigid rod" which may be accurate for shorter strands (< ~150 base pairs but is dependent on base composition).[30–32] However, longer strands have a "persistence length" – the number of bases (or distance) where the orientation is correlated – which can be used as a measure of DNA stiffness. In general, a longer persistence length means a more rigid duplex with less bends.

To end this section, we will outline two non-traditional secondary DNA structures that are also found in nature. Both structures require specific conditions (pH or salt) and do not form any Watson-Crick base pairs. Firstly, there is the G-quadruplex (Figure 1.2A) which (as the name implies) is composed of a series of G–quartets: 4 guanine (G) bases forming hydrogen bonds with each other.[33] More specifically, one G binds two other G bases and the resulting structure is square-like. The G-quadruplex is stabilized by either potassium, magnesium or other divalent metals (though potassium is most commonly utilized). These structures are found in the telomeric regions of genomic DNA and are their exact function is still a topic of research.[34–36] Finally, another structure formed in the telomeric regions are the cytosine (C) analogue of the G-quadruplex: the i-motif. It is not a quadruplex; the hydrogen bonds are between two C bases instead of four with the G-quadruplex (Figure 1.2B). More specifically, the base pair occurs between a protonated and unprotonated C, which can occur at under slightly acidic conditions (pH < 5).[37–39] Stabilization at higher pH can also be achieved with metal ions,[40–42] intercalating ligands,[43] molecular crowding,[44] or non-canonical modifications of the DNA.[45,46] In most cases, this enhanced stability is attributed to an up-shift of the cytosine pK_a value. This structure will be explored in more detail in Chapter 3, where we explore the effect of conjugated dyes on i-motif formation and their effect on nanomaterial adsorption, as well as Chapter 4, where we investigate the high affinity of poly-C DNA to nanomaterials.

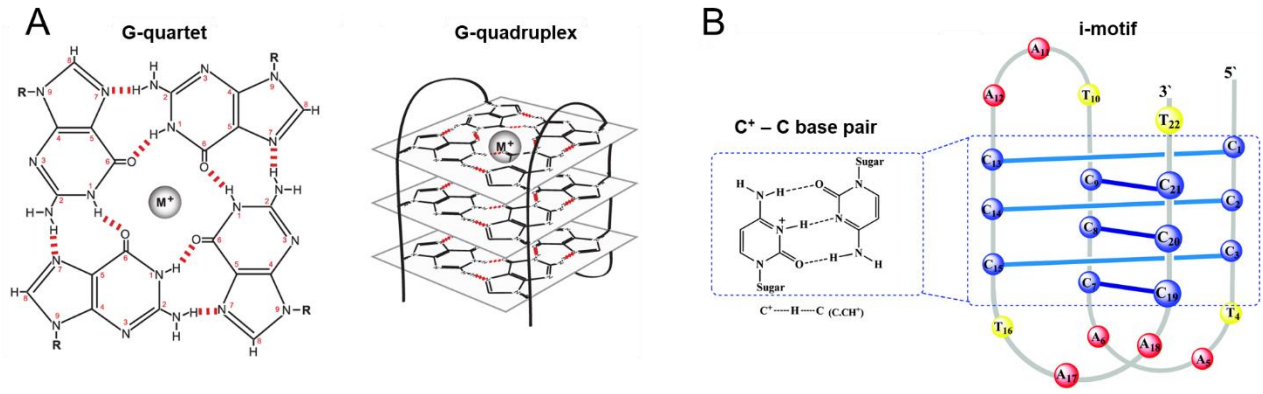

Figure 1.2. Structures of (A) the G-quadruplex and (B) the i-motif. Image (A) reproduced from ref.[47]. Creative Commons Attribution License. Image (B) reproduced from ref.[48] with permission. Copyright © 2017 Royal Society of Chemistry.

1.1.2 Functional DNA

In this thesis, we do not explore the genomic role of DNA but, instead, utilize it in a functional way (i.e., sensing). In 1990, Szostak and Ellington wondered whether polynucleotides can bind to a ligand with very high affinity (in a similar way to how protein antibodies can bind antigens).[49] In principle, such a method would rely on specific interactions between the nucleobases and the target ligand (analogous to amino acid sequences in proteins). They designed a process by which an RNA containing small region of randomized bases flanked by two primer regions (N_{random} = 20 – 30 bases, called a "RNA library") is incubated with a target ligand (in their case, thrombin). Binding RNA were isolated, purified and amplified (i.e., concentrated) using the polymerase chain reaction. This process was repeated several times (called "rounds"), lowering the target concentration to isolate only the most tightly bound RNA strand (or strands). The RNA was then sequenced, and the resulting strand called an "aptamer" for thrombin – a term coined by Szostak himself. Two years later, the same group isolated the first DNA aptamer using a similar process except the targets were DNA-binding dyes.[50] Since the development of the thrombin aptamer, researchers have evolved several DNA and RNA aptamers for a variety of different target ligands (and even different aptamers for the same target). A representative example is shown in Figure 1.3A – the adenosine aptamer.[51] This aptamer has two loops, and it is generally accepted that each strand binds two adenosine molecules. The dissociation constant (K_d – the ratio of the rate of

aptamer-target dissociation to association) for this aptamer was determined to be ~10 μM from isothermal calorimetry (ITC) measurements in our group.[52] We use the adenosine aptamer in Chapter 2, where we look at the influence of non-specific displacement *vs.* aptamer binding DNA-nanomaterial biosensors.

DNA can also catalyze chemical reactions, and this development shares some of its history with DNA aptamers. In the early 1980s, the groups of Sidney Altman and Thomas Cech found that natural RNA structures can catalyze biological reactions: ribozymes,[53] a discovery that won them the Nobel prize in 1989. The quintessential example is the hammerhead ribozyme, which was discovered in 1986.[54] This ribozyme catalyzes both the cleavage and ligation of RNA at a specific site and typically uses a metal ion cofactor (e.g., Mg^{2+}), which would be in equilibrium with its hydroxide in solution. This metal hydroxide, in turn, could act as a general base or acid in the cleavage and/or ligation.[55] During the 10 years after this discovery, there was extensive research into whether any natural DNA enzymes (or "DNAzymes") existed. Alas, this search was unsuccessful (and remains so to this day) even though many more natural ribozymes were discovered.[56] This was surprising as, apart from the 2′ carbon (hydroxyl vs. no hydroxyl) and one of the pyrimidine bases (thymine vs. uracil), DNA and RNA are chemically very similar to each other. Researchers were not discouraged, however, and sought to investigate whether it would be possible to synthesize a DNAzyme artificially. About 12 years after the discovery of the ribozyme, the first artificial DNAzyme (a ribonuclease – an enzyme that cleaves a ribonucleotide site) was developed using a modified version of the *in-vitro* selection process described above.[57] Most DNAzymes are ribonucleases though ligases,[58–60] and even DNA-cleaving DNAzymes,[61] have also been developed. In the context of analytical chemistry, the most important feature is not the reaction itself but the metal co-factor, which is the target analyte in the *in-vitro* selection. The general idea is that unique DNAzymes (mostly ribonucleases) would require different metal co-factors to function and can therefore be used to sense that metal ion. For example, our group recently developed a Ag^{+} -specific DNAzyme (Figure 1.3B).[62] It is composed of an enzyme strand which has a region known as a "catalytic loop", where Ag^{+} can bind and catalyze the cleavage of a single ribonucleotide site on the partially hybridized strand (the substrate strand).

Even more recently, DNA has been used to create nanostructures and one of the most sophisticated examples is known as "DNA origami". The general concept of DNA origami is

shown in Figure 1.3C. A large circular viral DNA is hybridized with several smaller strands (called "staple strands") designed to form the desired shape. The initial report showcased several unique and complex structures formed by this simple combination of DNA (stars, triangles and even smileys).[63] These days, computer programs can help one to design such structures, which reduces potential human error.[64] DNA origami has been used in applications such as drug delivery,[65] biosensors,[66] and nanopore technologies.[67]

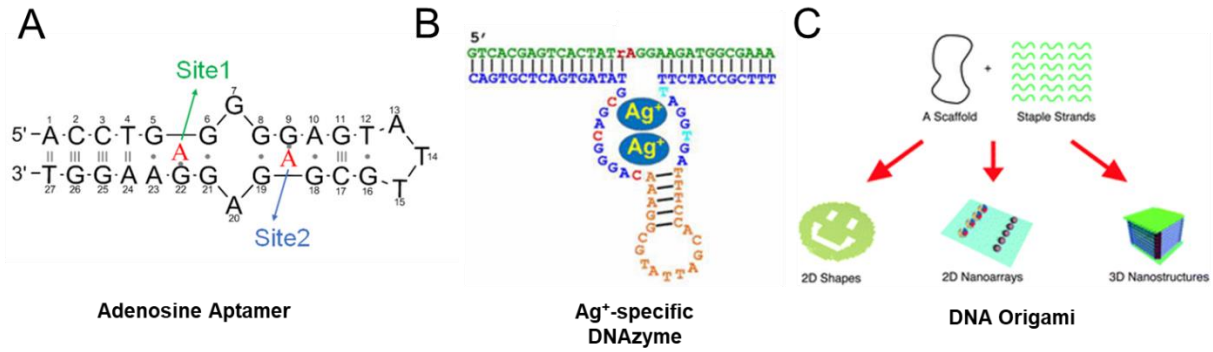

Figure 1.3. Different types of Functional DNA. (A) General structure of the adenosine aptamer including the two binding sites. Image reproduced from ref.[52]. Creative Commons Attribution License. (B) The silver-dependent DNAzyme which binds two Ag+ ions within its catalytic loop. Image reproduced from ref.[62] with permission. Copyright © 2017 American Chemical Society. (C) Scheme of DNA origami formation using a circular viral DNA strand along with smaller staple strands. Image reproduced from ref.[68] with permission. Copyright © 2010 Royal Society of Chemistry.

1.1.3 Biosensors

Many aptamers and DNAzymes have been used to make biosensors. A biosensor is classically defined as having two parts: i) a biorecognition element – a chemical molecule or entity that can bind to the target analyte and ii) a signal transduction element – a probe molecule or device that can translate the binding to measurable signal.[69] More recently, this definition has grown to encompass both the electronics (converting the signal to a current or another electronic parameter) and display (where the electronic parameter is visualized on a plot or graph).[70] Aptamer– and DNAzyme– binding would fall into the category of "biorecognition element". Intrinsically, however, there is no property of DNA (currently) that could reliably correlate this binding event with a signal. Therefore, DNA is typically covalently labelled with a reporter molecule, which is

dependent on the method of signal detection. In this thesis, we will be using fluorescent labels almost exclusively in this regard. Therefore, in the next section, we explore the nature of fluorescence – from theory to experimental implementation.

1.2 Fluorescence Spectroscopy and Anisotropy

Fluorescence is the process by which a molecule (called a "fluorophore") emits radiation after excitation from their ground state.[71] This emission of radiation returns the fluorophore to its ground state. A simplified view of this process can be represented by a Jablonski diagram (Figure 1.4A). The timescale of the emission is longer (typically nanoseconds) than that of intramolecular vibrations (picoseconds). Therefore, energy is constantly being dissipated in this way (called non-radiative processes) as the molecule decays to its lowest energy excited state, before returning to the ground state with radiative emission. Consequently, the emitted radiation is always (except in very specific circumstances) of lower energy than the radiation used in excitation.

One can define several parameters that are characteristic of a fluorophore. Firstly, the quantum yield – a ratio of the intensity of emitted photons to excitation photons – can be considered a measure of the efficiency of the intramolecular transitions and is unique to each fluorophore. Secondly, each fluorophore has at least one characteristic excitation (λ_{exc}) and emission (λ_{em}) wavelength maxima. The difference between these two values is known as the Stokes' Shift. Finally, the fluorescence lifetime (τ) describes how long a fluorophore takes to emit a photon after excitation. This value varies depending on the fluorophore but, for typical labelled reporter probes, is typically in the range of 1-20 ns. The most common fluorophore used in DNA biosensing (as well as in this thesis) is carboxyfluorescein (also known as FAM – structure shown in Figure 1.4B), which has an λ_{exc} of ~ 490 nm and a λ_{em} of ~ 515 nm with a high quantum yield (> 0.80).[72,73] This fluorescence is notably pH dependent – with a significant reduction in quantum yield in acidic environments due to protonation. Other fluorescent dyes, such as cyanines,[74] are also used to label DNA but are less common.

The fluorescence emitted by a biosensor can be detected using fluorescence spectroscopy. The typical scheme is shown in Figure 1.4C.[75] The process starts with the generation and selection of excitation radiation. A Xe lamp is normally used for this purpose, as it emits radiation with near constant intensity from the near-UV to infrared regions.[76] The desired wavelength is selected using a monochromator – composed of a prism (to disperse white light into its constituent wavelengths)

and slits (to select the desired wavelength). After interaction with the sample, the emitted light (collected at a 90^{o} angle to the sample to prevent transmitted excitation light) passes through another monochromator and amplified using a photomultiplier tube before detection. There are two types of measurements: emission and excitation scans.[71] An emission scan is the typical experiment performed when the peak excitation wavelength is known. The excitation wavelength is kept constant and the emission at different wavelengths is collected. However, if this peak excitation wavelength is not known, an excitation scan can be performed. Here, the emission wavelength is kept constant, and the excitation wavelengths are varied (as long as it is lower than the emission wavelength). In our experiments, we only use emission scans as the reporter molecules attached to our DNA probes have a known excitation wavelength.

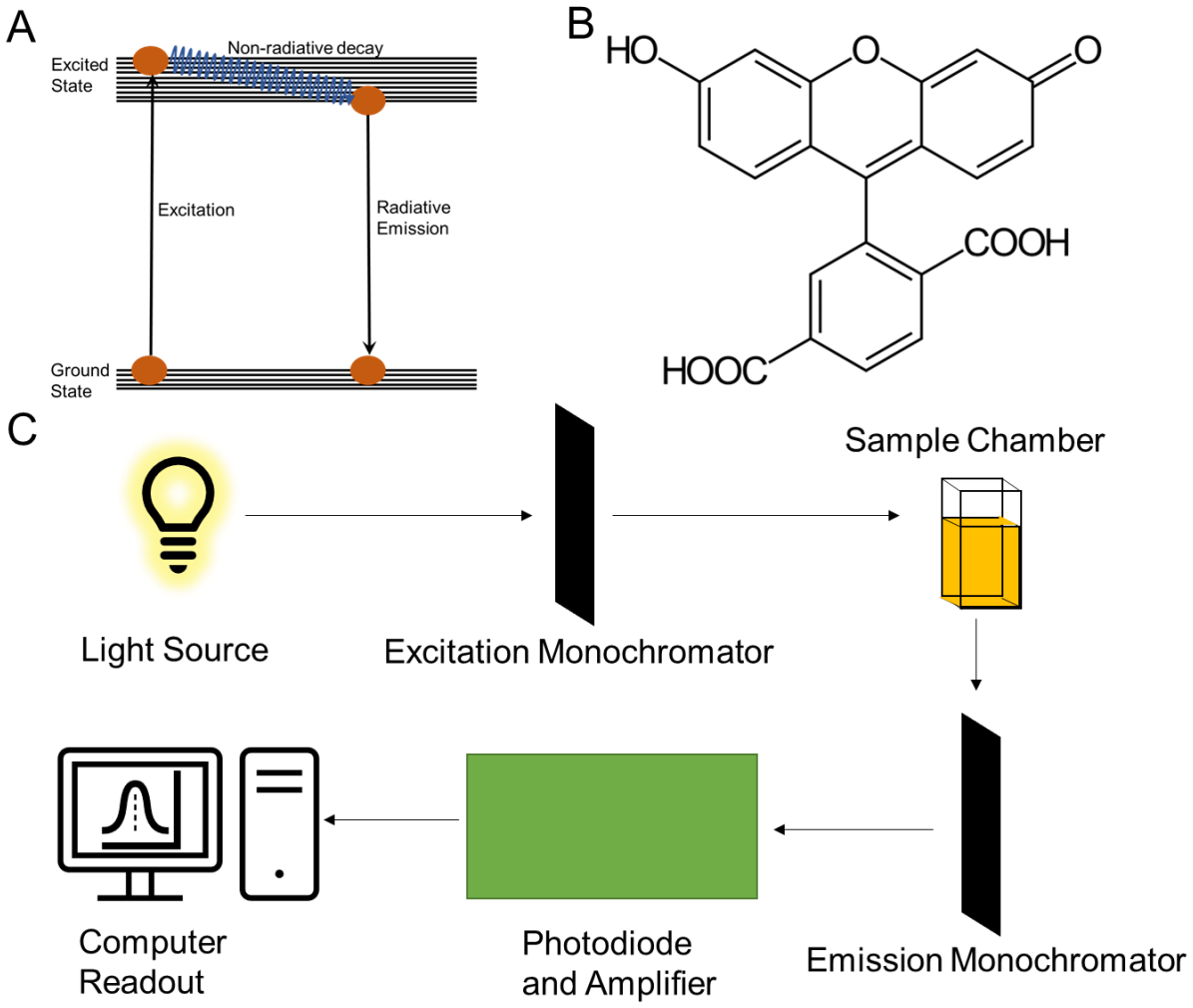

Figure 1.4. The process of fluorescence and its experimental implementation. (A) Simplified Jablonski diagram showing the electronic transitions responsible for fluorescence. (B) Chemical structure of the common DNA label, carboxyfluorescein. (C) Scheme of fluorescence spectroscopy from sample excitation to computer readout.

Finally, we will discuss one more aspect of fluorescence: anisotropy (or polarization). As mentioned earlier, fluorescence involves the absorption and emission of energy due to electronic transitions. However, there is a bit more nuance to this process. Excitation will only occur if the polarity of the incoming radiation is parallel (or has some parallel component) to the absorption vector (or dipole) of the fluorophore.[77] This process is known as photoselection and is illustrated in Figure 1.5A. At first glance, such a stringent rule may appear to be detrimental to fluorescence.

However, in typical fluorescence spectroscopy, the excitation radiation is unpolarized, which makes the emission also unpolarized. If one were to polarize the excitation radiation to a specific plane, then photoselection becomes much more important. Only fluorophores with absorption vectors aligned with the polarized light will be excited. Since fluorescence occurs at a longer timescale than molecular rotation,[78] the emitted light is randomly polarized if the fluorophore is free in solution (Figure 1.5B, top)). However, if the fluorophore is bound to a larger entity, these rotations are hindered (now on the same timescale as fluorescence),[77] and the emitted light is also relatively polarized (Figure 1.5B, bottom). The instrumental setup is similar to fluorescence spectroscopy, except polarizers are added before and after the sample chamber. The emitted light that is parallel ($I_{||}$) and perpendicular ($I_{\perp}$) to the excitation plane is measured and the anisotropy (r) is calculated according to the following formula:

$$r = \frac{I_{||} - I_{\perp}}{I_{||} + 2I_{\perp}}$$

There is a "2 $I_{\perp}$" in the denominator as it considers both the y and z axes which are both perpendicular to the excitation light polarization (assuming it is in the x direction). A related parameter is called polarization (P) and has a similar formula to anisotropy:

$$P = \frac{I_{||} - I_{\perp}}{I_{||} + I_{\perp}}$$

Both quantities have the same physical meaning, though the magnitudes are different. Indeed, modern instruments typically produce both values upon measurement. In the context of analytical chemistry, anisotropy is used to quantify the binding of a smaller ligand (typically labelled with a fluorophore) to a larger moiety.[79] Before binding, the free fluorophore rotates constantly and will therefore have low anisotropy. Upon binding, this rotation is hindered (as previously shown in Figure 1.5B) and anisotropy/polarization is increased. This is the focus of Chapter 5, where we examine the quenching effect of nanomaterials on the fluorescence polarization of FAM-labelled DNA.

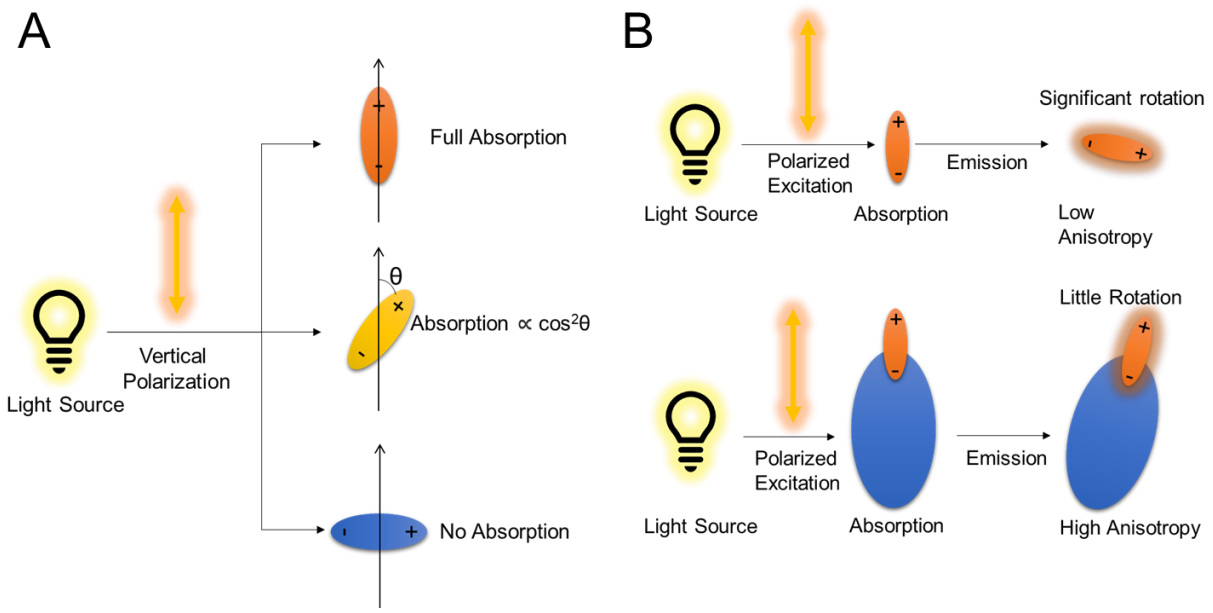

Figure 1.5. Fundamentals of fluorescence polarization. (A) The process of photoselection. A fluorophore is only excited if its absorption dipole is parallel to the polarization of the excitation radiation. (B) Emission polarization/anisotropy of free (top) and bound (bottom) fluorophore. If the fluorophore rotates significantly in the timescale of fluorescence, then anisotropy will be low. The opposite is true in the case of a slow rotation.

1.3 Aptamer and DNAzyme – based Biosensors

We have now looked at functional DNA and the concept of fluorescence, but how are these implemented in biosensing? Firstly, it is important to distinguish between "signal on" and "signal off" sensors. In the former, the fluorophore's emission is quenched, and addition of the target will increase fluorescence. Conversely, in a "signal off" sensor, fluorescence is initially high, and addition of target will quench fluorescence. Quenching can be achieved by designing the sensor so that fluorophore is close to another chemical moiety aptly known as a "quencher". As the fluorophore is excited by incident light, the absorbed energy is transferred non-radiatively to the quencher and dissipated.[80] Such a process can only occur if the fluorophore is sufficiently close to the quencher (from a few angstroms up to ~10 nm). Alternatively, energy transfer can occur between a fluorophore and another radiative fluorophore; instead of a non-radiative dissipation, the fluorescence of the second fluorophore increases.[81] This process is known as Förster resonant

energy transfer (FRET). In this case, the fluorophore that is initially excited is known as the "donor" and the fluorophore emitting the reabsorbed energy is called "acceptor". Implementation of quenchers and FRET acceptors represent the bulk of DNA fluorescence sensors, and we will discuss a few representative examples in this section.

A typical DNA biosensor with a fluorophore – quencher pair is a molecular beacon (Figure 1.6A).[82–84] The probe sequence consists of a hairpin DNA (base pairs near the terminal ends with a large unpaired loop) with a fluorophore (F) and quencher (Q) at each end. In this state, the fluorescence is quenched as the fluorophore is close to the quencher. If the target (mostly a DNA sequence of interest) is added, the hairpin unfolds so that binding can occur. The fluorophore and quencher would be further away from each other, and fluorescence will increase. This kind of sensor has been particularly popular for messenger RNA (mRNA) detection, where it has seen consistent use over the last couple of decades for *in vitro* and *in vivo* sensing.[85–89] Variations on this sensor also utilize FRET for enhanced selectivity and sensitivity.[90] The target need not be DNA/RNA; some sensor designs can be used to detect metals, proteins or small molecules (Figure 1.6B). In this case, folding of the DNA upon target binding displaces the fluorophore-quencher pair from their close interaction, increasing fluorescence. Such a design has been utilized for protein (namely thrombin) and K^+ detection.[91–94] An interesting variation was introduced by Zhang et. al, in which the molecular beacon contains a single ribonucleotide site within the loop of the molecular beacon hairpin (Figure 1.6C).[95] This serves as a site for target dependent DNAzyme cleavage, splitting the beacon in two and increasing fluorescence.

With DNAzymes, a molecular beacon is not necessary to design a robust biosensor. Older implementations have utilized quencher-labeled enzyme strands which cleave fluorophore-labeled substrate strands in the presence of the DNAzyme co-factor (Figure 1.6D). This type of sensor has been used in several variations to detect a wide selection of metals and molecular targets.[96–102] As new DNAzymes are discovered, they are often incorporated into such sensors to prove that the enzyme can function.

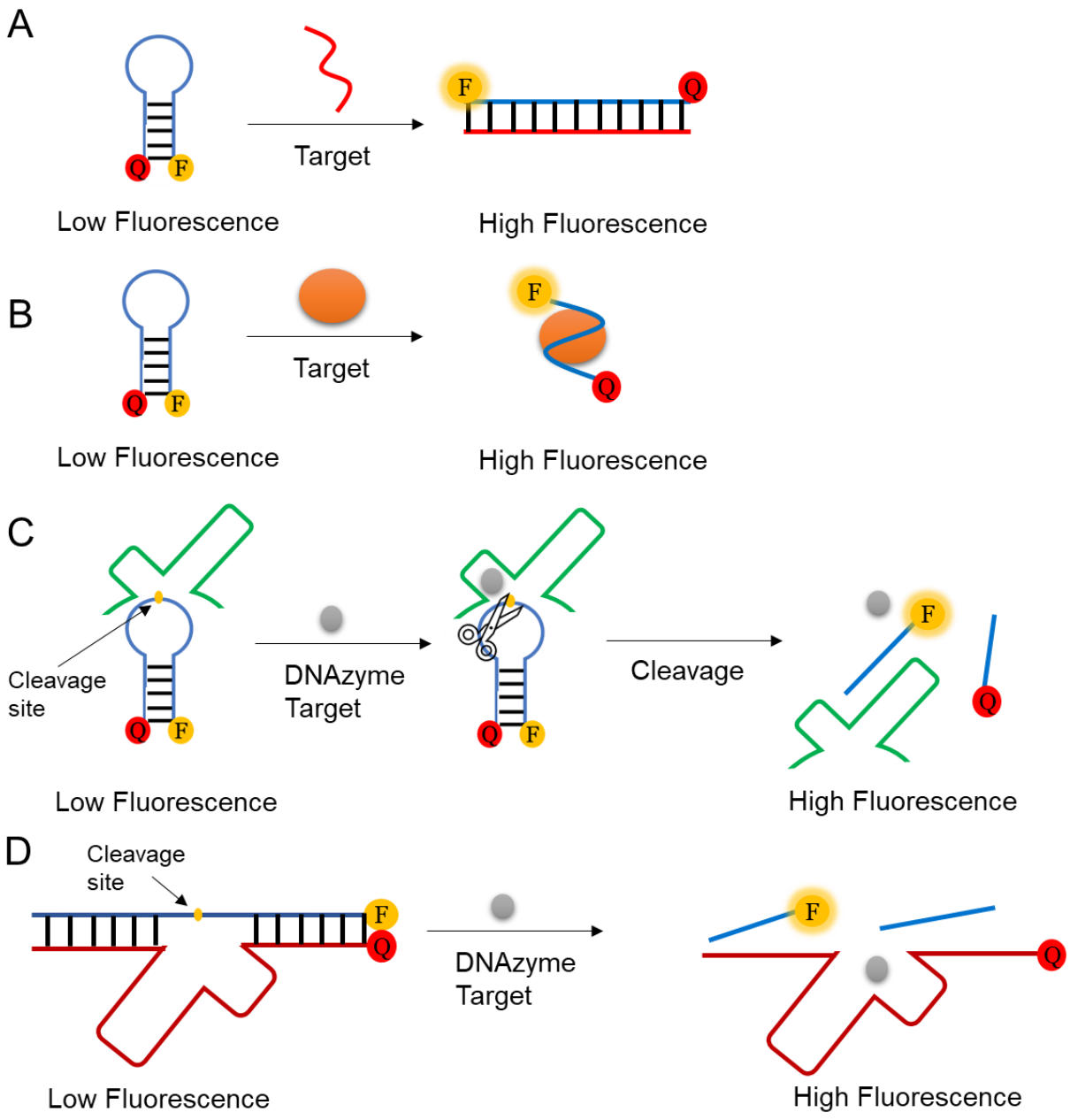

Figure 1.6. Four different strategies for DNA fluorescence biosensor design (A) A traditional molecular beacon where the addition of a target DNA hybridizes with a hairpin DNA, increasing the distance between fluorophore and quencher. (B) The same type of molecular beacon, except the target is a not DNA (e.g., protein, metal ion, small molecule). (C) A molecular beacon with ribonucleotide cleavage site where a target-dependent DNAzyme can cleave, splitting the beacon in half. (D) Traditional fluorescence DNAzyme sensor where a quencher labelled enzyme strand

is hybridized with a fluorophore labelled substrate strand. Upon addition of the target, cleavage of the ribonucleotide site occurs, releasing the fluorophore labelled strand.

Finally, fluorescence polarization/anisotropy has also been used in DNA-based biosensors.[79,103,104] As discussed earlier, if a fluorophore is bound to a much larger moiety, its polarization/anisotropy is increased significantly compared to the free fluorophore. Such an increase could be obtained by aptamer-target binding (a similar scheme to Figure 1.5B, bottom). However, the target needs to be sufficiently large or else the aptamer would not rotate much slower in the bound state. Therefore, this method has been restricted to directly targeting proteins or using large particles/macromolecules as a means to measure small molecule binding.[105–107] This being said, small changes in anisotropy have been observed with direct binding of small molecules to aptamers, which could be analytically useful.[108,109]

1.4 The DNA/Nanomaterial Interface

Apart from sensors exploiting specific DNA folding interactions upon target binding, the diverse properties of nanomaterials have also lent themselves to biosensor development. This is possible since DNA often interacts with these nanomaterials, resulting in physical adsorption (or physisorption). Physisorption refers to the partitioning of a solute, liquid, or gas at the interface between two phases due to non-covalent interactions.[110] These non-covalent interactions include electrostatic (including hydrogen bonding) forces, van der Waals forces and π-π stacking. In most cases, the net interaction is a combination of these forces. This thesis is mainly focused on DNA adsorption on GO and, to a lesser extent, metal oxide nanoparticles. These two nanomaterials are chosen for several reasons: 1) They adsorb DNA through different mechanisms (which we will discuss in a later section), 2) Metal oxide nanoparticle interactions with DNA are not as studied as other surfaces (such as gold nanoparticles) with aptamer-based biosensors,[111,112] 3) They both quench fluorescence once dye-labelled DNA is adsorbed (which may not be the case for softer organic/polymeric nanomaterials), and 4) GO is an established carbon-based nanomaterial that has demonstrated wide use in fluorescence-based biosensors (and can be used as a standard to compare).[113,114] First, we will discuss the physicochemical properties of each material. Then, we will explore the theory of the fundamental non-covalent interactions before looking at the physisorption of DNA on GO and metal oxide nanoparticles.

1.4.1 Chemical Properties of Graphene Oxide

GO is derivative of graphene – a single layer of carbon with a lattice of honeycomb structural units.[115,116] The carbons in a single layer of graphene are predominantly sp^2 hybridized. Graphene, without modification, is very hydrophobic and will not disperse in aqueous solutions. This limits its application in fields where water is used as a solvent. Graphene is therefore chemically modified to facilitate this solubility. GO is one such modification where (as the name implies) graphene is oxidized, resulting in the formation of carboxylic acid (R-COOH), hydroxyl (R-OH) and epoxy (R-O-R) groups on its surface, as shown in Figure 1.7A.[117,118] The carboxylic acid groups are more prominent at the edges, while epoxy and hydroxyl groups occur more abundantly in the basal plane. At an industrial scale, GO is produced by treating graphite with potassium permanganate ($KMnO_4$) acidified with sulphuric acid (H_2SO_4) followed by exfoliation – a process known as Hummer's Method.[119] Modifications of this method are mainly focused on the type of acid used, which may also affect surface functionality. For example, Hummer's method uses sulphuric acid, which would result in scattered organosulpho species on the surface. If nitric acid is used instead, there may be the presence of amine ($R\text{-}NH_2$) or amide ($R\text{-}CONH_2$) groups. In any case, oxidation occurs non-selectively which results in a very heterogenous surface; some areas will be more oxidized (and therefore hydrophilic) than others. In this thesis, we use GO produced by Hummer's method, which will be negatively charged at neutral pH due to deprotonation of carboxylic acid groups ($pK_a \sim 5$).[120]

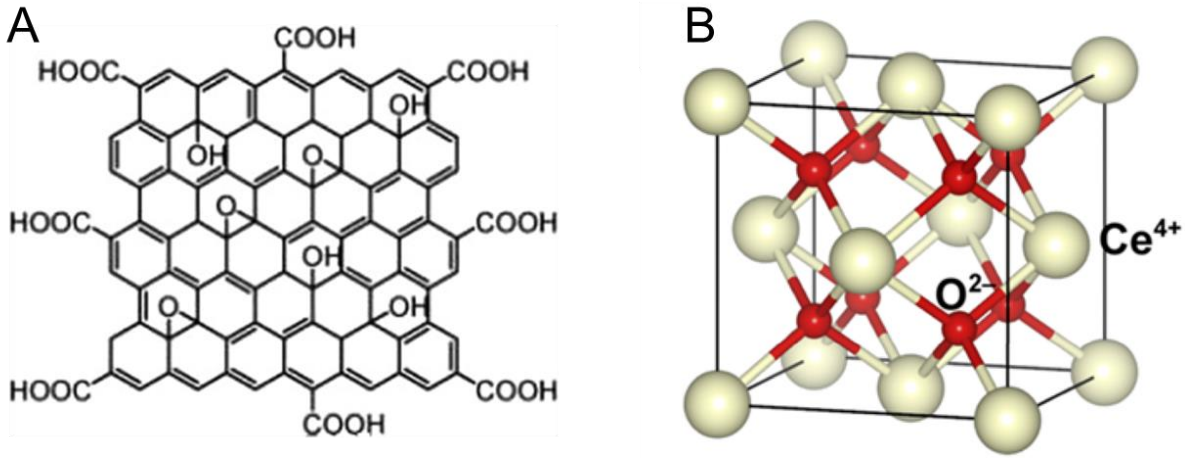

Figure 1.7. Structural properties of GO and metal oxides. (A) General structure of GO. Carboxyl groups are located on the edges, with hydroxyl, epoxide and hydrophobic domains located on the

interior. Image reproduced from ref.[121] with permission. Copyright © 2012 American Chemical Society. (B) Face-centered cubic unit cell of CeO_2, encompassing 4 Ce^{4+} ions and 8 O^{2-} ions. Image reproduced from ref.[122] with permission. Copyright © 2018 Elsevier B.V..

1.4.2 Chemical Properties of Metal Oxides

In Chapters 2 and 5, we compare GO to different metal oxide nanoparticles. These include (but are not limited to) CeO_2, Fe_3O_4, TiO_2, Y_2O_3, NiO and ZnO. Each of these materials have their own physicochemical properties that lend themselves to different applications. For example, CeO_2 adopts a face-centered cubic unit cell structure with 4 cerium atoms and 8 oxygen atoms (Figure 1.7B).[123] Furthermore, CeO_2 nanoparticles can be made quite small, with individual particles comprising only a few (~8) unit cells. The surface of CeO_2 has a mixture of Ce^{3+} and Ce^{4+}, oxygen-containing groups (hydroxyl, water, etc.) and vacancies that change the electronic properties of the nanoparticle.[124,125] They allow the surface Ce to easily cycle between Ce^{3+} and Ce^{4+}, which gives rise to weak oxidase activity. This can be enhanced by the addition of peroxide (i.e., as a peroxidase) or fluoride.[126] Fe_3O_4 has a similar catalytic activity, but uniquely exhibits size-dependent magnetic properties.[127,128] We will only explore DNA adsorption on these metal oxide nanoparticles without exploring their specific properties.

Most metal oxide nanoparticles are produced using precipitation, where a base (such as ammonium hydroxide) is added dropwise to a solution of the metal ions in the presence of a stabilizer.[129] If completely amorphous particle growth is observed, then the particle will be spherical to minimize surface energy. Often, however, crystallization takes place and there are preferred planes of particle growth, resulting in nanoparticles of irregular shape with areas of amorphous and crystalline regions.[130] Some research groups have exploited this anisotropy to produce nanoscale rods or stars (which normally involves treatment at elevated temperatures).[131,132] In this thesis, we will primarily be using particles of irregular shape as they are produced cheaply at a large scale. As an aside, at neutral pH, the surface of most metal oxides is dominated by their hydroxide. This results in them having a weak negative charge at neutral pH which changes to positive in slightly acidic (~pH 4-5) conditions.[133] The surface metal ions have

a high affinity to oxygen-based ligands, and thus many metal oxides adsorb DNA via the phosphate backbone of DNA.

1.4.3 Fundamentals of intermolecular forces

Before exploring the modes of physisorption of DNA on these nanomaterials, we need to introduce the characteristics of the responsible non-covalent interactions. Therefore, in this section, the fundamentals of electrostatic, van der Waals, hydrogen bonding and π-π stacking interactions are outlined. Some of these can be attractive or repulsive, while others are strictly attractive.

Electrostatic (or double layer) interactions describe the attraction (or repulsion) of charged species in solution.[134] If the two species are similarly charged, then they will repel each other. Conversely, two oppositely charged species will attract each other. Since DNA is negatively charged (from the phosphate backbone), it will adsorb to positively charged surfaces. While one may be tempted to say the opposite for negatively charged surfaces, there is an important caveat to account for: ionic strength. Consider two negatively charged surfaces in an aqueous solution (Figure 1.8A). Both surfaces will attract counterions which strongly adsorb to its surface (called the Stern layer). Beyond the Stern layer, the counterion concentration decreases until the bulk concentration is reached (called the diffuse layer). In a low ionic strength environment, the diffuse layer is thick and the repulsive electrostatic force between the two surfaces is strong.[135] However, at high ionic strength, more counterions diffuse to the surface and the diffuse layer thickness decreases. This effectively reduces the magnitude of the repulsive force between the two surfaces (called electrostatic screening).[136] As a result, the two negatively charged surfaces may still approach each other. It should be noted that repulsion can only be screened to a certain extent, but not enough to cause attraction; the interaction will still be repulsive. Why then, would the two surfaces still approach each other? The answer lies in the (almost) universal attractive force – the van der Waals interaction.

The van der Waals interaction describes three forces between two atoms or molecules: 1) permanent dipole – permanent dipole (Keesom interactions), 2) permanent dipole – induced dipole (Debye interactions) and 3) induced dipole – induced dipole (London dispersion forces).[137] Molecules such as carbon monoxide have a permanent dipole due to the difference in electronegativity between the atoms. Therefore, upon close approach, the two dipoles may experience repulsion or attraction depending on their orientation – the Keesom interaction (Figure

1.8B, top). A molecule with a permanent dipole may also approach a non-polar molecule and induce a dipole by distorting its electron cloud – the Debye interaction (Figure 1.8B, middle). The Debye interaction is always attractive. Finally, while two non-polar molecules do not have any permanent dipole, their negatively charged electron cloud in an atom constantly fluctuates in size around the positively charged atomic nucleus. Consequently, there can be the generation of temporary dipoles where the nucleus is spatially displaced from the electron cloud. If two of these transient dipoles approach each other, there will be a small, attractive interaction between them – the London dispersion force (Figure 1.8B, bottom).[138] All three interactions are very short-range (<5 nm), and its magnitude increases significantly with decreasing distance between the two dipoles. Mathematically, the three types of van der Waals interactions are considered together and is material-dependent (described by its Hamaker constant).[139]

The attractive van der Waals forces combine with repulsive electrostatic forces and are described by Derjaguin Landau Verwey Overbeek (DLVO) theory.[140] The sum of these interactions between two surfaces is shown in Figure 1.8C. If the surface charge is high, then the electrostatic repulsion will be higher than the attractive van der Waals interaction, resulting in a force barrier preventing the two surfaces from touching. However, if the surface charge is low, then the van der Waals attraction will overcome this electrostatic repulsion and the surfaces can approach each other (at the primary minimum). Beyond this primary minimum, electron clouds overlap which causes significant repulsion that cannot be overcome. Higher ionic strength has the same effect on the net interaction as decreasing surface charge. The sum of these two forces also gives rise to a secondary minimum that is some distance away from electron cloud overlap. If the repulsion cannot be overcome, the particles will stay in this state (called aggregation or flocculation, depending on the context).[141] Agitation of the solution will disperse the particles temporarily, but with time will return to this aggregated state. While DLVO theory is not perfect,[142,143] it continues to be the standard model of describing interactions at the colloidal domain.

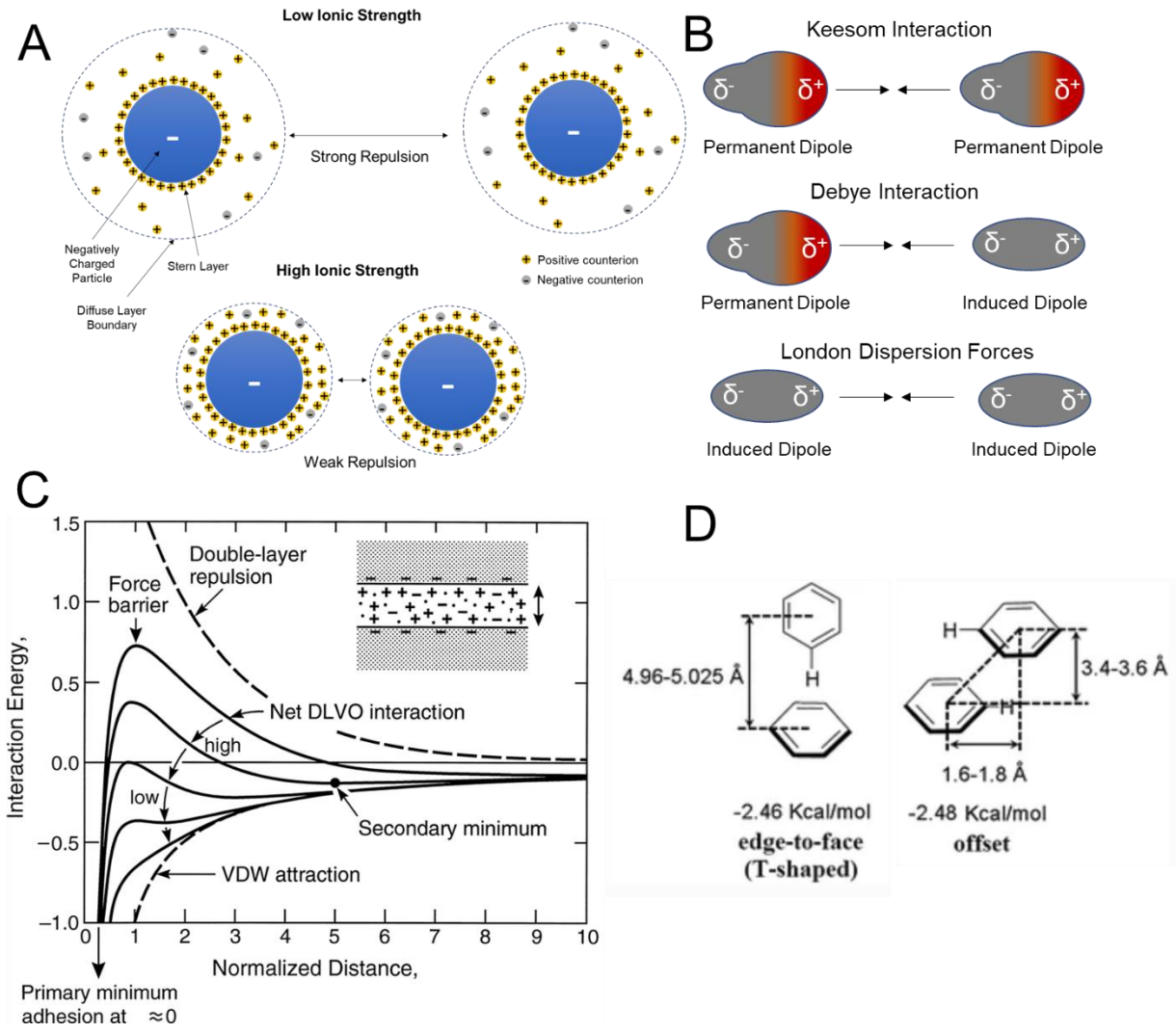

Figure 1.8. Overview of the main intermolecular forces observed in DNA/nanomaterial interactions. Increased ionic strength results in a decreased electrostatic force. If the two nanomaterials are of the same charge, then this force will be repulsive. (B) The three types of van der Waals interactions: Keesom, Debye and London dispersion forces. (C) The sum of the attractive van der Waals force and repulsive electrostatic force as a function of distance, described by DLVO theory. Image reproduced from ref.[140] with permission. Copyright © 2001 Cambridge University Press. (D) The two most stable conformations of the π – π interaction: T – shaped and parallel-displaced (offset). Image reproduced from ref.[144] with permission. Copyright © 2015 Springer Nature Switzerland AG.

We will also discuss two other interactions usually observed with nanomaterial/DNA systems: hydrogen bonding and $\pi - \pi$ stacking. Many consider hydrogen bonding a special case of electrostatic interaction where hydrogen bridges the interaction between two atoms of high electronegativity.[145] One of the atoms (called the "donor") has a covalent bond with hydrogen. Since the electronegative atom pulls electron density from hydrogen, this bond is polarized.[146] Examples of hydrogen bond donors are hydroxyl (R-OH) and amine ($R\text{-}NH_2$) groups. The other atom (called the "acceptor") is simply an electronegative atom with a free lone pair. The partial negative charge on the acceptor is attracted to the partial positive charge on the hydrogen atom, resulting in the formation of a bond. Examples of acceptors can be oxygen (O), nitrogen (N) or fluorine (F) atoms. Such attractive forces are important in DNA hybridization. It is therefore understandable that they also play a part at the DNA/nanomaterial interface. Finally, $\pi - \pi$ stacking is an attractive interaction between aromatic rings.[147,148] Experimentally, it has been observed that the most favourable conformations (lowest interaction energy) are either the T-shaped or parallel-displaced (offset) arrangements (Figure 1.8D).[149] It has been suggested that the delocalized electrons in the aromatic rings act like a negative charge. The carbon atoms on the edge of the ring are electron donating groups and are therefore a positive charge. Therefore, these two orientations would maximize the attraction between the two rings. Like hydrogen bonds, these interactions are also critical to DNA hybridization and are therefore useful for adsorption on nanomaterials.

1.4.4 Mechanism of DNA adsorption on GO

As mentioned earlier, DNA can adsorb on nanomaterials through a variety of non-covalent interactions. GO and CeO_2 represent two classes of materials that adsorb DNA through different mechanisms. For GO, there are two main modes of attraction: hydrogen bonding and π-π stacking.[114,150] This hydrogen bonding occurs between the hydroxyl/carboxyl/ether groups on GO and the bases/phosphate on DNA. This type of interaction is localized to hydrophilic regions on GO. At low pH, this binding is enhanced due to protonation of carboxyl groups on GO, as well as protonation of some DNA bases (notably C, but also G and A to a lesser extent).[151] Since the DNA bases are conjugated systems, they can also favourably stack with aromatic regions on GO.[152] For this reason, purine-rich strands tend to adsorb more strongly to GO than pyrimidine-rich strands (with the exception of poly-C, which will be discussed below).[153,154] Simulations utilizing random DNA strands have showed that DNA spreads out on the GO surface to maximize attractive interactions in hydrophilic regions, but is more compacted in hydrophobic regions (Figure

1.9A).[155] More recent insight has shown that DNA localization on the GO surface is also temperature-dependent; heating drives the GO towards more hydrophobic regions, freezing drives it to hydrophilic regions.[156] For heating, the driving force is entropy due to increasing hydrophobicity of the DNA strand with temperature. In the cooling case, there is elongation of the DNA strands resulting in more hydrogen bond contact points in the oxidized regions. It should be mentioned that, due to both DNA and GO being negatively charged at neutral pH, a moderate ionic strength (> 0.1 M) is needed for both the hydrogen bonding and π – π stacking interactions to overcome the repulsive electrostatic forces. Furthermore, since the bases are very important for DNA adsorption on GO, single-stranded DNA has a much higher affinity than double-stranded DNA.[157]

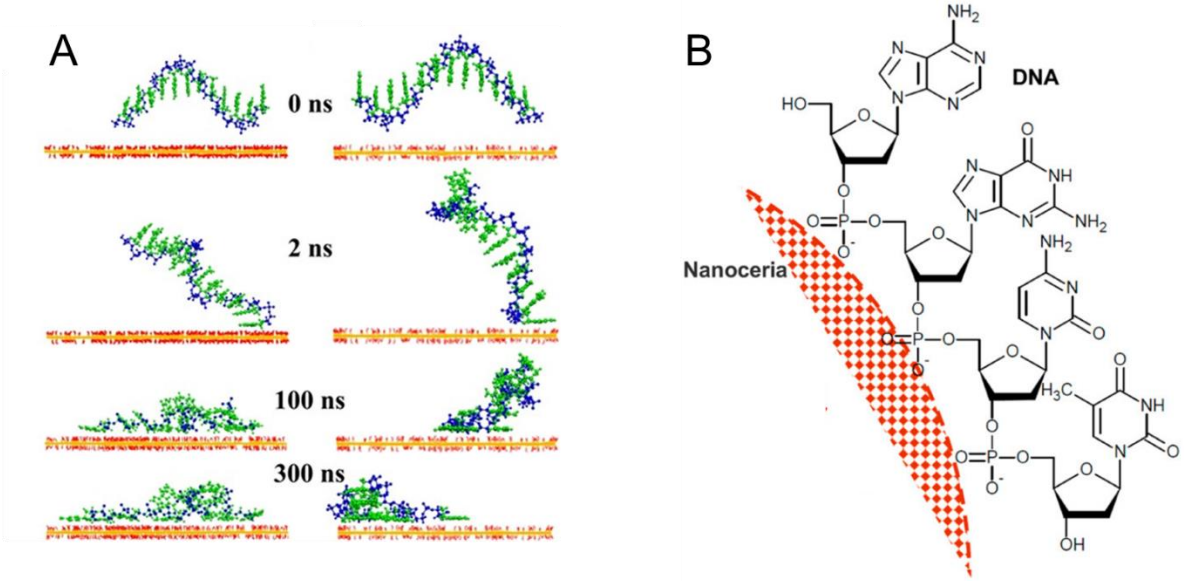

Figure 1.9. Mechanism of DNA adsorption on GO and metal oxide nanoparticles. (A) Simulations of single-stranded DNA adsorption on GO as a function of time on hydrophilic (left) and hydrophobic (right) regions. Image reproduced from ref.[155] with permission. Copyright © 2017 John Wiley and Sons Inc.. (B) Adsorption of single or double stranded DNA on nanoceria, emphasizing the attractive electrostatic interactions between the phosphate backbone and the nanoparticle surface. Image reproduced from ref.[158] with permission. Copyright © 2013 American Chemical Society.

1.4.5 Mechanism of DNA adsorption on Metal Oxides

Unlike GO, DNA adsorbs to metal oxide nanoparticles predominantly through attractive electrostatic and Lewis acid/base interactions between surface metal ions and the negatively charged phosphate backbone of DNA (shown with CeO_2 in Figure 1.9B).[133] While these metal oxides have an overall weak negative surface charge (as mentioned above) at neutral pH, this can be overcome with a relatively low ionic strength (simply 10-50 mM buffer without additional salt) environment which gives DNA access to the nanoparticle surface. An excess of free orthophosphate or other negatively charged species can easily displace DNA from these surfaces..[159] On the other hand, an excess of individual nucleobases (adenine, guanine, etc.) cannot displace DNA, indicating the lack of involvement of the DNA bases on adsorption. For this reason, there is a much smaller variation in the strength of adsorption by base type (unlike GO), as well as hybridization state (single-stranded vs double-stranded).

1.5 Fluorescence-based Biosensor development using GO/DNA conjugates

Biosensors utilizing both GO and DNA have been implemented using several methods. Some exploit its unique electronic properties in current- or impedance-based designs. However, GO can also quench the fluorescence of organic fluorophores once they are in proximity to each other (in a similar way to organic quenchers described in section 1.3). Therefore, fluorescence-based sensor designs have been quite popular in the last decade.[160] The basic implementation is shown in Figure 1.10A, where a fluorophore labeled probe DNA is adsorbed on the surface of the GO resulting in quenched fluorescence. Addition of target/heat/competing ligands causes desorption of the probe DNA, formation of the probe DNA/target complex and recovery of the fluorescence.[161] Early research using this method was confined to cDNA detection. However, this was later expanded for non-DNA targets. For example, in 2014 our group utilized a FAM-labelled adenosine aptamer/GO system for the detection of adenosine.[112] The sensor displayed a region of linear response, with a limit of detection of 0.028 mM. This recovery was selective for adenosine and adenosine phosphates; other nucleobases or nucleotide phosphates could not induce this desorption. Similar biosensors have been designed using different aptamers for the detection of different types of cells,[162,163], human chorionic gonadotropin,[164] adenosine triphosphate (ATP),[165–167] alfatoxin B1,[168] the prostate specific antigen,[169] and bisphenol A.[170]

A more complicated version of this technique utilized several labelled DNA sequences with different affinities to various proteins (Figure 1.10B). Since each DNA was labelled with a unique fluorophore, the addition of a target protein elicited a unique combination of fluorescence signals. Through statistical analysis (Figure 1.10C), many proteins were tested and selectively distinguished from one another. Sensing capabilities were retained even in environments of high interference (i.e., human serum), showing the robustness of the method.

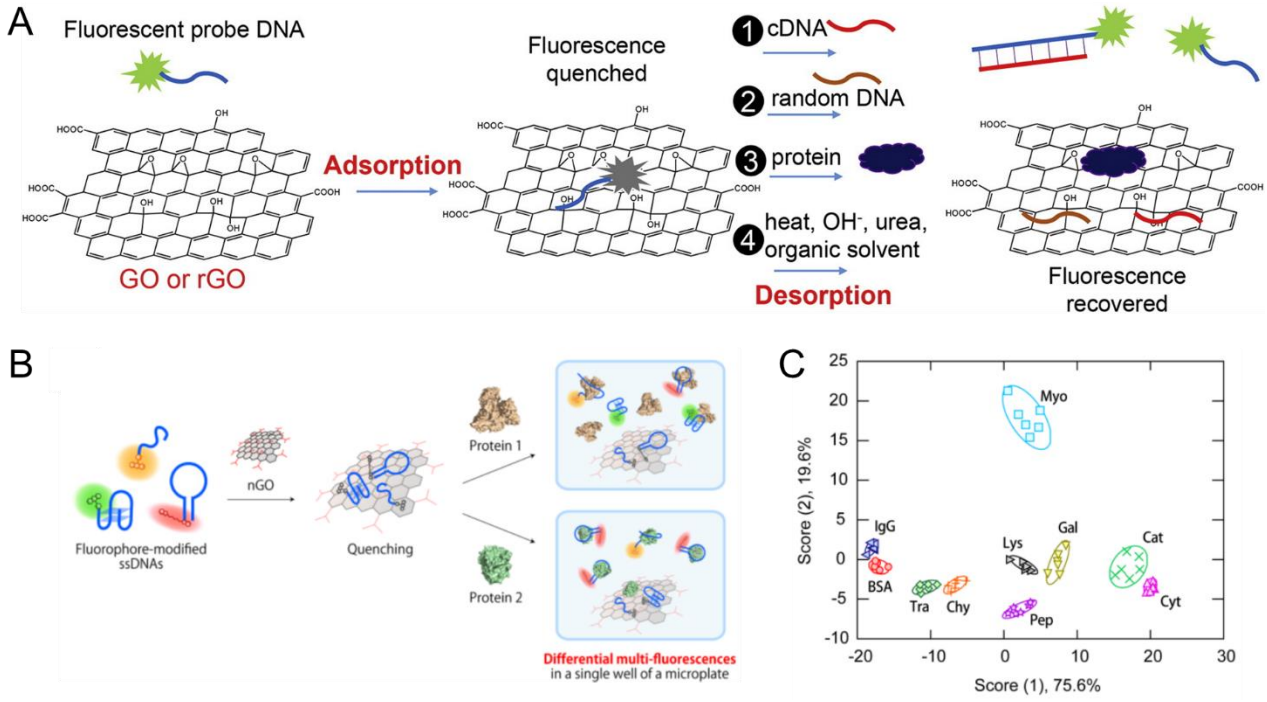

Figure 1.10. Biosensor designs for GO/DNA systems. (A) General scheme for the target detection using fluorescent probe DNA and GO. Upon mixture, the probe DNA adsorbs on GO, quenching fluorescence. Addition of the target or changing the solution conditions causes desorption of DNA and recovery of the fluorescence. Image reproduced from ref.[113] with permission. Copyright © 2016 Elsevier B.V.. (B) Scheme of detection of various proteins using various labelled DNA probes. Upon adsorption, the probe DNA are quenched. After the addition of a protein, strands with varying affinities to the protein will desorb to different degrees, yielding a unique combination of signals. (C) Linear canonical discriminant plot showing statistical groupings of different proteins using the method in (B). Image reproduced from ref.[171]. Creative Common CC BY License.

1.5.1 Addressing Non-Specific Displacement of DNA from GO

Apart from the protein example shown above, the detection scheme outlined in Figure 1.10A can only work well in clean, controlled buffer conditions. The picture becomes more complicated for specific targets (e.g., adenosine or metals) in complex media (such as human serum or lake water). While DNA indeed has a high affinity for GO, proteins and other macromolecules also have similar affinities and can displace DNA from its surface.[114] This significantly decreases biosensor specificity. To address this, two strategies (to date) have been implemented. First, a labelled non-binding strand (an internal standard) can be adsorbed simultaneously with the labelled binding probe strand (Figure 1.11A). Then, after addition of target, the fluorescence of desorbed probe and standard strands can be measured separately. The difference between these two intensities in the absence or presence of target is less sensitive to competing targets, improving specificity. This method has been used to detect ATP in cells with and without production enhancement by the addition of Ca^{2+} or etoposide.[172] The second method is to co-adsorb a non-labeled, non-binding blocking strand along with the labeled binding strand (Figure 1.11B).[173] The amount of the blocking strand is added in large excess compared to the binding strand. Therefore, non-specific displacement would more likely affect the blocking strand rather than the binding strand. Addition of target will more selectively interact with labelled probe DNA. This blocking strand need not be DNA; effective blocking has been achieved using various polymers and proteins.[174]

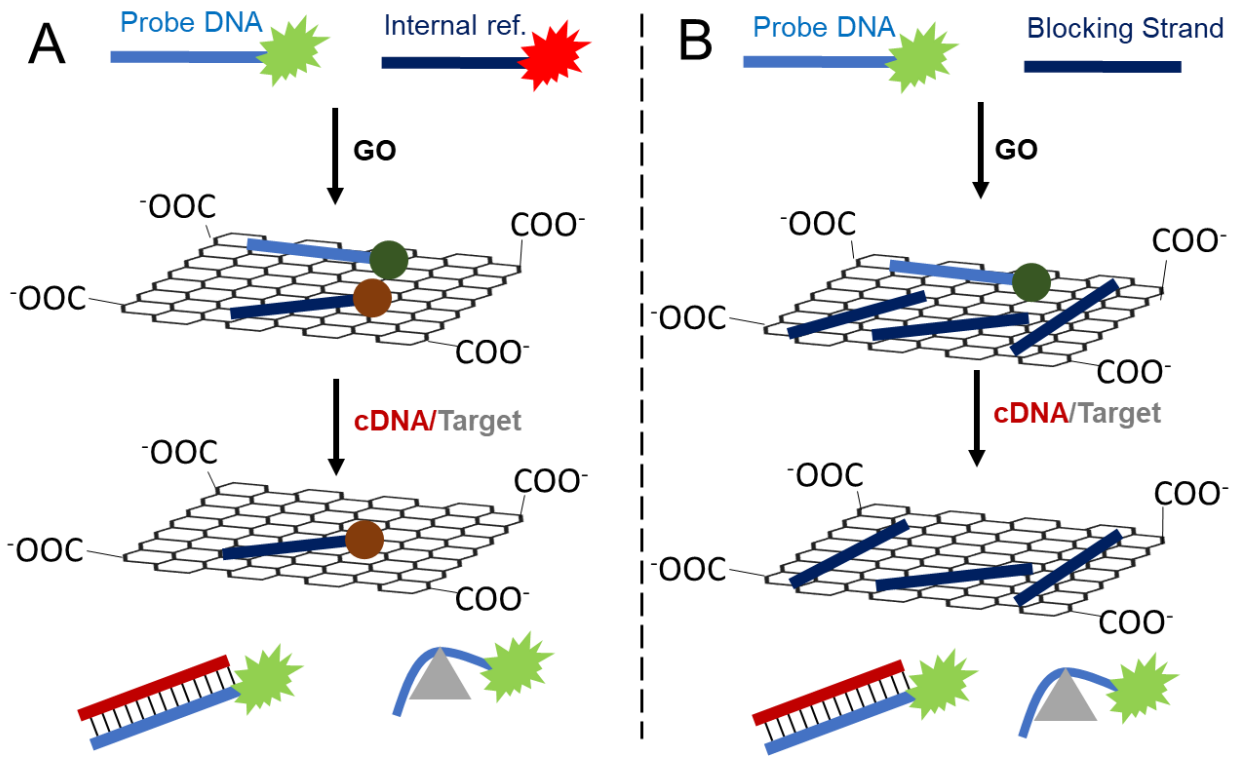

Figure 1.11. Strategies to overcome non-specific displacement of DNA. (A) Co-adsorption of a labelled internal standard that probes non-specific adsorption, as well as a labelled test strand that probes target binding. The difference between the two intensities can provide enhanced specificity to the target. (B) Co-adsorption of an excess of non-labelled blocking strands with the labelled probe strand. The blocking strand would be more likely to be displaced by non-specific interactions, leaving the probe strand more susceptible to target interactions.

1.5.2 Improving Sensor Kinetics by Inhibited DNA Adsorption

The kinetics of adsorption is typically fast (a few minutes) for DNA on GO under optimal reaction conditions.[114] However, the desorption step is much longer (~30 minutes). Due to this, sensors have been designed that utilize adsorption instead of desorption as the key step. Such a sensor would pre-mix the target and the probe DNA, followed by the addition of GO. If the target was present, adsorption would be inhibited, and the fluorescence would remain high. In the absence of target, the single stranded probe DNA would easily adsorb on GO, quenching fluorescence. Early work by He et al. utilized this adsorption-based sensor to great effect,[175] affording a limit of detection for cDNA of 0.1 nM, which was even lower than conventional probe/GO pre-mixing.

An interesting development of this method was shown to simultaneously detect 3 metals: Cu^{2+}, Mg^{2+} and Pb^{2+} (Figure 1.12A). The DNA probe consisted of an amalgamation of three DNAzymes, each selective to one of the three metals. Upon metal binding, a cleavage reaction occurs, releasing a unique fluorophore labelled single strand that can adsorb on GO, quenching its fluorescence. If the metal was not present, The DNAzyme superstructure would remain intact, and fluorescence would stay high. A detection limit of 1 nM, 200 nM and 0.3 nM for Cu^{2+}, Mg^{2+} and Pb^{2+}, respectively, was obtained with very good selectivity (Figure 1.12B).

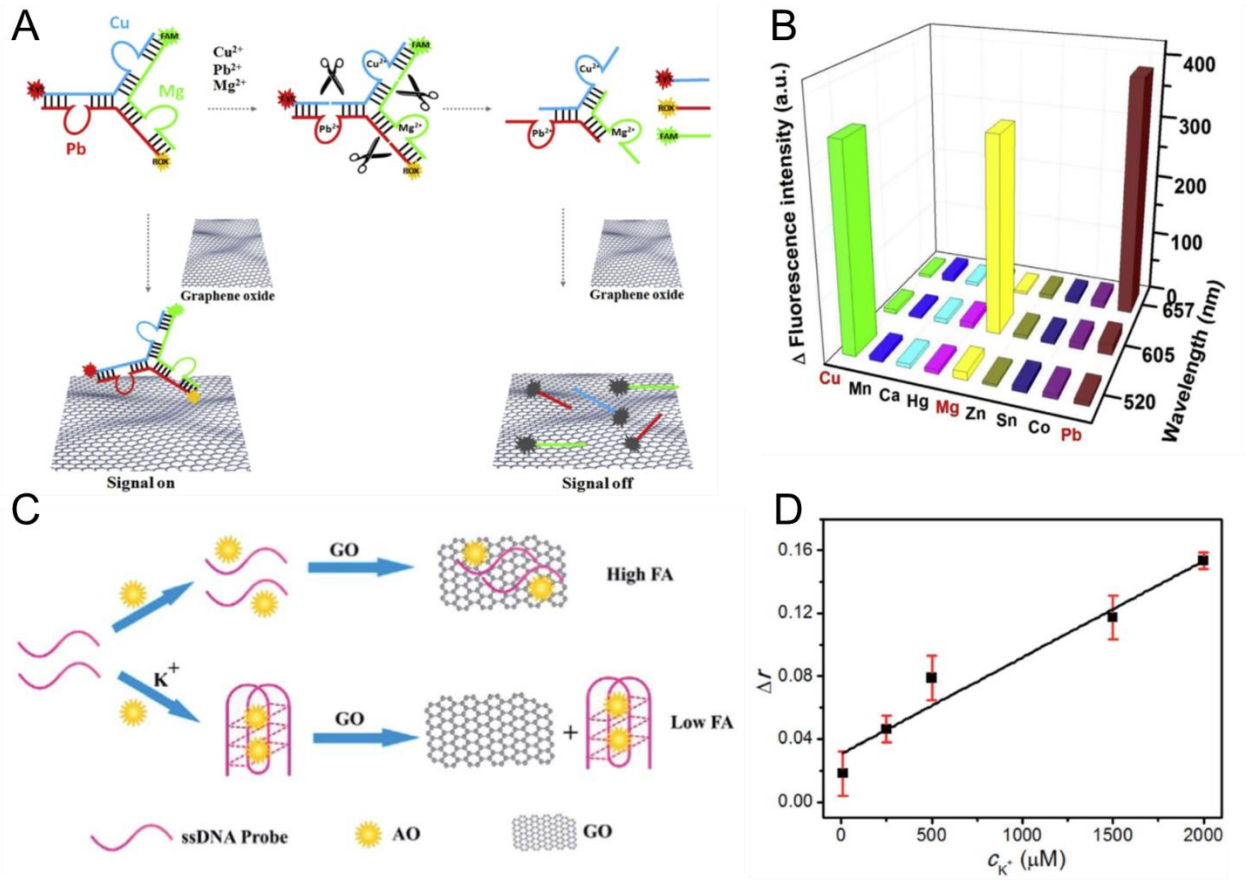

Figure 1.12. DNA biosensor designs based on inhibited adsorption on GO. (A) Scheme of a triple DNAzyme junction for the simultaneous detection of three metals. In the presence of one (or all) of the targets, the DNAzyme cleaves a fluorophore labelled substrate from the superstructure, allowing it to adsorb on GO, quenching fluorescence. In the absence of the targets, the hybridized structure limits its adsorption on GO and fluorescence remains high. (B) Selectivity of the sensor to different metals at the different emission wavelengths (for each fluorophore). Image reproduced from ref.[176] with permission. Copyright © 2017 Elsevier B.V.. (C) Scheme of a K^+ sensor utilizing

the staining properties of acridine orange in a fluorescence anisotropy assay. In the presence of K^+, a G-quadruplex forms, and acridine orange intercalates, preventing adsorption on GO. The anisotropy remains low. However, in the absence of K^+, both the DNA and acridine orange adsorbs on GO, increasing fluorescence anisotropy. (D) Linear range of K^+ detection using this anisotropy sensor. Image reproduced from ref.[177] with permission. Copyright © 2015 Royal Society of Chemistry.

Anisotropy-based sensors have also been developed using this type of method. Such sensors typically utilize DNA-binding dyes (such as SYBR Green or acridine orange). An example of this is shown in a K^+ sensor in Figure 1.12C using acridine orange.[177] If K^+ was present, DNA folded to form a G-quadruplex and acridine orange (AO) preferentially partitions within the structure. Since the DNA is folded, adsorption on GO is hindered and anisotropy is low. In the absence of K^+, both DNA and the dye adsorb on GO and the anisotropy is high. A detection limit of 1 μM was obtained for K^+ (Figure 1.12D). Other implementations of a similar method have been used to detect C-reactive protein, Hg^{2+}, and tropomyosin.[178–180]

1.5.3 Diblock Sensor Designs and the "Problem" of Poly-C Adsorption

Sometimes, researchers wish to minimize the interaction of the probe DNA with GO. Therefore, biosensors have been developed with diblock DNA. In such cases, one block is anchored to the GO surface, while the other block (typically an aptamer or cDNA) participates in target binding. Early examples of such sensors utilized transmittance[181] and electrochemiluminescence[182] rather than fluorescence for DNA detection. However, implementations of fluorescence sensors using diblock DNA have found a niche with anisotropy-based measurements. Anisotropy can be rendered as an unreliable indicator of probe DNA adsorption in quenching environments (a concept explored in Chapter 5 of this thesis). Therefore, if the fluorophore is kept a sufficient distance from GO, fluorescence would not be quenched significantly. This was explored by Xiao et al. for the detection of ricin B-chain (Figure 1.13A).[183] To begin with, a magnetic bead was conjugated with the ricin B-chain aptamer, which is partially hybridized with a small blocking strand. Upon addition of ricin B-chain, it displaced the blocking strand. Simultaneously, a diblock DNA with a poly-A anchoring block was partially hybridized with a dye-labelled probe strand (complementary to the blocking strand) and adsorbed on GO. The now-liberated blocking strand

fully hybridizes with the dye-labelled probe strand, which is released from the GO surface. Upon digestion with exonuclease III, the result is a free fluorophore with low anisotropy. On the other hand, if target was not present, then the probe DNA remains partially hybridized to the diblock DNA, and anisotropy was high. A detection limit of 400 ng/mL was obtained for ricin B-chain (Figure 1.13B). This same group used a simpler method to detect adenosine,[184] while developing a more complicated method to detect microRNA.[185]

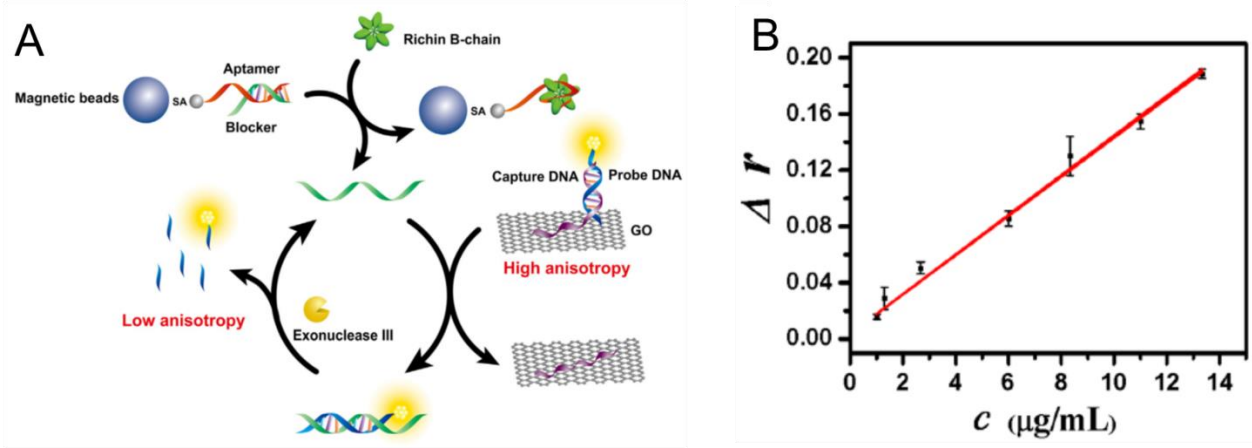

Figure 1.13. A diblock anchoring design for DNA detection. (A) General scheme of ricin B-chain detection using anchored DNA. The ricin B-chain aptamer is conjugated to magnetic beads and partially hybridized with a blocking strand. In a separate solution, the labeled probe DNA is partially hybridized with the anchored capture DNA (high anisotropy). In the presence of ricin B-chain, the blocking strand is displaced from the aptamer. This blocking strand fully hybridizes with the probe DNA, removing it from the GO surface. Exonuclease III degrades the probe strand, yielding a fluorophore of low anisotropy. The blocking strand can then react with another anchored probe DNA. (B) Linear response of this anchored DNA system to ricin B-chain concentration. Image reproduced from ref.[183] with permission. Copyright © 2016 Elsevier B.V..

The anchoring DNA used in the above reports were purine (poly-A or poly-G)-rich, supported by theoretical studies that such nucleotides adsorb more strongly on GO. However, in 2017, our group performed a comprehensive screen of DNA adsorption on 2D nanomaterials (included GO) and inorganic metal oxides using fluorescence spectroscopy.[186] For almost all nanomaterials, poly-C (in this case, C_{15}) displayed the highest affinity for adsorption. If A_{15}, T_{15}

or G_{15} was adsorbed (using GO as an example), C_{15} displaced the most DNA from the surface (Figure 1.14A, B and D, respectively). If C_{15} was adsorbed, then only excess C_{15} could significantly displace it from GO (Figure 1.14C). This was more generally observed with most other nanomaterials (Figure 1.14E). Such an observation is difficult to explain, as cytosine is not significantly different from thymine in chemical structure, yet the former adsorbs much more strongly than the latter on GO (if incorporated into DNA). Some preliminary experiments with carbon-based materials (GO and carbon nanotubes) suggested the unique ability of poly-C to form the i-motif played some part in this observation.

A later study from our group explored the properties of poly-C anchoring groups on GO.[187] It was seen that the length of this anchoring block did not reduce the density of adsorbed blocks on GO. Poly-C anchoring blocks also showed significant resistance to various species that disrupt adsorption (such as urea, bovine serum albumin, polyethylene glycol, etc.) compared to poly-A blocks. However, an explanation for this was not provided here either.

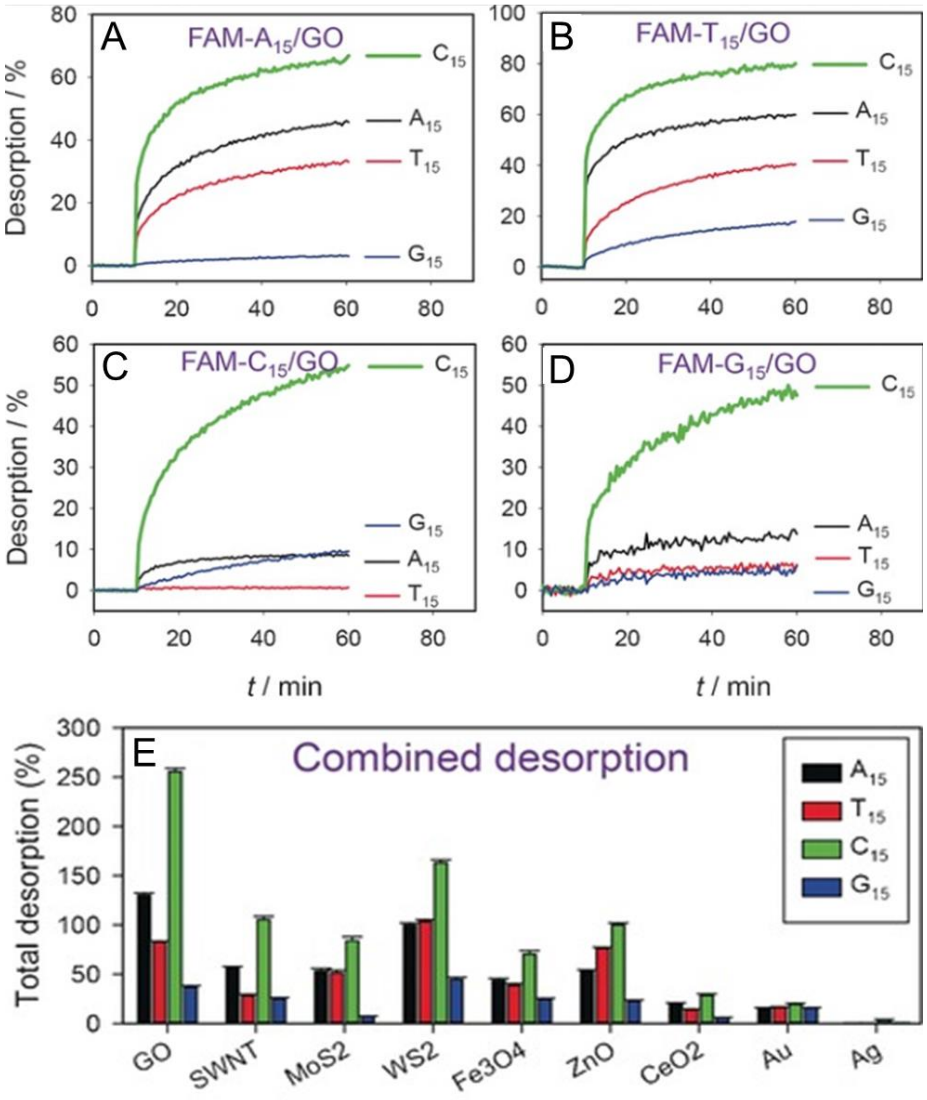

Figure 1.14. The high affinity of poly-C DNA to various nanomaterials. Addition of 15-mer DNA to (A) FAM-A_{15}, (B) FAM-T_{15}, (C) FAM-C_{15}, and (D) FAM-G_{15} adsorbed on GO. In all cases, C_{15} induced the most desorption. (E) Response of adsorbed FAM-T_{15} on different nanoparticles to the four DNA homopolymers. For all nanoparticles, C_{15} was able to induce the most desorption. Image reproduced from ref.[186] with permission. Copyright © 2017 John Wiley and Sons Inc..

1.6 Fluorescence Biosensors Based on Metal Oxide/DNA conjugates

Similar biosensor designs to GO/DNA have also been utilized for metal oxide nanoparticles (since they are mostly quenching surfaces – with some exceptions), but reports are more limited. Our group showed that adsorbing labeled DNA on multiple metal oxide nanoparticles can be used to

detect target complementary DNA with good selectivity and sensitivity.[18] Certain metal oxides, such as NiO, adsorbed DNA more strongly (due to their positive charge at neutral pH) and performed slightly better than others. The limit of detection for cDNA was in the range of 0.3 nM, similar to that of GO. Sensor performance was not significantly compromised in complex environments, with cDNA being detected sensitively even in human serum (detection limit of 0.25 nM for NiO).

Metal oxide nanoparticles have been utilized for non-DNA targets as well. Our group used FAM-labelled DNA homo-oligomers on CeO_2, $CePO_4$ and Fe_3O_4 to probe desorption by arsenate (Figure 1.15A). Sensitive detection was obtained with CeO_2 (Figure 1.15B), with a calculated limit of detection of 29 nM. Despite this, it was not particularly selective; both phosphate and arsenite also showed fluorescence recovery upon addition to these conjugates (Figure 1.15C). The reason for this non-selectivity lies with the adsorption mechanism; any ligand that can effectively compete with DNA for adsorption can displace it if its concentration is high enough.[133] For this reason, metal oxide nanoparticles are not as useful as GO in aptamer-based biosensor development. Instead, DNA can probe inorganic ligand affinity with these metal oxides, which has been utilized significantly by our group in recent years.[17,159,188,189] Still, they serve as a good comparison to GO due to this difference in this adsorption mechanism (as we will see in Chapter 2).

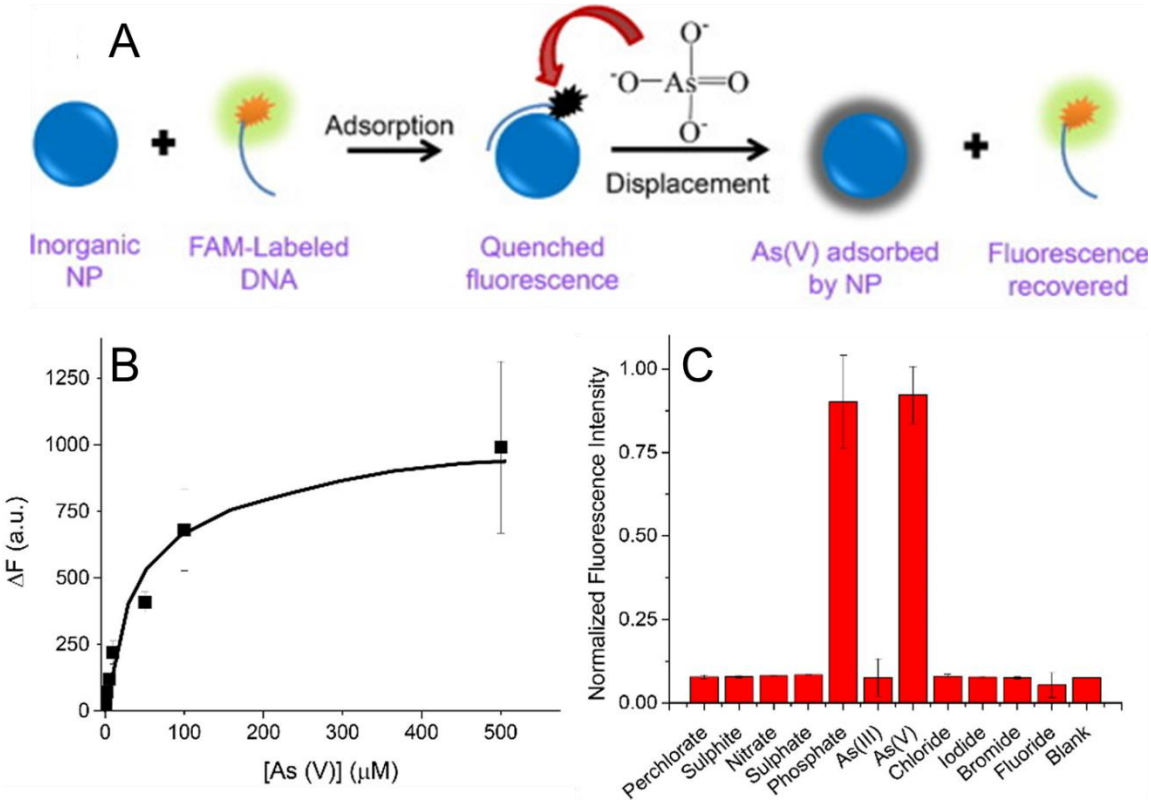

Figure 1.15. A biosensor utilizing metal oxide nanoparticles. (A) General scheme of arsenate detection using inorganic nanoparticles. FAM-labelled single-stranded DNA was adsorbed on the nanoparticle, quenching fluorescence. The addition of arsenate displaces DNA, increasing fluorescence. (B) Response of sensor to increasing arsenate concentration. (C) Selectivity of sensor response. Only arsenate and phosphate cause any fluorescence recovery. Image reproduced from ref.[190] with permission. Copyright © 2017 Elsevier B.V..

1.7 Thesis Goals and Outline

In this Chapter, we have examined the fundamental concepts, sensor design and current state of the art of DNA/nanomaterial fluorescent biosensors. While this field has experienced tremendous growth in recent years, there is still a need to understand underlying mechanisms and behaviours that make these sensors possible. Therefore, we aimed to solve some of these problems during work I undertook over the past 4 years. The body of this thesis is divided into 4 Chapters, each contributing new insight into nanomaterial/DNA fluorescent biosensors. It should be noted that Chapters 3 and 4 relate to each other insomuch as it focuses on poly-C DNA interactions with GO,

whereas Chapters 2 and 5 are works concentrating on desorption mechanisms and artifacts of polarization, respectively.

In Chapter 2, we start with comparing the desorption of the adenosine aptamer from CeO_2 and GO in response to differ. We find that, for GO, target/aptamer interactions dominate. Only adenosine, adenosine phosphates and complementary DNA can induce desorption. Non-targets have little to no effect on the adsorbed aptamer. On the other hand, for CeO_2, desorption does not occur in response to adenosine. Instead, desorption only occurs with target molecules that can more readily displace DNA (except for cDNA). This was seen not only for CeO_2, but for other metal oxide nanoparticles like Fe_3O_4, ZnO, NiO and TiO_2 which adsorb DNA in a similar way.

In Chapter 3, we begin our exploration of poly-C adsorption on GO by studying the properties of FAM-labelled C_{15} itself. We find that FAM-C_{15} as-purchased can fold into an i-motif at neutral pH. Once heated, we see a sharp increase in fluorescence around the melting temperature, indicating the unfolding of the i-motif. The structure does not reform upon cooling and the melting is therefore irreversible. In addition, the unfolded FAM-C_{15} adsorbs even stronger on GO than folded FAM-C_{15}. Finally, if folded FAM-C_{15} is adsorbed on GO, some of it unfolds either upon adsorption to or desorption from GO. While this provided insight into dye-poly-C interactions, it did not show why poly-C adsorbs stronger on GO compared to other DNA homo-oligomers.

In Chapter 4, we continue our investigations on poly-C/GO interactions by adsorbing model pH-insensitive Alexa-labelled DNA (a random 12-mer or T_{15}) on GO and adding varying C-containing DNA to desorb it. While poly-C adsorbs strongest of the 4 bases at neutral pH, it is among the weakest at pH 4 (where the i-motif is stabilized naturally). This agrees with findings in Chapter 3 that the i-motif actually adsorbs weaker than unfolded C_{15}. Using molecular dynamics simulations, we determine that the reason for strong poly-C/GO adsorption is the lack of intrastrand interactions within poly-C (maximizing interactions with GO), rather than any secondary structure (which would minimize interactions with GO).

In Chapter 5, we explore a relatively new technique for studying DNA/GO interactions: fluorescence polarization. We see that polarization is artificially increased when the fluorescence intensity is near the detection limit of the instrument. This was achieved by lowering FAM-DNA concentrations or by lowering the pH of the solution (as FAM has a pH-dependent fluorescence). Therefore, for a quenching surface like GO, an increase in polarization upon mixing with DNA is

likely due to the low concentration of free FAM-DNA, rather than adsorption. For a non or weakly quenching material (such as Y_2O_3), increase in polarization can be more correlated to adsorption. We then derive an equation that can describes how the fluorescence polarization can depend on the both the quenching and adsorption efficiency of a specific nanomaterial.

Chapter 2 - Nanomaterial and Aptamer Based Sensing: Target Binding Versus Target Adsorption

The results presented in this Chapter have been published as:

Anand Lopez and Juewen Liu. "Nanomaterial and Aptamer-Based Sensing: Target Binding versus Target Adsorption Illustrated by the Detection of Adenosine and ATP on Metal Oxides and Graphene Oxide". *Analytical Chemistry* **2021**, 93, 5, 3018–302.

2.1 Introduction

Pre-adsorption of fluorescently-labelled DNA oligonucleotides on nanomaterials is a popular method of sensing.[17,113,191,192] Such DNA oligonucleotides are typically used for the detection of complementary DNA (cDNA), and they can also be aptamers to detect metal ions, small molecules and proteins.[82,193] Most of the work utilizing fluorescence take advantage of the fluorescence quenching property of nanomaterials upon DNA adsorption.[194–197] The assumption is that target molecules can bind with the DNA probe to desorb it from the nanomaterial, resulting in fluorescence enhancement.[198–201]

For this sensing mechanism to happen, the probe DNA cannot be adsorbed too strongly. Otherwise, aptamer binding interactions cannot compete with the aptamer adsorption, leading to poor sensitivity. For example, DNA absorbs on gold nanoparticles (AuNPs) *via* coordination with the DNA bases, which is quite strong; often only ~1% of pre-adsorbed DNA probe can be desorbed in the presence of target DNA or target molecules.[111,202] Another example is carbon nanotubes, where DNA can wrap around nanotubes via hydrophobic and π-π stacking interactions. In one case, it took more than 10 h for the adsorbed probe DNA to desorb, which is not viable for a biosensor.[203] In this regard, graphene oxide (GO) is a better choice since it interacts with DNA less strongly, and DNA can be quickly desorbed by its target molecules.[113,204–206]

Recently, metal oxide nanoparticles (MONPs) with interesting magnetic, catalytic and fluorescence quenching properties have also been used for designing DNA-based biosensors.[18,133,159,176,189,190,207–209] The phosphate backbone of DNA is responsible for interacting with the metal ions on MONPs.[133] Many MONPs have enzyme-like catalytic activities, making them analytically attractive.[210–212] For example, Fe_3O_4 has peroxidase-like activity, while CeO_2 has oxidase-like activity. DNA adsorption was used to modulate their catalytic activities, which in

turn was used for detection.[209,213] Target-induced aptamer desorption from MONPs has been assumed to be due to aptamer binding, while the potential of target molecule interaction with MONPs has not been considered. We recently observed that the adsorption of many target molecules on AuNPs governed this sensing mechanism.[111] If a target molecule can bind strongly to a nanomaterial, then it may compete with or even supersede probe DNA/target interactions. While this has been shown for AuNPs, no studies have focused on MONPs to date.

Herein, we investigated competitive target/aptamer and target/nanomaterial interactions on various MONPs. We employed a 27-mer DNA aptamer that can bind adenosine and adenosine triphosphate (ATP), since we can systematically test different target molecules.[51,201] ATP has a triphosphate and it can strongly adsorb on many MONPs, while adenosine does not have phosphate-based adsorption. For all the tested MONPs, we found that ATP can produce a signal, but adenosine cannot, suggesting the dominating effect of target adsorption instead of aptamer binding.

2.2 Materials and Methods

NaCl, $MgCl_2$ and 4-(2-hydroxyethyl)-1-piperazineethanesulfonic acid (HEPES) were purchased from VWR Canada. These were dissolved in Milli-Q water to make buffer A with a strong ionic strength (1 mM $MgCl_2$, 100 mM NaCl and 20 mM HEPES, pH 7.6). Buffer B (moderate ionic strength) contained 100 mM NaCl and 20 mM HEPES (pH 7.6), while buffer C (low ionic strength) contained only 20 mM HEPES (pH 7.6). For GO-related studies, buffer D was prepared using 20 mM HEPES (pH 7.6), 300 mM NaCl and 2 mM $MgCl_2$ (the $MgCl_2$ concentration was varied in some experiments). All DNA sequences (Table 2.1) were purchased from Integrated DNA Technologies (Coralville, IA) and dissolved in water at a concentration of 100 µM. FAM-labelled strands were further diluted to 1 µM stock in water. Adenosine and other nucleosides were purchased from Mandel Scientific (Guelph, ON, Canada). Adenosine triphosphate, guanosine triphosphate, cerium dioxide (CeO_2, 20 wt% dispersion), titanium dioxide (TiO_2), zinc oxide (ZnO) and iron (II,III) oxide (Fe_3O_4) were purchased from Sigma-Aldrich. GO and nickel oxide (NiO) were purchased from ACS Materials LLC. All nanomaterials were dispersed/diluted to a stock concentration of 1 mg/mL in water.

Table 2.1 List of DNA sequences used in Chapter 2.

DNA names	Sequences (5′→ 3′)
FAM-Aptamer	FAM-ACC TGG GGG AGT ATT GCG GAG GAA GGT
FAM-A_{15}	FAM-AAA AAA AAA AAA AAA
Aptamer	ACC TGG GGG AGT ATT GCG GAG GAA GGT
cAptamer	ACC TTC CTC CGC AAT ACT CCC CCA GGT

UV/Vis absorption spectroscopy. To determine the concentration of the nucleotides and nucleotide triphosphates, the absorbance of the stock solutions was measured using an Agilent 8453 spectrometer. The stock was diluted by 500× so that the peak absorbance was below 0.8. This peak absorbance for ATP and adenosine (λ_{max} = 259 nm, ε = 15.9 $mM^{-1}cm^{-1}$) and GTP and guanosine (λ_{max} = 243 nm, ε = 10.4 $mM^{-1}cm^{-1}$) was then used with the Beer-Lambert law to calculate concentration.

Nanomaterial adsorption capacity. To determine the DNA adsorption capacity (either FAM-aptamer or FAM-A_{15}), varying concentrations of nanomaterials (CeO_2, TiO_2, Fe_3O_4, NiO, ZnO and GO) were respectively added to 50 nM DNA (10 nM for GO) in buffer A (buffer D for GO). The total volume of the sample was 100 µL. After a 30 min incubation, the samples were transferred to a 96-well plate and the fluorescence was measured using a microplate reader (Tecan, Spark). The optimal nanomaterial concentration was determined to be when the fluorescence decrease plateaued. FAM fluorescence was monitored by exciting at 485 nm and detecting emission at 530 nm.

DNA desorption. In a typical experiment (using CeO_2 as an example), 1 µL of 1 mg/mL CeO_2 (final concentration: 10 µg/mL) was added to 94 µL of buffer A. Then, 5 µL of 1 µM FAM-aptamer was added (final concentration: 50 nM) and the sample was incubated for 30 min. After incubation, various concentrations of adenosine or ATP were added to induce desorption. The sample was incubated further for 1 h before measurement using the Tecan plate reader. This was repeated using different MONPs/GO or replacing the DNA sequence with FAM-A_{15}. For selectivity experiments, 0.8 mM target (adenosine, ATP, guanosine, GTP, cytidine or thymidine) was added to induce DNA desorption. For DNA detection experiments using CeO_2, the final

concentration of FAM-aptamer was 10 nM and the CeO_2 concentration was 1 μg/mL. For GO, the FAM-aptamer concentration was 10 nM, the GO concentration was 3 μg/mL and the experiments were conducted in buffer D.

DNA desorption calculation. Once the target induced DNA desorption, the following equation was used to calculate %DNA desorption:

$$\%\text{DNA Desorbed} = \frac{F - F_0}{F_{\text{free}} - F_0} \times 100\%$$

where F is the measured signal after target is incubated with probe/MONP (or probe/GO) conjugate, F_0 is the signal of the probe/MONP or probe/GO conjugate only and F_{free} is the signal of free FAM-aptamer or FAM-A_{15}. Error bars seen in all experiments represent 1 standard deviation away from the mean of three identical experiments.

Adsorption/desorption kinetics. For adsorption kinetics, ATP or adenosine (final concentration 0.8 mM) was pre-mixed with FAM-aptamer (final concentration = 50 nM) in buffer A. The fluorescence was measured for 5 min before the addition of 1 μL of 1 mg/mL CeO_2 (final concentration = 10 μg/mL). Fluorescence was further monitored for 55 min before terminating the experiment. For desorption kinetics, the overall process was similar except that FAM-aptamer and CeO_2 were incubated for 30 minutes in buffer A, followed by the addition of adenosine or ATP (final concentration = 0.8 mM).

Dynamic light scattering. All MONPs were dispersed in 1 mL buffer A and the particle size was measured using a Zetasizer Nano (Malvern). The concentrations of CeO_2 was 10 μg/mL, TiO_2, NiO and Fe_3O_4 were 100 μg/mL, and ZnO was 50 μg/mL. All measurements were conducted at 25°C using a scattering angle of 90°.

Transmission electron microscopy. CeO_2 and Fe_3O_4 were dispersed in water at 10 μg/mL and 10 μL was transferred dropwise to a holey-carbon TEM grid. After overnight drying, imaging was conducted in a Phillips CM-10 microscope at 100 kV.

2.3 Results and Discussion

2.3.1 Sensing mechanism of adenosine and ATP on CeO_2 nanoparticles

The secondary structure of the adenosine/ATP aptamer is shown in Figure 2.1A, and it has the strongest binding affinity for adenosine (K_d ~10 µM), while the affinity for ATP (Figure 2.1B) is slightly weaker.[52,214] The aptamer was labeled with a FAM fluorophore and mixed with CeO_2 nanoparticles to achieve quenched fluorescence. The CeO_2 nanoparticles had an average size of ~5 nm and they were extensively characterized in previous works.[215] We first optimized the CeO_2 concentration needed to achieve fluorescence quenching. For 50 nM FAM-aptamer, 10 µg/mL CeO_2 was sufficient to achieve 95% fluorescence quenching (Figure 2.2A), which was used for this study. We then added target molecules to induce aptamer desorption and subsequent recovery of the fluorescence signal. If aptamer binding is the main driving force for its desorption, we would expect a similar signal from both adenosine and ATP (Figure 2.1C). Since ATP has a triphosphate group, it can strongly adsorb on CeO_2 via phosphate/Ce interactions and compete with the DNA aptamer, which may also lead to aptamer desorption (Figure 2.1D). In this case, adenosine may not produce much signal.

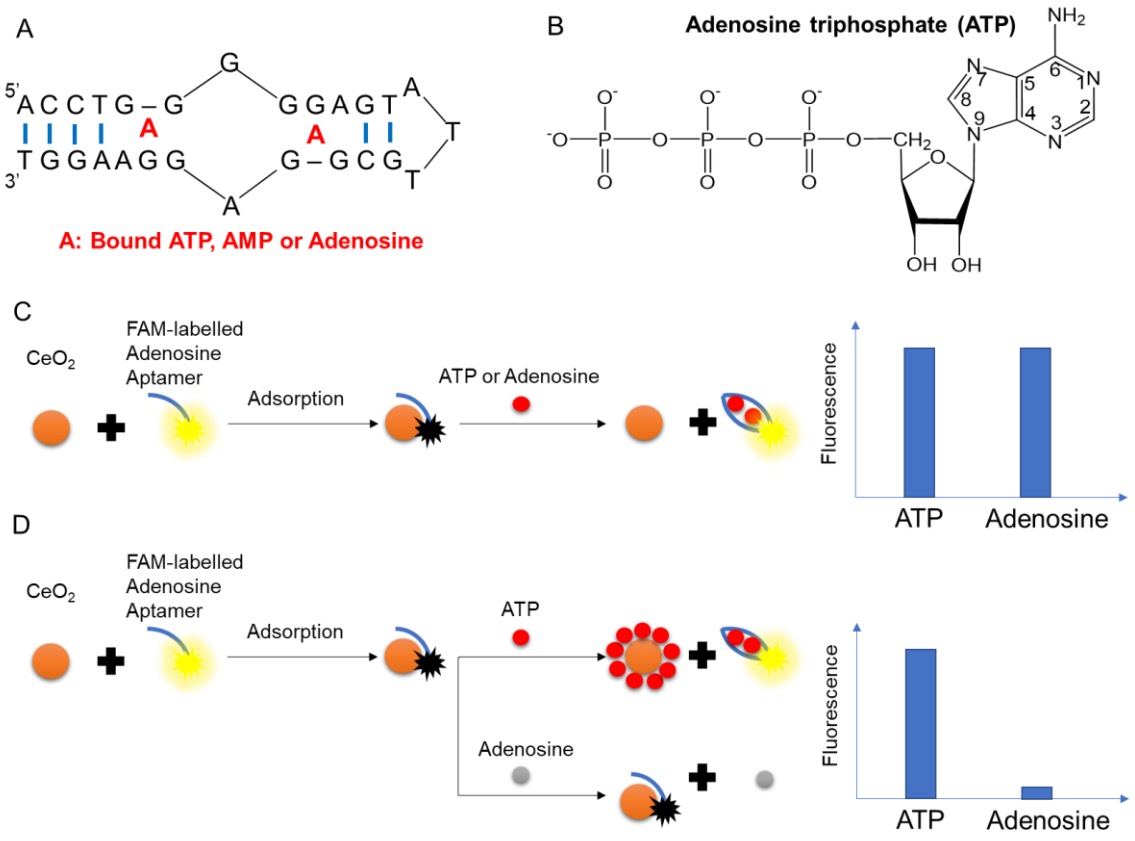

Figure 2.1. Detection schemes: aptamer binding versus target displacement. (A) The secondary structure of the adenosine aptamer, and the two red A letters represent the two target binding sites. (B) Molecular structure of ATP. (C) FAM-labeled aptamer adsorption on CeO_2 and subsequent desorption due to an aptamer binding mechanism, where the addition of ATP and adenosine should both generate the fluorescence signal. (D) FAM-aptamer adsorption on CeO_2 and subsequent desorption due to competitive adsorption from ATP, whereas adenosine does not have strong affinity to CeO_2 and does not generate signal.

In our experiment, we respectively added various concentrations of ATP and adenosine to the FAM-aptamer/CeO_2 conjugate (Figure 2.2B). While a strong fluorescence enhancement was observed with the ATP sample, no increase occurred for the adenosine sample. Even a concentration of 8 µM ATP was enough to desorb ~25% of the aptamer from the CeO_2 surface, and 0.3 mM ATP reached saturated aptamer desorption. Since the K_d of the aptamer is ~10 µM adenosine,[51,52] the total adenosine added would have already saturated aptamer/target binding.

Therefore, the increase of fluorescence by ATP was attributed to the competition between ATP and the DNA on the CeO_2 surface (Figure 2.1D) instead of aptamer binding (Figure 2.1C). This conclusion was confirmed with the addition of GTP and guanosine, where only GTP yielded fluorescence increase (Figure 2.2C). Since this aptamer cannot bind either guanosine or GTP, our results supported the surface-competition mechanism.

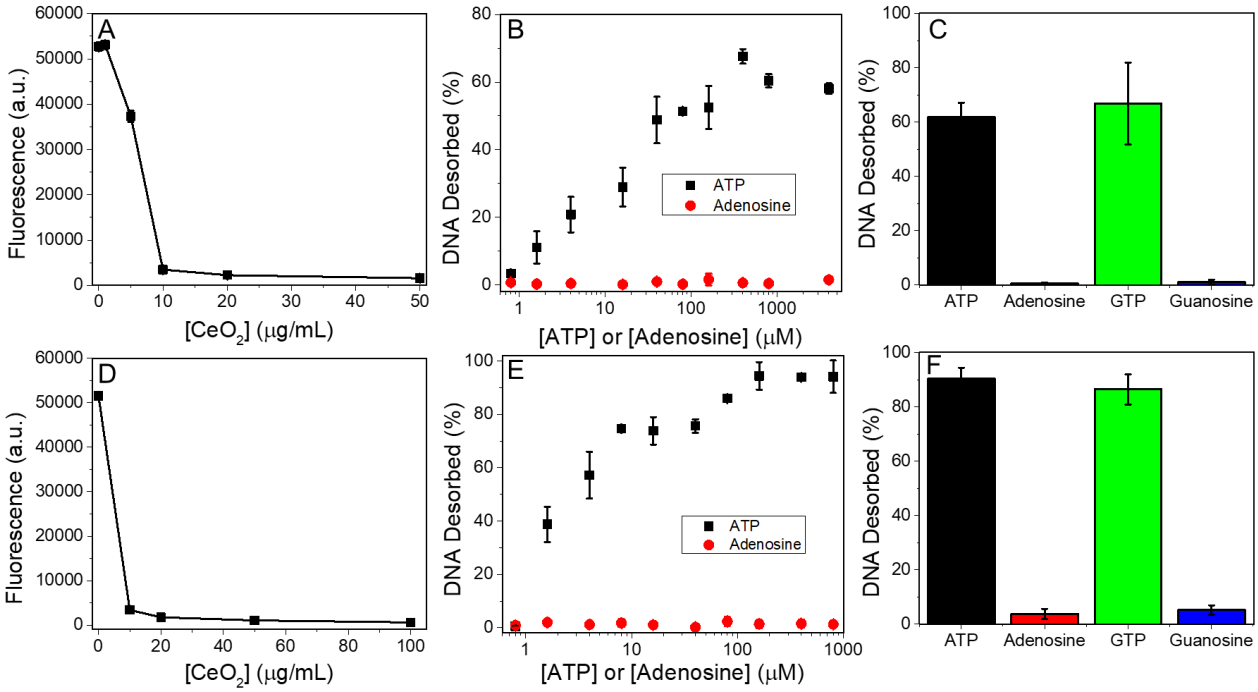

Figure 2.2. Response of DNA-loaded CeO_2 to adenosine and ATP Determination of the optimal CeO_2 nanoparticle concentration to adsorb 50 nM (A) FAM-aptamer and (D) FAM-A_{15} DNA from fluorescence quenching. Based on this data, 10 μg/mL CeO_2 was chosen for both DNA. Addition of various concentrations of ATP and adenosine to CeO_2 (10 μg/mL) adsorbed with 50 nM (B) FAM-aptamer or (D) FAM-A_{15} in buffer A. Response of (C) FAM-aptamer and (F) FAM-A_{15} to various nucleotide-based desorbents. All measurements were performed in buffer A (1 mM $MgCl_2$, 100 mM NaCl and 20 mM HEPES, pH 7.6).

Furthermore, when a non-aptamer sequence was used (FAM-A_{15}, capacity on CeO_2 shown in Figure 2.2D), the trend was the same, with only ATP showing a significant fluorescence increase (Figure 2.2E). In fact, the sensitivity of this response was higher than that of FAM-aptamer. Since

FAM-A_{15} is a shorter strand than FAM-aptamer (27-mer), it is reasonable to expect that the binding with CeO_2 would be weaker (less phosphate groups) resulting in easier displacement by ATP. Similarly, GTP also induced significant desorption of FAM-A_{15} (Figure 2.2F). All these experiments confirmed that the produced signal had little to do with aptamer binding but was due to target/CeO_2 interactions. This is consistent with previous reports of ATP detection using non-aptamer strands adsorbed on CeO_2 nanoparticles.[216] Our data implied that the adsorption of the aptamer on CeO_2 was so tight that aptamer binding could not compete with the adsorption.

We then studied the effect of pH. All our previous experiments were conducted under close to neutral pH (7.6) conditions, where the adenine base (pK_a ~4.2) would be uncharged. We also performed a similar displacement experiment under acidic (pH 4.0) and basic (pH 11.0) conditions (Figure 2.3A). Regardless of pH, the displacement mechanism was dominant as reflected in the higher desorption by ATP compared to adenosine.

Finally, we studied the effect of salt concentration. In general, a high ionic strength favors aptamer/target binding.[214] At the same time, ionic strength may also affect DNA/CeO_2 interactions. The above experiments were performed in the high ionic strength buffer A (20 mM pH 7.6 HEPES, 100 mM NaCl and 2 mM $MgCl_2$). Herein, we tested two additional buffers: buffer B (moderate ionic strength, 20 mM pH 7.6 HEPES and 100 mM NaCl) and buffer C (low ionic strength, only 20 mM pH 7.6 HEPES). In all these samples, ATP desorbed the aptamer, but adenosine did not. When the ionic strength was lowered, ATP effectively displaced all adsorbed aptamers compared to ~60% in the high ionic strength buffer (Figure 2.3B). Since low ionic strength disfavored aptamer binding to target molecules, this again indicated that the desorption was not due to aptamer binding. Interestingly, dynamic light scattering (DLS) showed that CeO_2 was aggregated in buffer C to a similar extent as buffer A (Figure 2.3C), with the average particle size being ~350 nm compared to ~10 nm in water. This was further supported by TEM, which showed that the particle sizes were 5-10 nm (Figure 2.3D), corresponding to the DLS data obtained in water. Therefore, the lower desorption seen at higher ionic strength (buffer A) likely reflected a stronger FAM-aptamer/CeO_2 conjugate, rather than protection from target access due to aggregation.

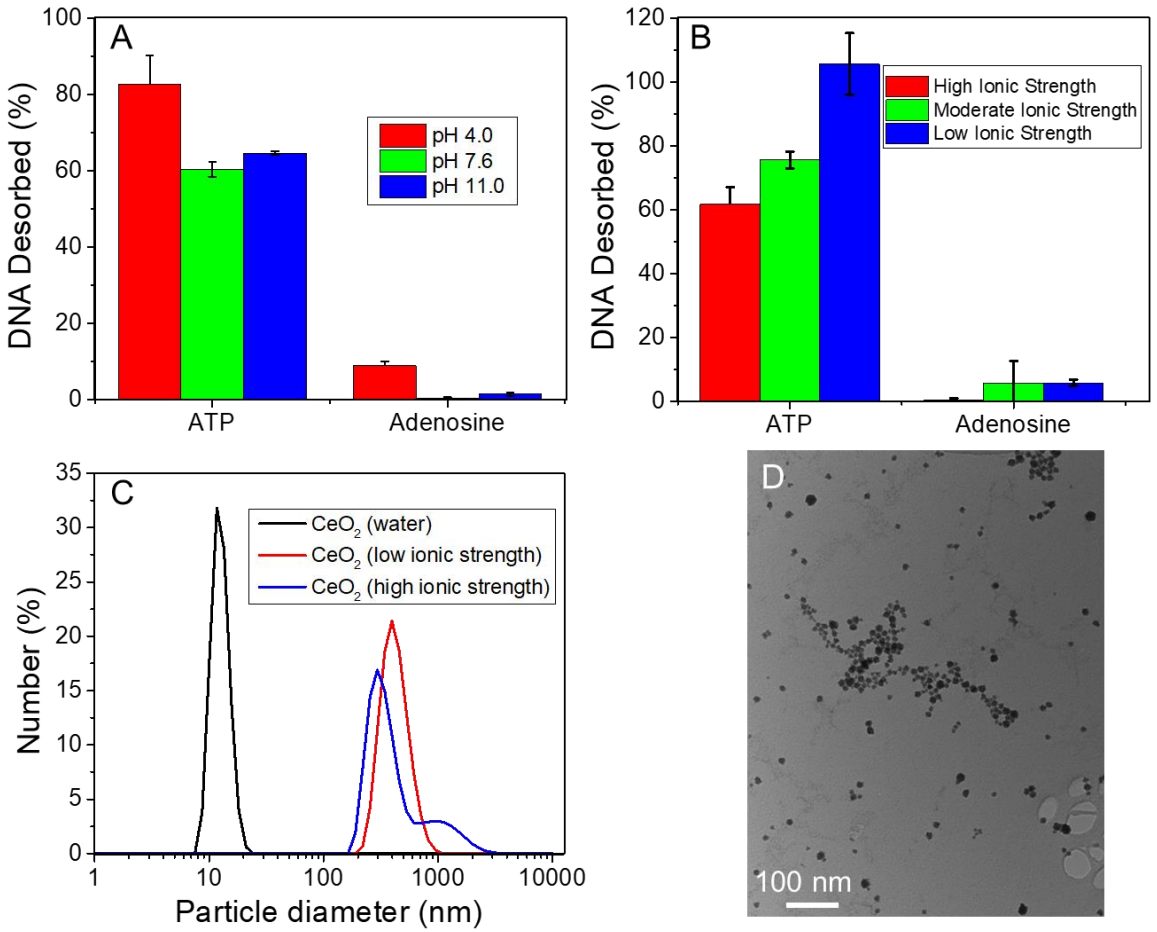

Figure 2.3. Comparison of pH and ionic strength in DNA desorption from CeO_2. (A) Addition of 0.8 mM ATP and adenosine to the FAM-aptamer/CeO_2 at different pH. The NaCl and $MgCl_2$ concentrations were the same as that of buffer A. (B) Addition of ATP and adenosine to the FAM-aptamer/CeO_2 in buffers of high (buffer A), moderate (buffer B), low (buffer C) ionic strength. (C) Dynamic light scattering (DLS) data for the CeO_2 nanoparticles dispersed in water, buffer C (low ionic strength) and buffer A (high ionic strength). (B) TEM image of the CeO_2 nanoparticles.

2.3.2 Detection of complementary DNA

The lack of aptamer binding to adenosine above was attributed to the stronger aptamer adsorption by CeO_2. To increase target binding strength, we used the complementary DNA of the aptamer as the target (cAptamer). In addition, we also added the same aptamer sequence as a competitor (non-labelled, named Aptamer). We tested the effect of ionic strength since a high ionic

strength favors DNA hybridization. Essentially, the non-labelled aptamer strand served to test the displacement mechanism, while the cAptamer was for testing the hybridization mechanism although nonspecific displacement by cAptamer cannot be ruled out either (Figure 2.4A).[161] We found that probe desorption was non-discriminate at the lowest ionic strength (Figure 2.4B), with both 50 nM cAptamer and aptamer strands desorbing 20-30% of the adsorbed DNA. We reason that the desorption under this low salt condition was mainly due to non-specific displacement instead of specific hybridization due to the unfavorable hybridization condition. At high ionic strength (Figure 2.4C), both cAptamer and Aptamer desorbed less than 10% of the adsorbed DNA, with cAptamer desorbing slightly more than the aptamer strand. This difference was higher at moderate ionic strength (almost 2-fold, Figure 2.4D). The overall conclusion is that low ionic strength favors the displacement mechanism, and an intermediate ionic strength may allow selective desorption by the cAptamer, which could be analytically useful for the detection of target DNA. By increasing target binding affinity (using cDNA instead of aptamer targets) and by modulating DNA adsorption affinity (varying ionic strength), selective target DNA detection can be achieved. Since adenosine is just one base, and its binding affinity to the aptamer is much weaker than the 27-base cAptamer, this experiment indicated the importance of the relative binding strength.

Under an appropriate salt condition, the strength of DNA adsorption to CeO_2 was comparable to DNA hybridization. For comparison, when AuNPs were used, even DNA hybridization could not compete with DNA adsorption.[111,217] This is due to the extremely high adsorption affinity of DNA on gold. Therefore, the relative adsorption strength is critical for developing related biosensors. Not all nanomaterials can be used for this sensing purpose.

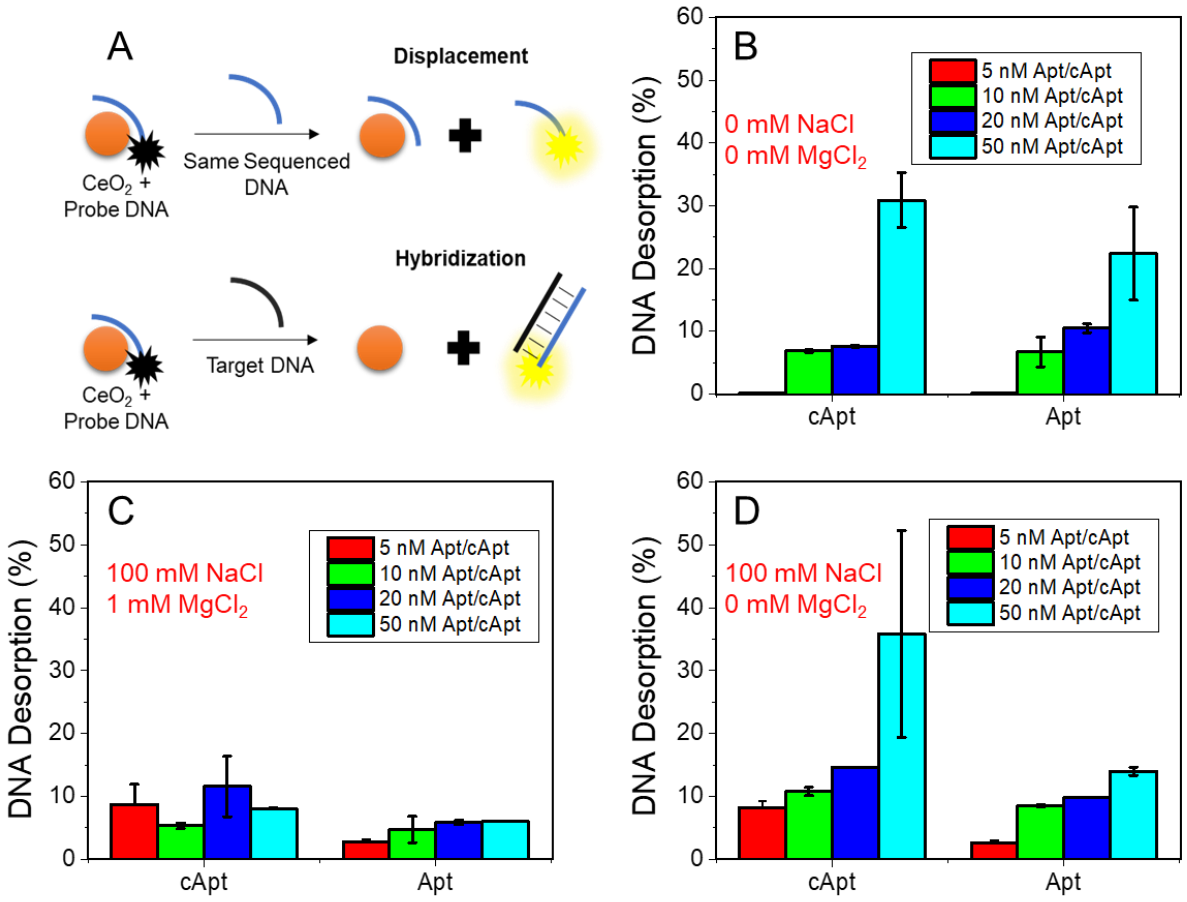

Figure 2.4. DNA desorption from CeO_2 at different ionic strength in response to DNA targets. (A) Schemes showing DNA displacement and hybridization upon the addition of target DNA. Desorption of FAM-Aptamer (10 nM) from CeO_2 (1 μg/mL) induced by various concentrations non-labelled cAptamer (cApt) or aptamer (Apt) in buffers of (B) low, (C) high and (D) moderate ionic strength.

2.3.3 Signal based on the kinetics of aptamer adsorption

In the experiments above, nanomaterials affected adenosine binding to the aptamer. To have a fair comparison, we then pre-mixed adenosine or ATP and the FAM-aptamer before adding CeO_2, and the kinetics of the fluorescence change was monitored (Figure 2.5A). A control was performed with only CeO_2 (no adenosine or ATP). When ATP and FAM-aptamer were pre-incubated, the fluorescence remained high upon addition of CeO_2, indicating a lack of aptamer adsorption. However, when adenosine and FAM-aptamer were pre-incubated, the signal decreased (Figure

2.5A, red trace) in a comparable fashion to that of simply mixing the FAM-aptamer and CeO_2 (Figure 2.5A, blue trace). Therefore, the binding of aptamer and adenosine was outcompeted by the adsorption of the aptamer by CeO_2 to the extent that the aptamer/adenosine binding could not prevent aptamer adsorption at all. On the other hand, the lack of aptamer adsorption in the aptamer/ATP mixture can only be attributed to ATP capping CeO_2 and preventing aptamer adsorption.

To confirm our hypothesis, FAM-A_{15} was substituted for the FAM-aptamer (Figure 2.5B) in the kinetics measurement. A similar trend was observed: only ATP prevented FAM-A_{15} adsorption on CeO_2. Therefore, in this case, aptamer/target binding was irrelevant for signal generation. The weakly adsorbing adenosine cannot affect aptamer adsorption, while the strongly adsorbing ATP inhibits aptamer adsorption by CeO_2, regardless of the order of sample addition.

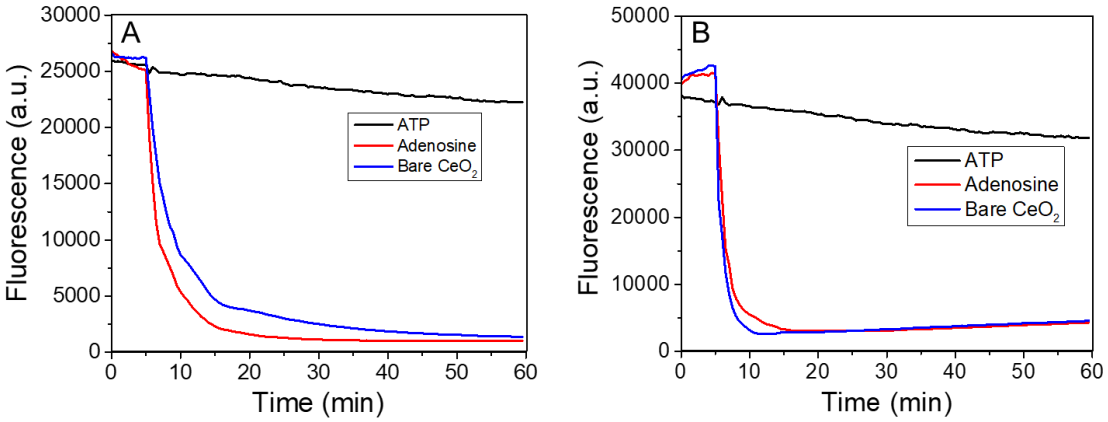

Figure 2.5. Kinetics of adsorption of 50 nM (A) FAM-aptamer and (B) FAM-A_{15} on CeO_2 in the presence of ATP, adenosine or neither.All experiments were conducted in buffer A (1 mM $MgCl_2$, 100 mM NaCl and 20 mM pH 7.6 HEPES) and 10 µg/mL CeO_2. [ATP] = [adenosine] = 0.8 mM.

2.3.4 Detection of adenosine and ATP on other metal oxide nanoparticles

The above study indicated that CeO_2 cannot be used to signal aptamer binding of adenosine or ATP. To understand the generality of this observation, we then tested a few other MONPs including ZnO, NiO, Fe_3O_4 and TiO_2, which have been characterized in our previous publications.[18,133] Under our experimental conditions (buffer A), these particles were more

aggregated (Figure 2.6A) compared to the measured particle size in water. For example, Fe_3O_4 in buffer A formed aggregates of ~400 nm in diameter, despite having individual particles of 30-70 nm under TEM (Figure 2.6B). These MONPs were chosen as they were previously shown to adsorb DNA, quench fluorescence, and some were susceptible to phosphate-induced desorption.[133] The optimal nanoparticle concentration was also individually determined to reach saturated quenching (Figure 2.6C).

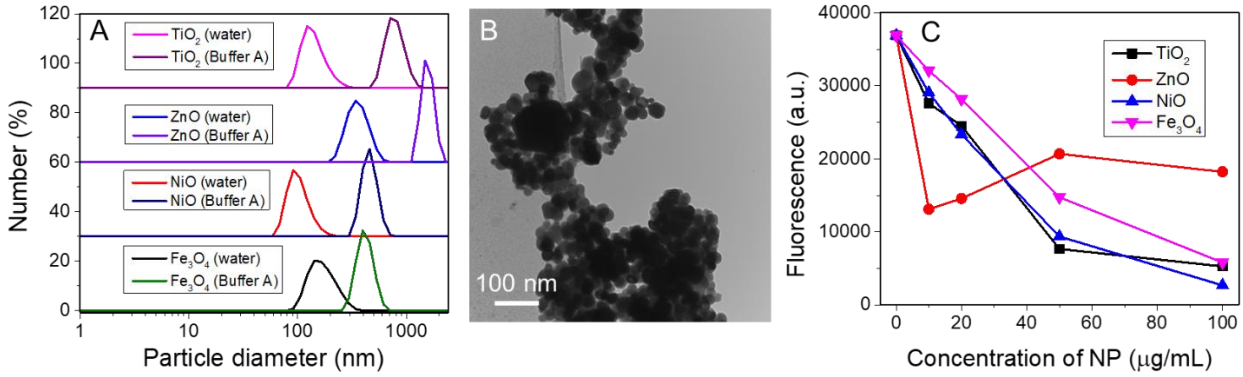

Figure 2.6. Structural characterization and DNA adsorption capacity for various MONPs. (A) Dynamic light scattering (DLS) data for the studied MONPs (apart from CeO_2) in water and buffer A (high ionic strength). (B) TEM image of the Fe_3O_4 nanoparticles showing aggregation. (C) Determination of the optimal MONP concentrations to adsorb 50 nM FAM-aptamer. Based on the fluorescence quenching, the following concentrations were used: 100 μg/mL TiO_2, NiO, and Fe_3O_4. For ZnO, the fluorescence cannot be fully quenched, and thus we chose 50 μg/mL ZnO for future experiments. All measurements performed in buffer A.

We respectively adsorbed the FAM-aptamer on the nanoparticles, followed by the addition of ATP or adenosine to induce aptamer desorption (Figure 2.7A). All the four MONPs showed a similar trend as CeO_2, with ATP desorbing more aptamer compared to adenosine. For adenosine, its response was in the background level, similar to that from the non-target molecule, guanosine. Therefore, the observed aptamer desorption was due to target/MONP interactions rather than target/aptamer binding. These experiments were repeated using FAM-A_{15} as a probe DNA (Figure 2.7B), and a similar profile was seen to FAM-aptamer.

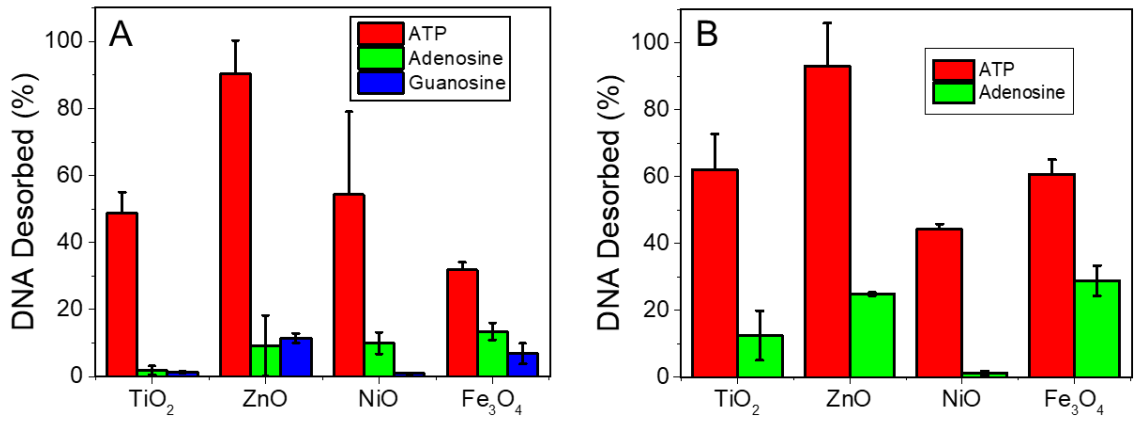

Figure 2.7. The effect of 0.8 mM ATP and adenosine on the desorption of (A) FAM-labeled adenosine aptamer, and (B) FAM-A_{15} DNA from various MONPs. All experiments were conducted in buffer A. TiO_2, NiO and Fe_3O_4 = 100 µg/mL; ZnO = 50 µg/mL.

2.3.5 Detection of adenosine and ATP on GO.

In the previous sections, we studied MONPs where the aptamer interacted primarily through its phosphate backbone with the metal ions on the surface. This was why ATP, with a triphosphate group, could compete with adsorbed DNA. As a further comparison, we also studied graphene oxide (GO), which is a metal free material extensively used for aptamer-based biosensors not just in fluorescence, but also electrochemical detection.[172,218–220] Interactions between DNA and GO are primarily due to a combination of hydrogen bonding (either through the DNA bases or phosphate backbone) and π-π stacking.[114,186,187] Electrostatic forces are repellant in this system as both GO and DNA are negatively charged at neutral pH.

We first determined the concentration of GO to quench 10 nM FAM-aptamer to be 3 µg/mL in buffer D (Figure 2.8A). We then prepared GO/FAM-aptamer conjugates and added various concentrations of ATP or adenosine to induce desorption of the aptamer (Figure 2.8B). In this case, interestingly, adenosine was slightly more effective than ATP, which was the opposite to case with the MONPs. Apart from electrostatic repulsion between ATP and GO, it is known that ATP binds weaker to the adenosine aptamer than adenosine. These two factors likely contributed to the weaker ATP-induced aptamer desorption. We also compared the selectivity to other nucleotides and GTP (Figure 2.8C). Guanosine and GTP induced some desorption of FAM-aptamer from GO.

Since the aptamer does not bind them, desorption was likely due to non-specific displacement. The two pyrimidine nucleosides, thymidine and cytidine, did not induce any aptamer desorption, which can be explained by their weaker affinity to GO than the purines. Therefore, even for adenosine/ATP, it is reasonable to expect that displacement still contributed non-trivially to probe desorption (e.g. similar to guanosine and GTP). However, probe/target binding increased the sensitivity greatly.

The majority of the previous GO/aptamer work used ATP as the target molecule and its selectivity was demonstrated by comparing with other NTPs.[112,218] In our current work, we compared ATP with adenosine to gain more mechanistic insights. The repulsion between ATP and GO can be tuned by varying the ionic strength, which was then studied. Since GO requires a moderate ionic strength to adsorb DNA in the first place, we started with 20 mM pH 7.6 HEPES, 300 mM NaCl and subsequently varied the Mg^{2+} concentration (Figure 2.8D). Adenosine induced more desorption from GO than ATP at most Mg^{2+} concentrations. At the highest concentration of Mg^{2+} (5 mM), desorption by adenosine and ATP became comparable. With sufficient Mg^{2+}, the charge disadvantages (i.e. electrostatic repulsion) of ATP for aptamer binding and GO adsorption were compensated.

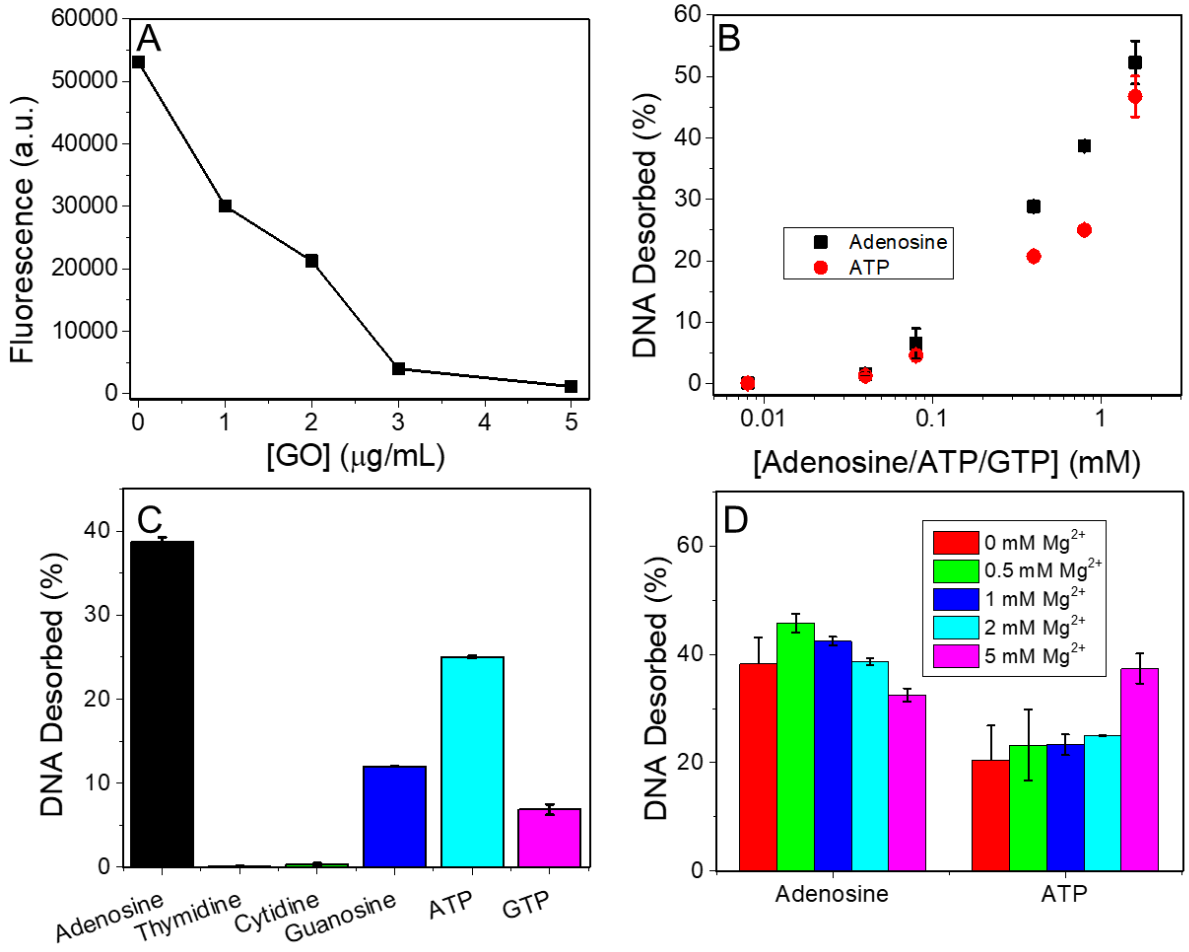

Figure 2.8. Charging DNA-loaded GO with different targets and non-targets. (A) Determination of the optimal GO concentrations to adsorb 10 nM FAM-aptamer. Based on the data, 3 μg/mL GO was used. (B) Response of FAM-aptamer (10 nM) loaded GO (3 μg/mL) to various concentrations of ATP and adenosine in buffer D. (C) Response of the GO/FAM-aptamer conjugate to various targets (0.8 mM) in buffer D. (D) The effect of increasing Mg^{2+} concentration on adenosine- and ATP-induced FAM-aptamer desorption from GO. Apart from Mg^{2+} variation experiments, the other compositions of buffer D were kept the same.

2.4 Discussion

Target molecule induced aptamer desorption from nanomaterials has always been attributed to aptamer binding.[17,221,222] In this work, we tested this hypothesis by comparing two targets of the

same aptamer: adenosine and ATP. We started with some MONPs with a focus on CeO_2. ATP with a triphosphate group has a high affinity to CeO_2,[188] while adenosine does not have such interactions. On the other hand, adenosine has a slightly stronger affinity to the aptamer than ATP.[201] Based on our work, the triphosphate affinity to CeO_2 trumped target (adenosine or ATP) affinity to the aptamer. Although higher ionic strength favors aptamer/target binding, we found that this was not enough to achieve adenosine-induced aptamer desorption. The displacement mechanism was dominant in other tested MONPs as well.

On the flip side, target/surface interactions, when strong and specific enough, can also be used to detect target molecules. We previously used DNA adsorbed Fe_3O_4 nanoparticles to detect arsenate,[159] and DNA adsorbed CeO_2 nanoparticles to detect H_2O_2.[207] In both cases, the DNA was only used to produce fluorescence signal, while target recognition relied on the nanoparticle surfaces.

Based on this study and previous work, we can divide nanomaterials into a few types based on their interaction strength with DNA. First, for very strongly adsorbing materials such as AuNPs, the adsorbed DNA cannot be desorbed even by the cDNA (Figure 2.9A). Desorption may occur by some small molecules or ions such as As (III), Br^- and thiol-containing molecules due to their strong affinity with gold surface and competitive adsorption.

Second, for MONPs, they can generally be used for detecting cDNA.[18] However, none of the tested MONPs allowed specific detection of adenosine (Figure 2.9B), and this can be attributed to the weaker interaction between adenosine and the aptamer compared to DNA binding to its cDNA. At the same time, since cDNA can also be adsorbed on metal oxides, displacement effects may also contribute. In this study, we chose adenosine/ATP as targets since they have drastically different affinities to MONPs, yet they both can bind to the same aptamer. Its K_d is typical for small molecule binding aptamers. The length of this aptamer (27 nucleotides) is on the short side, while many other small molecule binding aptamers are around 30-50 nucleotides. Based on this analysis, we do not believe that other adsorbed aptamers can be desorbed from MONPs solely due to aptamer binding to their target molecules. Since each target molecule is different, we cannot discuss their adsorption on MONPs in general. In addition, we cannot rule out that aptamers with very strong affinities to the target (K_d << 1 μM, comparable to DNA hybridization) may be

desorbed from MONPs through target/aptamer binding. To understand the mechanism of aptamer desorption, it is important to use non-aptamer sequences as controls to validate the observed signal.

Finally, nanomaterials such as GO have a moderate affinity for DNA (Figure 2.9C). For GO, the range of adsorption affinity is broad due to its surface heterogeneity with the highly oxidized regions being lower affinity and the pristine graphene regions being high affinity.[150,156] In the low affinity regions, aptamer binding can be comparable with DNA adsorption. If aptamer targets can be detected, it is not surprising that cDNA can also be detected. Detection of cDNA using GO has been extensively demonstrated, although target-induced probe displacement also played key roles in the observed signals.[161]

Since there are so many different types of materials that have been used for similar sensing purposes, it is impossible to discuss each one individually. The three types shown in Figure 2.9 can be interpreted as representative examples for very strong, strong and moderate interactions with DNA. To ensure aptamer-based detection, aptamer binding needs to be the dominating mechanism of signal production. Nonspecific displacement needs to be avoided, which can be measured by using non-aptamer probes as controls.

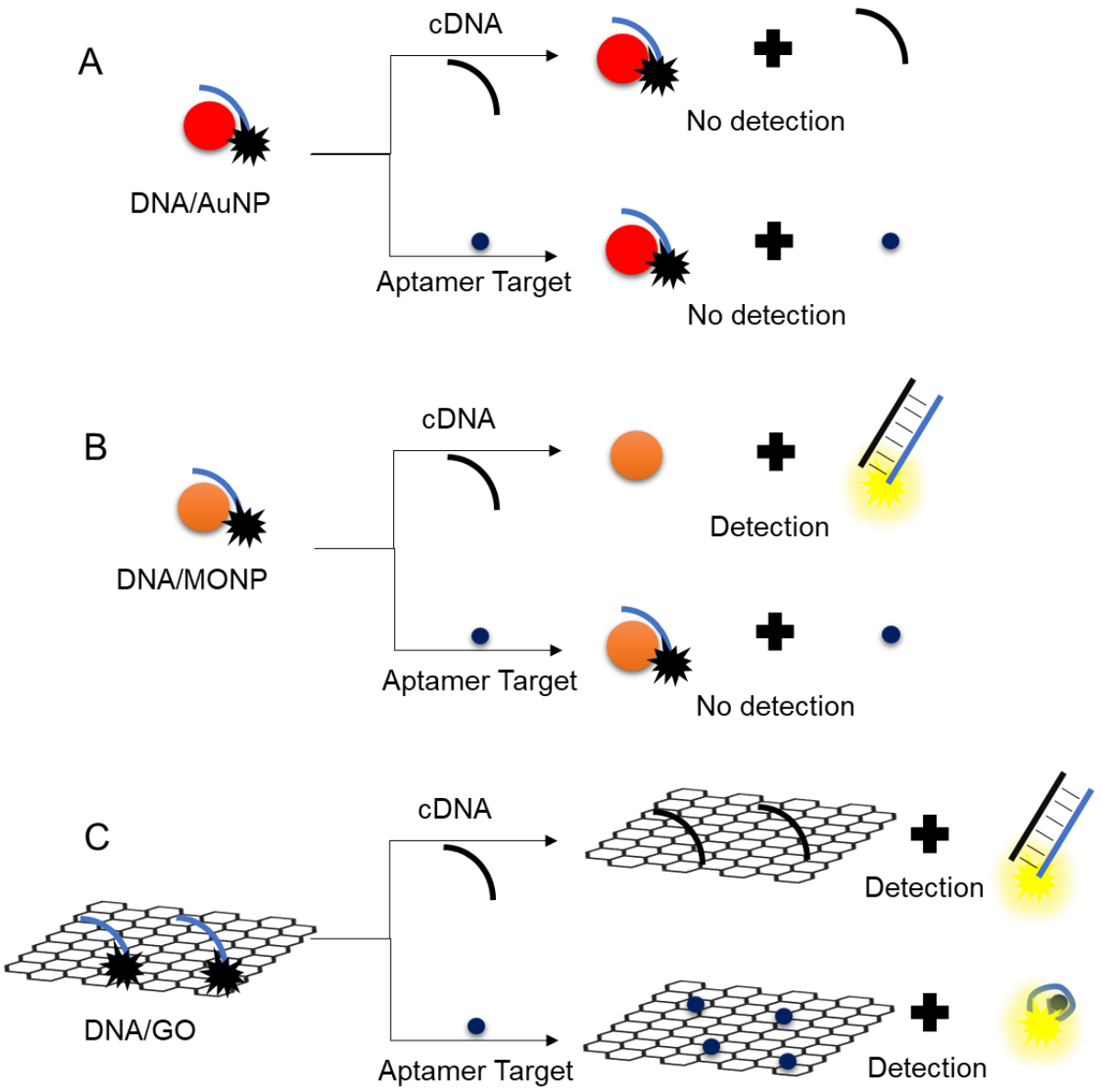

Figure 2.9. Classifying different nanomaterial/DNA conjugates in terms of DNA adsorption strength. (A) DNA adsorbs on AuNPs very strongly, and neither cDNA nor aptamer targets can induce desorption. (B) MONPs represent a relatively strong adsorption strength, where cDNA can induce desorption, but aptamer targets cannot. (C) Both cDNA and aptamer targets can desorb probe DNA from GO. These cartoons do not consider desorption of the probes due to competition from target molecules or cDNA (e.g. nonspecific displacement).

2.5 Conclusions

In this work, we sought to investigate the adsorption of target molecules and its effect on aptamer-based biosensors using the adenosine/ATP aptamer as a model system. We first focused on CeO_2, where we found that displacement dominated over target/aptamer interactions. Only ATP was able to desorb the aptamer from CeO_2 due to competitive adsorption, while adenosine resulted in no aptamer desorption at all. This was also observed with four other MONPs. Desorption of the same aptamer probe from GO, on the other hand, occurred with both adenosine and ATP. Adenosine was slightly more effective under most conditions. Since adenosine, compared to ATP, has stronger interactions with GO, target adsorption also contributed to the detection of adenosine in this case. In the end, we used the binding affinities cDNA and typical aptamer targets as two thresholds and divided materials into three types. Only when the aptamer binding to its target is stronger than the adsorption of the aptamer, can specific aptamer-based detection be achieved. Otherwise, the signal might be mainly from nonspecific desorption. This study indicates that careful control experiments are needed to ensure the signal production mechanism of this type of biosensors.

Chapter 3 - Fluorescein-Stabilized i-motif DNA and Its Unfolding Leading to Stronger Adsorption Affinity

The results presented in this Chapter have been published as:

Anand Lopez, Biwu Liu, Zhicheng Huang, Fang Zhang, and Juewen Liu. "Fluorescein-Stabilized i-Motif DNA and Its Unfolding Leading to a Stronger Adsorption Affinity". *Langmuir* **2019**, 35, 36, 11932–11939.

3.1 Introduction

Interfacing DNA with nanomaterials has attracted significant interest in recent years with applications in biosensing,[196,223–227] gene delivery,[228–230] drug delivery,[196,231] and directed assembly of nanomaterials.[232,233] To achieve the full potential of these applications, it is critical to understand and control DNA adsorption to produce high quality DNA/nano conjugates. In many systems, a fluorescently labeled DNA oligonucleotide is adsorbed, and its fluorescence is quenched by the surface. Stimuli-responsive desorption of the DNA is then accompanied with fluorescence enhancement, which is commonly used for biosensor development.[18,192,234,235]

DNA interacts with different nanomaterials differently.[236] For example, DNA uses its phosphate backbone to adsorb onto many metal oxides.[18,237] For carbon-based nanomaterials, attraction is due to the formation of hydrogen bonds with the DNA bases, as well as π-π stacking.[160,200,238] Finally, DNA adsorbs quite strongly on gold nanoparticles (AuNPs) through coordination of the nucleobases.[23]

The interaction strength typically varies with DNA sequence. For AuNPs, poly-deoxyadenosine (poly-A) DNA has the strongest affinity,[239–242] whereas for metal oxides, the sequence-dependency is weaker.[23,133,243] Interestingly, for carbon-based materials, coordination nanoparticles,[244] polydopamine nanoparticles,[198] and calcium phosphate,[245] poly-deoxycytidine (poly-C) DNA has the strongest affinity.[186,187] As an example, we adsorbed various dye-labelled 15-mer DNA (A_{15}, C_{15}, T_{15}, G_{15}) on graphene oxide (GO), and C_{15} had the strongest resistance to desorption.[186]

C-rich DNA can fold into a structure known as an "i-motif" composed of C-C^+ base pairs (Figure 3.1).[38,246] However, as the pK_a of the N_3 in cytosine is 4.2,[247,248] i-motif DNA should be

largely unfolded at neutral pH. Some solution conditions (e.g. molecular crowding or the presence of Ag^+) have been reported to stabilize the i-motif at neutral pH.[41,249–252] A few nanosized carbon materials were also able to achieve this stabilization effect, including carbon nanotubes,[253,254] fullerene,[255] and graphene quantum dots.[186,256] Intuitively, a folded DNA should adsorb less strongly on a surface. Therefore, even if an i-motif is formed, it still cannot explain the tighter adsorption affinity. The pH-responsiveness of i-motif DNA has often been used for pH sensing, and its nanoconjugates can facilitate cellular uptake and signaling.[257] In addition, the high stability adsorption of C-rich DNA is important for bioconjugation.[186] Therefore, understanding adsorption of such C-rich DNA is critical for biosensor development.

In most of our experiments, a carboxyfluorescein (FAM) is labeled on the 5′-end of the DNA sequence. An interesting question is whether this dye affects the folding of poly-C DNA? If so, how does this influence the stability of adsorption? To answer these questions, we herein systematically studied FAM-labeled DNAs. Quite surprisingly, we found that the FAM label played a critical role in stabilizing the i-motif structure. After unfolding DNA (by heating), adsorption of poly-C DNA became even stronger on GO.

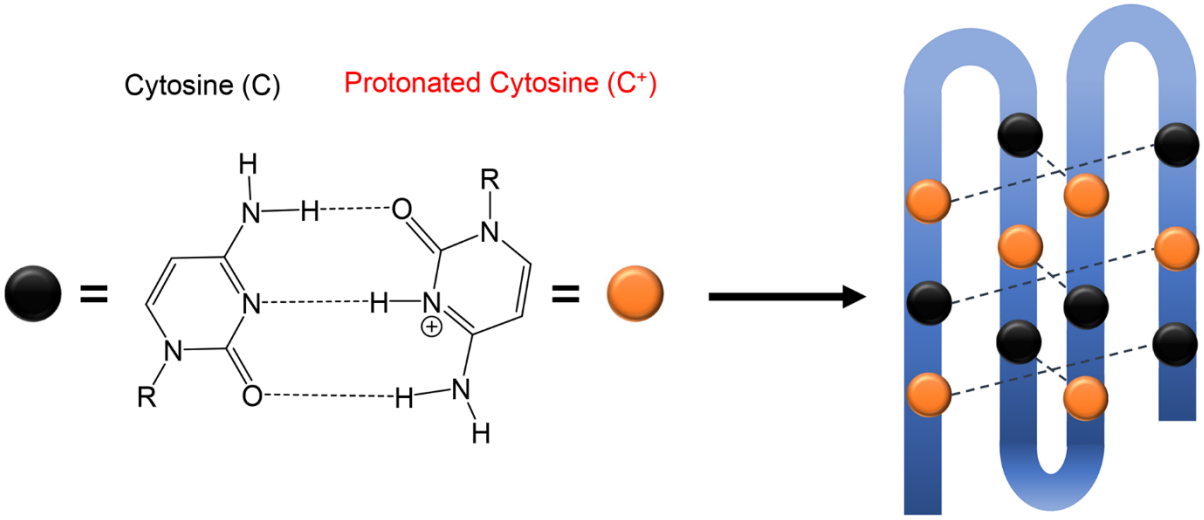

Figure 3.1. A general structure and constituents of an i-motif DNA. Base pairing occurs between C and C^+ nucleobases resulting in the formation of the folded structure.

3.2 Materials and Methods

All of the DNA sequences (Table 3.1) were purchased from Integrated DNA Technologies (Coralville, IA, USA). 4-(2-hydroxyethyl)-1-piperazineethanesulfonic acid (HEPES), sodium phosphate monobasic, sodium acetate, sodium citrate, and sodium bicarbonate were purchased from VWR Canada. 2-(N-morpholino) ethanesulfonic acid (MES) and sodium chloride (NaCl) were purchased from Bio Basic Canada. Fluorescein, and acetic acid were purchased from Sigma-Aldrich. Graphene oxide was purchased from ACS Materials LLC. The as-purchased DNA samples were received in a dried powder form. This was dispersed in water to a concentration of 0.1 mM, and a portion of it was further diluted to a stock concentration 1 µM. Both solutions were stored in a freezer (-20°C) before use.

Table 3.1. List of the DNA sequences and modifications used in Chapter 3. FAM: carboxyfluorescein.

DNA names	Sequence (5′→ 3′)
FAM-C_5	FAM-CCC CC
FAM-C_{10}	FAM-CCC CCC CCC C
FAM-C_{15}	FAM-CCC CCC CCC CCC CCC
FAM-C_{20}	FAM-CCC CCC CCC CCC CCC CCC CC
C_{15}	CCC CCC CCC CCC CCC
T_{15}	TTT TTT TTT TTT TTT
FAM-T_{15}	FAM-TTT TTT TTT TTT TTT
FAM-T_5	FAM-TTT TT
A_{15}	AAA AAA AAA AAA AAA
FAM-A_{15}	FAM-AAA AAA AAA AAA AAA
IM	CCC TAA CCC TAA CCC TAA CCC T
FAM-IM	FAM-CCC TAA CCC TAA CCC TAA CCC T

Fluorescence measurements. Fluorescence was measured as a function of pH using a Tecan (Spark) spectrometer. The dye-labeled DNA or free fluorescein was dispersed in various buffers (10 mM) at a final concentration of 20 nM. These buffers were phosphate (pH 3.4), acetate (pH

4.0), citrate (pH 5.0), MES (pH 6.0), HEPES (pH 7.6), Tris (pH 8.5), carbonate (pH 9.5), and phosphate (pH 11.2). The excitation and emission wavelengths were 485 nm and 535 nm respectively for FAM. For the cy3 experiment, the excitation and emission wavelengths were 532 nm and 577 nm, respectively and the measurements were performed in 10 mM HEPES buffer (pH 7.6). These experiments were repeated using heated DNA (95^{o}C for 10 min and cool to room temperature).

Melting analysis. All DNA studied were dispersed in 10 mM HEPES buffer (pH 7.6) at a concentration of 1 µM. 50 µL of this solution was transferred to a microtube and placed in a CFX-90 Real Time System coupled with a C-1000 thermal cycler (BioRad). The samples were then heated at a rate of 1°C/min from 4°C to 95°C, measuring fluorescence after incubating at each temperature for 60 sec.

Circular dichroism. CD measurements were conducted with a Jasco J-715 spectrophotometer. DNA samples were prepared in 25 mM buffer solution (citrate for pH 5; HEPES for pH 7.6). For the heated samples, heating was performed as described above. The final concentration of DNA was 10 µM. Each sample was measured in a continuous scanning mode (from 320 to 220 nm) for 5 cycles.

Fluorescence lifetime. FAM-C_{15} and FAM-T_{15} were dispersed in 10 mM HEPES buffer (pH 7.6) at a concentration of 2.5 µM and 500 nM respectively. FAM-C_{15} was significantly quenched in its folded state and thus was used at a high concentration. 200 µL of each sample was transferred to a cuvette before measuring the fluorescence lifetime using a FluoroMax-4 spectrofluorometer (Horiba Scientific). The excitation was achieved using a 450 nm laser, detecting the emission at 505 nm and a band-pass of 10 nm (FAM-T_{15}) or 5 nm (FAM-C_{15}) and a detector voltage of 700 V. Each sample was compared before and after heating (95°C for 10 min).

FAM C_{15} adsorption on GO. To determine the capacity of GO for FAM-C_{15} DNA, different concentrations of GO were titrated against 20 nM FAM C_{15} DNA in 10 mM HEPES buffer (pH 7.6) containing 300 mM NaCl. The samples were incubated for 1 h, centrifuged and the fluorescence of the supernatant was measured on the Tecan plate reader. This was compared with a calibration curve to determine the concentration of GO necessary to adsorb all DNA. This was performed for both heated and unheated C_{15}.

DNA desorption from GO. FAM-C_{15}, FAM-T_{15}, and FAM A_{15} (20 nM each) were respectively adsorbed on 10 μg/mL GO in 10 mM HEPES buffer (pH 7.6) containing 300 mM NaCl. The samples were incubated for 1 h before transferring to a 96 well plate. The fluorescence was then measured every 30 sec (excitation: 485 nm; emission: 535 nm). After 5 min, desorption was induced using 2 μM non-labelled DNA.

3.3 Results and Discussion

3.3.1 FAM-labeled C_{15} DNA has abnormally low fluorescence at neutral pH

Since the stability of i-motif is strongly pH-dependent and folded and unfold DNA might quench fluorescence to different extents, we wondered if we could use fluorescence to follow DNA folding/unfolding. FAM-labeled DNA is often used due to its cost-effectiveness and high fluorescence yield, but the fluorescence intensity of FAM is also strongly affected by pH. Therefore, we designed careful controls to separate fluorescence change due to pH and due to DNA folding. We measured the fluorescence of the four types of 15-mer DNA homopolymers as a function of pH and a control was performed with the free fluorescein (Figure 3.2A). The general trend is that the higher the pH, the higher the fluorescence. For the free fluorescein dye, we can fit an apparent pK_a of 6.8, which is consistent with its reported value of 6.7.[258] While most of the fluorescence changes can be attributed to the effect of pH on FAM, a careful examination still reveals interesting differences.

The fluorescence intensity of FAM-C_{15} was the lowest at pH 7.6 among the four types of 15-mer DNA homopolymers. Compared to that at pH 9.5, the FAM-C_{15} fluorescence at pH 7.6 was only 6.0%, while FAM-labeled A_{15}, T_{15} and G_{15} reached 31%, 30% and 23% of that at pH 9.5, respectively (Figure 3.2B). The free fluorescein reached ~70%. Therefore, all the DNAs quenched the FAM emission, and the extent of quenching was the highest for FAM-C_{15} at pH 7.6. Poly-G DNA is known to be a strong quencher,[259] but at pH 7.6, the fluorescence intensity of FAM-G_{15} was even higher than that of FAM-C_{15}. Quenching of fluorescence by other bases has also been reported recently.[260] The mechanism of such quenching was attributed to photo-induced electron transfer, with guanine being the best quencher in the studied conditions. However, previous studies only varied the bases next to FAM, while secondary structures of DNA and their effects on fluorescence quenching were not considered. In our case, the FAM label in the C_{15} DNA must

experience a strongly quenching local environment either by static or dynamic mechanisms. This strong quenching cannot be explained by the typical adjacent base effects, and likely relates to the secondary structure of FAM-C_{15}.

We also studied a FAM-labeled i-motif forming DNA (named FAM-IM) and compared its fluorescence trend with FAM-C_{15} (Figure 3.2C). This IM was from the human telomeric sequence known to form an i-motif in acidic conditions.[39] The trend for both sequences is quite similar, with a large jump in fluorescence intensity after pH 7.6. This provided some evidence that the folding of the DNA (likely an i-motif) was responsible for the strongly quenched fluorescence at neutral pH for FAM-C_{15}. Note that the change of fluorescence between pH 7.6 and 9.5 was due to two factors. One was from the pH-dependent fluorescence intensity of FAM, and this factor produces only about 50% fluorescence increase (the last bar in Figure 3.2B). The rest was due to disrupted FAM/nucleobase interactions. The large increase of these i-motif DNAs indicated strong FAM/DNA interactions and the strong quenching ability of the i-motif structures.

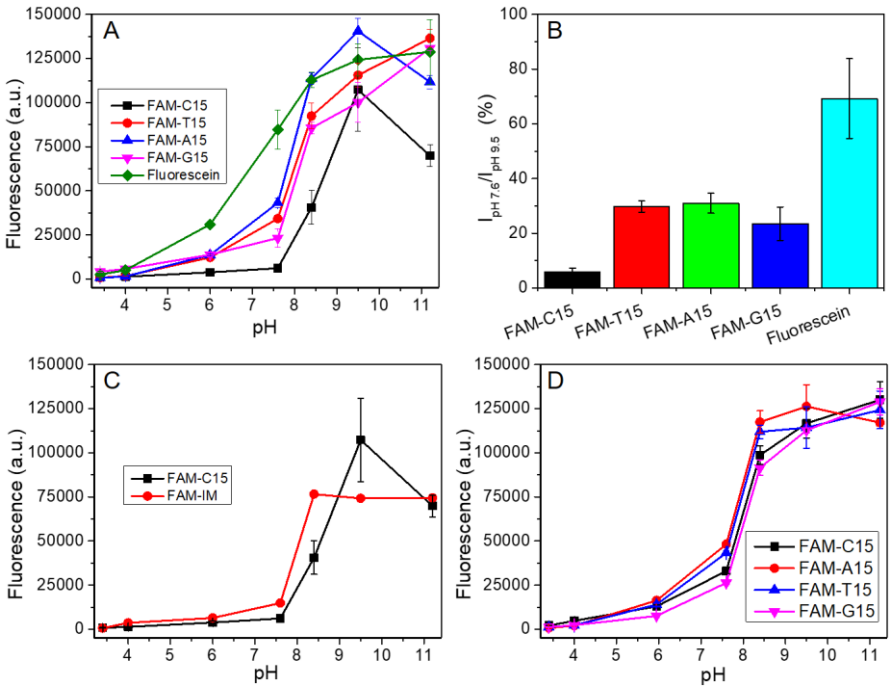

Figure 3.2. Fluorescence of different 15-mer DNA at different pH before and after heating. (A) Fluorescence at 535 nm of four FAM-labeled 15-mer DNA, as well as free fluorescein at different pH. (B) Ratio of the fluorescence intensity at pH 7.6 over that at pH 9.5 for the samples in (A). (C)

Comparing the fluorescence of FAM-labeled C_{15} to FAM-labeled i-motif (IM) DNA at different pH. (D) Fluorescence of the four DNAs after heating and cooling to room temperature as a function of pH. All measurements were performed using 10 mM buffer with a DNA final concentration of 20 nM.

We then heated all the DNA samples to 95°C for 10 min followed by cooling them to room temperature. At this moment, we performed the pH-dependent measurement again (Figure 3.2D), and the fluorescence of FAM-C_{15} at pH 7.6 became much higher and similar to the other DNAs. Therefore, some structure in the FAM-C_{15} might be disrupted by heating and such a structure unfolding was irreversible.

To further understand this, we also studied the effect of pH on the shorter FAM-C_5 and FAM-T_5 (Figure 3.3A). In both cases, the increase in fluorescence was more gradual between pH 7.6 and 9.5. Therefore, shorter FAM-C_5 was unable to fold into the quenching structure, and thus a minimal length is required. We also changed the fluorophore to Cy3 (Figure 3.3B). In this case, no significant change in the fluorescence intensity was observed upon heating. Therefore, this strong quenching by C_{15} is not general but unique to FAM. FAM is a negatively charged fluorophore, while Cy3 is cationic. They also have quite different structures, which can influence their interactions with DNA.

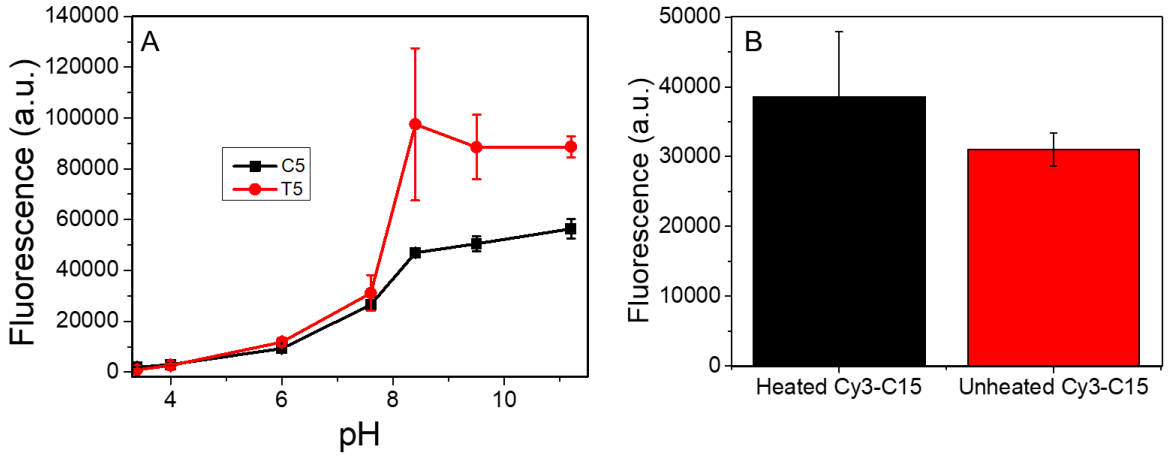

Figure 3.3. The effect of pH and heating on other DNA strands. (A) A comparison of FAM-C_5 and FAM-T_5 fluorescence with pH. All measurements were performed with 10 mM of the desired

buffer with a final DNA concentration of 20 nM. (B) Fluorescence of 20 nM Cy3-C_{15} before and after heating in 10 mM pH 7.6.

3.3.2 Irreversible melting of FAM-C_{15} DNA

Since the fluorescence of FAM-C_{15} significantly increased upon heating (e.g. comparing Figure 3.2A and 3.2D), we can follow its unfolding (or melting) by measuring temperature-dependent fluorescence changes. When FAM-C_{15} was heated gradually at pH 7.6, an interesting melting transition was observed with a melting temperature (T_m) of 69°C (Figure 3.4A and 3.4B for its first derivatives). This T_m value was independent of DNA concentration, indicating that melting occurred for an intramolecular conformational change. We then cooled the samples back down to 4°C, and then raised the temperature again, but the fluorescence did not increase this time (Figure 3.4C, 3.4D). Therefore, melting occurred only for the first cycle and simple cooling could not restore the original DNA structure responsible for the quenched fluorescence. For comparison, the melting of FAM-IM with a sequence of $(C_3TAA)_3C_3T$ was also measured. It also showed a melting transition in the first cycle but not the second one (Figure 3.4E, 3.4F). Therefore, its also formed a structure when freshly prepared, but the structure can be irreversibly disrupted by heating at neutral pH.

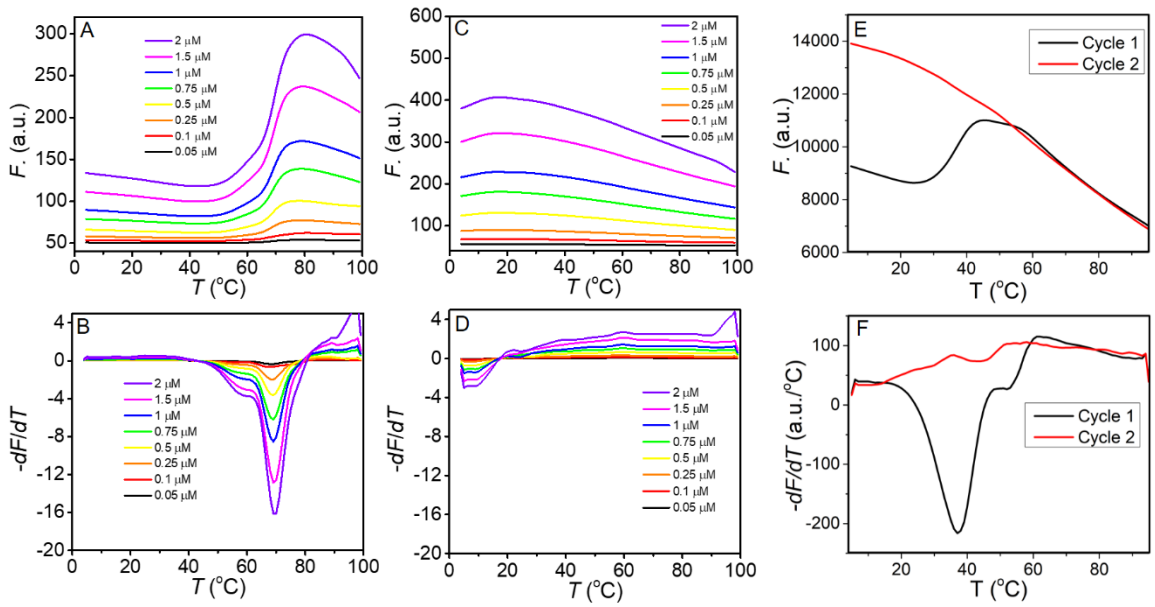

Figure 3.4. Melting curves of FAM-C_{15}. (A) Fluorescence intensity and (B) its first derivative of freshly prepared FAM-C_{15} at different concentrations at different temperatures. (C) Fluorescence and (D) derivative of the fluorescence of FAM-C_{15} for the second melting cycle. (E) Fluorescence and (F) derivative of fluorescence as a function of temperature over two cycles for the FAM-IM DNA. All measurements performed in 10 mM HEPES pH 7.6. The final concentration of DNA was 1 μM.

We also performed melting analysis of longer and shorter FAM-labeled poly-C DNA, and FAM-A_{15}, T_{15} and G_{15} (Figure 3.5A, 3.5B). Apart from FAM-C_{20}, all the other sequences did not exhibit a noticeable melting transition. Quite likely, C_{20} also formed an i-motif structure like C15. Formation of i-motif for poly-C DNA has a requirement of 4n-1 (where n=4,5,6,…).[37,261] Therefore, with n=4, C_{15} would be a perfect "sweet-spot" in this sequence space.

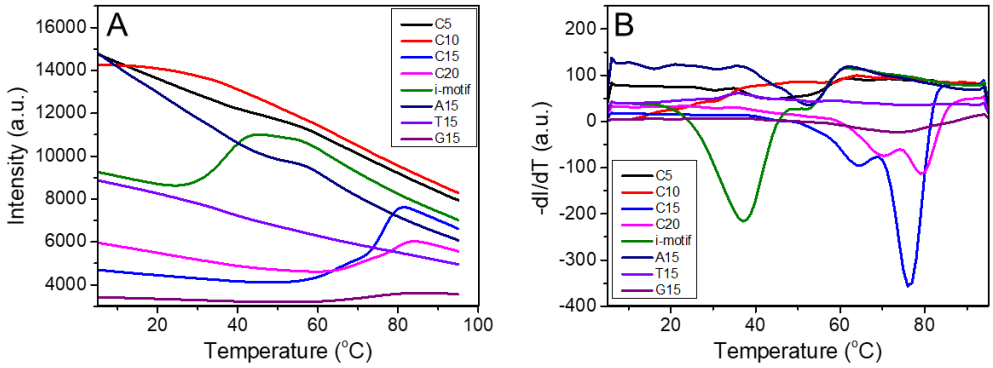

Figure 3.5. (A) Fluorescence and (B) derivative of fluorescence as a function of temperature for various FAM-labelled DNA. All measurements were performed in 10 mM HEPES (pH 7.6) and a final DNA concentration of 1 µM.

3.3.3 CD spectroscopy showing FAM-stabilized i-motif

To further understand the nature of these transitions, we performed CD spectroscopy for both the IM (Figure 3.6A) and the C_{15} (Figure 3.6B) DNA. In this case, the DNAs were non-labeled. At pH 5, the characteristics of C_{15} and IM were both consistent with an i-motif (e.g. positive peak at 290 nm and negative peak at 255 nm),[261] while at pH 7.6, the i-motif features disappeared. Interestingly, heating had almost no effect on either the C_{15} or the IM DNA. After heating and cooling, both showed the same folding as the unheated. Therefore, the effect of heating was reversible for the non-labeled DNAs, and they returned to the original conformation when cooled to room temperature. For these non-labeled DNAs, their conformations were mainly governed by pH as expected for typical i-motifs. This seemed to conflict with the earlier melting analysis of both DNA sequences (e.g. irreversible by heating). Therefore, we suspected that the FAM label might play a critical role.

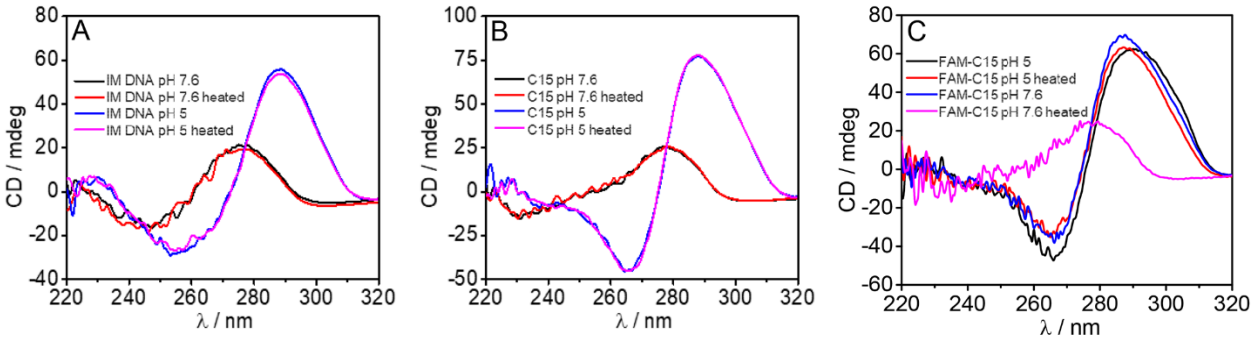

Figure 3.6. CD spectra of (A) non-labelled IM, (B) non-labelled C_{15}, and (C) FAM-labelled C_{15} DNA. In all cases, the spectra were obtained at both pH 5 and pH 7.6 before and after heating (final measurements all at room temperature). The buffer was 25 mM citrate (pH 5) or HEPES (pH 7.6) and the final concentration of DNA was 10 μM.

We then performed the same analysis with the FAM-labeled C_{15} (Figure 3.6C). Indeed, this set of spectra showed a large difference. Before heating and cooling at pH 7.6, the obtained spectrum was consistent with that of an i-motif. After heating and cooling, the features reverted to a random coil, which was consistent with the melting data above. Normally, the i-motif is formed only at slightly acidic pH since a fraction of the cytosine base needs to be protonated (pK_a ~ 4.2). However, with a FAM-label, it may fold into the i-motif even at neutral pH, but the i-motif is disrupted at strong basic pH. This folded structure can also be irreversibly disrupted by heating.

3.3.4 Fluorescence lifetime indicating static fluorescence quenching

Based on the above results, it appears that the FAM fluorophore might facilitate a stable complex. To further understand this, we used fluorescence lifetime to characterize the dynamics of the fluorophore in the initial state and after heating (Figure 3.7A, 3.7B). The average lifetimes were 2.73 ns (no heating) and 2.43 ns (heated) for FAM-C_{15}; and 2.58 ns (no heat) and 2.69 ns (heat) for FAM-T_{15}. Note that the steady-state fluorescence quenching was 94% (FAM-C_{15}) and 70% (FAM T_{15}), comparing the fluorescence at pH 7.6 to that at pH 9.5. Therefore, the lifetime can be considered to be unchanged with regards to the large amount of steady state quenching. The fact that these lifetimes were very close suggested that the mechanism of quenching was static in nature. For example, stacking of the bases with FAM may result in a nonfluorescent species.

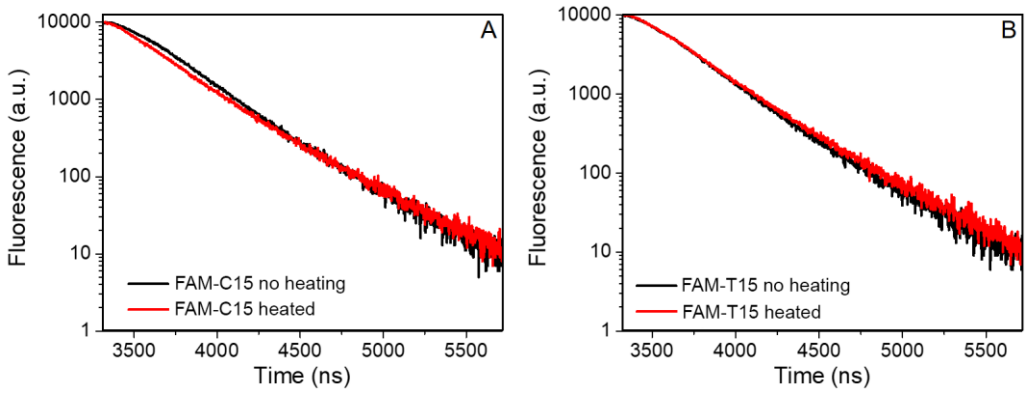

Figure 3.7. Fluorescence lifetime measurements of (A) FAM-C_{15} and (B) FAM-T_{15} before and after heating. All measurements performed in 10 mM pH 7.6 HEPES buffer at room temperature. The final concentration of DNA was 2.5 µM and 500 nM for FAM-C_{15} and FAM-T_{15} respectively.

3.3.5 Heated poly-C adsorbs stronger on GO.

We started this study because we previously observed that poly-C DNA adsorbed on many surfaces more strongly than other DNA homopolymers.[186] If a FAM-labeled poly-C DNA can initially form an i-motif structure, we suspect that the adsorption should be less effective than an open stretched DNA. To test this, we used graphene oxide (GO) as a model surface. We first measured adsorption of both heated and unheated FAM-C_{15} at various concentrations of GO by simply following fluorescence quenching (Figure 3.8A). For 20 nM FAM-C_{15}, 10 µg/mL GO was enough for full adsorption, regardless of the state of the DNA (heated or unheated). With this in mind, we then added excess C_{15} to displace FAM-C_{15} from GO to probe the strength of adsorption (Figure 3.8B). Since folded C_{15} quenched the fluorescence of FAM, in order to calculate the percentage of desorption, two different calibration curves (Figure 3.8C) would need to be generated. That is, one for the folded and another for the unfolded state. It was initially assumed that the desorbed species was in the same state as before (e.g. adsorbing folded DNA on GO will result in folded DNA being desorbed). However, using the calibration curve for unheated DNA, it was calculated that 300% of the adsorbed DNA was desorbed in the case of unheated DNA.

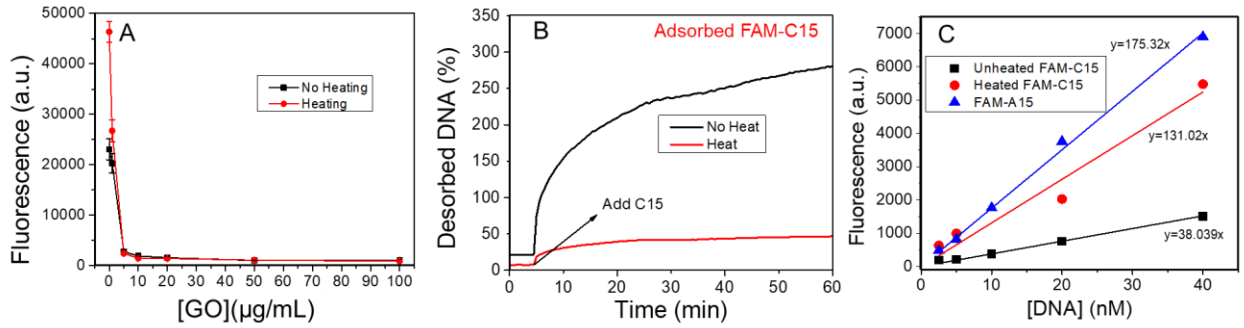

Figure 3.8. Impact of heating and not heating on DNA adsorption and desorption from GO. (A) Adsorption of heated and unheated FAM-C_{15} on graphene oxide. (B) Desorption profiles of FAM-C15 adsorbed on GO after the addition of 2 μM C_{15} before considering the state of the desorbed DNA. (C) Calibration curve for the various free FAM-DNA used. In all cases (A-C), the buffer was 10 mM pH 7.6 HEPES containing 300 mM NaCl.

We then repeated the same desorption experiments and collected the desorbed DNA. The desorbed DNA was heated and cooled before measuring the fluorescence (Figure 3.9A). After heating, a 33% increase was observed in the fluorescence for the unheated DNA compared to no change for the heated DNA. This confirmed that a significant percentage (~67%) of the folded DNA unfolded upon adsorption to or desorption from GO. After correcting for this, a more accurate representation of FAM-C_{15} desorbed can be seen in Figure 3.9B. Therefore, we hypothesized that there was a change in the conformation either during the adsorption or desorption process that unfolded the C_{15} DNA, resulting in a higher fluorescence intensity. We believe that when adsorbed, FAM-C_{15} likely still in the folded state. Otherwise, if fully unfolded, the desorption should be similar to that of the heated FAM-C_{15}. This argument does not consider partial unfolding, which may result in an intermediate adsorption strength. During displacement by other DNA, some of folded FAM-C_{15} could be unfolded. This is illustrated in Figure 3.9D.

To obtain the plot shown in Figure 3.9B, a correction factor was applied to the desorbed FAM-C_{15} based on the fluorescence after heating. More specifically, the desorbed FAM-C_{15} was heated and the fluorescence was compared to the calibration curve of heated FAM-C_{15} to find the total concentration of desorbed DNA. This concentration was then matched with the original

fluorescence intensity (before heating) to get a new calibration curve slope. This slope was found to be 105.69 a.u./nM, which was between that of unheated and heated FAM-C_{15}. This unfolding upon desorption (and corresponding increase in fluorescence) should be considered when designing biosensors using FAM-C_{15}.

In comparison, we also adsorbed heated/unheated FAM-A_{15}, testing its desorption using excess A_{15} (Figure 3.9C). For C_{15}, we saw that adsorption was stronger (about 2-fold) for the heated DNA compared to the unheated DNA. This could be explained by the better stacking interactions between the DNA bases and aromatic rings of GO for the unfolded DNA. When poly-C DNA is folded into the i-motif structure, the bases are effectively "hidden" from the GO surface. For FAM-A_{15}, heating did not appear to make much of a difference, and this is consistent with its lack of a stable secondary structure at neutral pH.

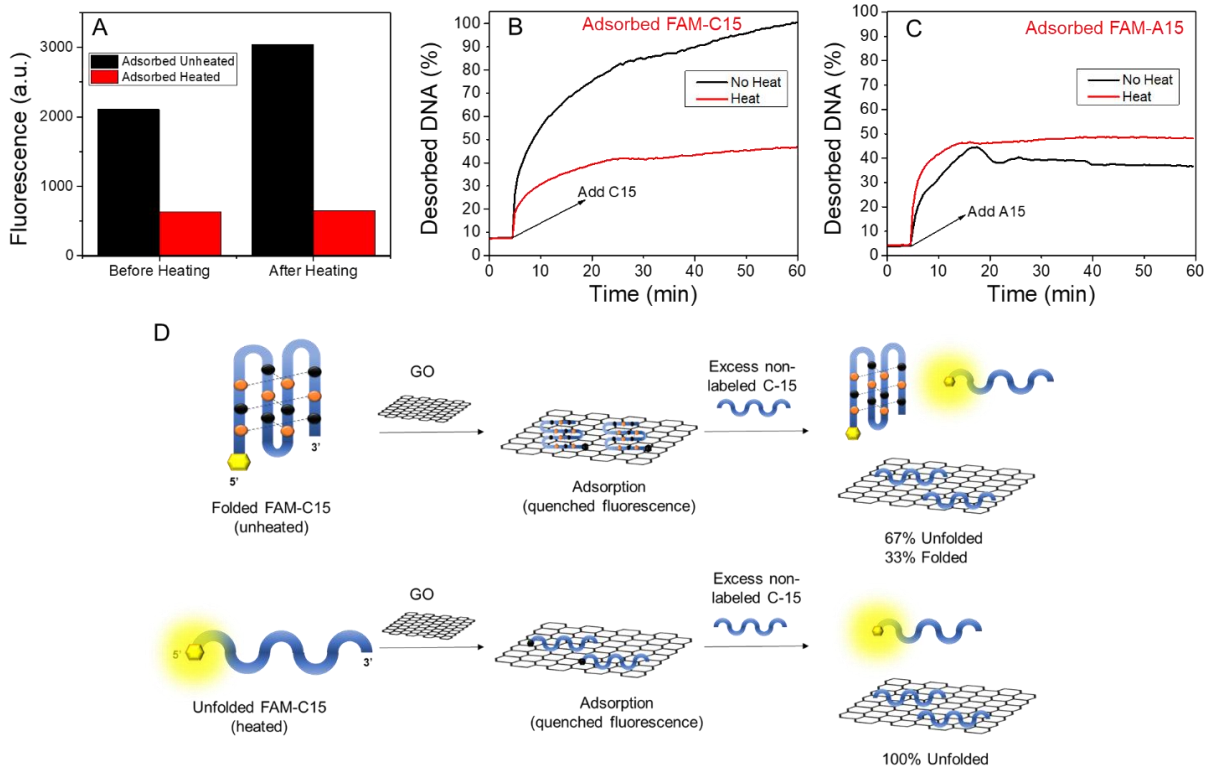

Figure 3.9. Accounting for FAM-C_{15} unfolding upon desorption from GO. (A) A comparison of desorbed FAM-C_{15} from GO before and after heating. This kind of experiment was used to generate a new calibration curve reflecting the unfolding of FAM-C_{15} upon adsorption/desorption (B) Desorption profile of FAM-C_{15} after the addition of 2 μM C_{15} accounting for the state of the

desorbed DNA (C) Desorption profile of FAM-A_{15} after the addition of 2 μM A_{15}. In all cases (A-C), the buffer was 10 mM pH 7.6 HEPES containing 300 mM NaCl. (D) General scheme showing the proposed behaviour of unheated and heated FAM-C_{15} upon adsorption and desorption from GO.

3.4 Conclusions

In this work, we set out to investigate the properties of FAM-C_{15} that made it adsorb on nanomaterials more strongly than the other DNA homopolymers. Ultimately, it was found that the FAM label can stabilize an i-motif structure even up to neutral pH, but the structure was irreversibly unfolded upon heating. The interaction between FAM and C_{15} resulted in significant static quenching of the FAM emission. The heat-unfolded FAM-C_{15} adsorbed to GO twice more strongly than when folded in the i-motif state. Interestingly, significant unfolding of folded FAM-C_{15} was seen upon desorption from GO. This unfolding resulted in higher measured fluorescence values compared to the folded structure. This study, therefore, could be useful for designing surface anchoring DNA sequences or fluorescent sensors based on poly-C DNA.

Chapter 4 -Poly-cytosine DNA Strongly Anchoring on Graphene Oxide Due to Flexible Backbone Phosphate Interactions

The results presented in this Chapter have been published as:

Anand Lopez, Yu Zhao, Zhicheng Huang, Yifan Guo, Shaokang Guan, Yu Jia and Juewen Liu "Poly-Cytosine Deoxyribonucleic Acid Strongly Anchoring on Graphene Oxide Due to Flexible Backbone Phosphate Interactions". *Advanced Materials Interfaces* **2021**, 8, 2001798.

4.1 Introduction

DNA-based biosensors have attracted significant interest due to its specific recognition of not only complementary nucleic acids but also other types of targets by DNA aptamers and DNAzymes.[193,262–268] While many of these biosensors have been implemented in molecular beacons or other homogeneous systems,[82,269,270] recent research has also interfaced DNA with nanomaterials as a framework for biosensors.[17,192,271–273] The most-studied nanomaterials for this purpose include carbon-based (such as graphene oxide (GO) and carbon nanotubes),[16,114] metallic (e.g. gold, silver),[227,274,275] and metal oxide (e.g. CeO_2, TiO_2) nanoparticles.[17]

The mode of adsorption of DNA varies with the type of nanomaterial. Adsorption can occur through electrostatic interactions (from backbone phosphate groups), coordination with the nitrogen atoms in the DNA bases, hydrogen bonding, hydrophobic and π-π stacking interactions. For most nanomaterials, the net interaction is a combination of multiple of these forces. There are certainly dominant ones, especially in metallic and metal oxide nanoparticles. In the former, the coordination with the nucleobases dominates,[23,227] whereas interactions through the phosphate group are dominant in the latter.[18,190]

Finding a strand of DNA with strong affinity to nanomaterials is critical for biosensor and materials development.[276–280] Selecting aptamers that bind to inorganic surfaces had limited success due to nonspecific adsorption of DNA. We reason that careful screening of DNA sequences is a more viable approach to examine their subtle differences in adsorption.[236] A few years ago, we reported that poly-C DNA has a generally high affinity for various nanomaterials from GO, MoS_2 to metal oxides.[186,187] Later, calcium phosphate,[245] and upconversion nanoparticles[277] were also reported to have strong affinity with poly-C DNA. This high affinity is

intriguing since the chemical reason behind it is not obvious. It was hypothesized that this high affinity was due to the formation of the "i-motif": a DNA secondary structure relying on C-C^+ interactions.[186] However, we found in the previous chapter that the i-motif structure resulted in a lower affinity to GO. Therefore, an answer to the high poly-C/GO affinity remained elusive. GO presents an interesting case as there is electrostatic repulsion of DNA combined with at least two modes of attractive interactions: hydrogen bonding and π-π stacking.[113,160,200,281,282] Hydrogen bonding can occur through the bases, as well as the sugar ring and phosphate backbone. In addition, π-π stacking can favourably occur with the aromatic regions in GO.[283]

Herein, we conducted pH-dependant experiments with various C-containing DNA strands and GO. At low pH, poly-C DNA cannot displace pre-adsorbed DNA on GO, suggesting a weaker affinity due to i-motif formation. To determine the reason for the high poly-C affinity at neutral pH, we performed molecular dynamics (MD) simulations, which showed that the phosphate backbone interacts more strongly with GO through hydrogen bonding for poly-C than other DNA homo-oligomers. This confers increased conformational flexibility on the surface of the GO, with more a more spread-out adsorbed state and increased adsorption affinity compared to other homo-oligomers of the same length. This was a surprising result as the phosphate backbone was typically not considered in GO/DNA interactions; attraction was typically attributed nucleobase/GO hydrogen bonding and π-π stacking. In the end, we were able to use this observation to generalize the tighter adsorption of poly-C DNA to various nanomaterials.

4.2 Materials and Methods

All of the DNA sequences (Table 4.1) were purchased from Integrated DNA Technologies (Coralville, Iowa, USA) and dissolved in water to a stock concentration of 100 µM. In the case of the dye-labelled strands, the stock concentration was 1 µM. 4-(2-hydroxyethyl)-1-piperazineethanesulfonic acid (HEPES), tris(hydroxymethyl) aminomethanesodium (Tris), sodium acetate, urea, sodium citrate and sodium chloride (NaCl) were purchased from VWR. 2-(N-morpholino) ethanesulfonic acid (MES) was purchased from Bio Basic Canada. Graphene oxide was purchased from ACS Materials LLC. All buffers were dissolved to a stock concentration of 500 mM and adjusted to their respective pH; 4.0 for acetate, 5.0 for citrate, 6.0 for MES, 7.6 for HEPES and 8.5 for tris. GO was dispersed in water and diluted to a stock concentration of 0.1 mg/mL. The main buffer used in this work was one of moderate ionic strength consisting of 10

mM buffer (e.g. citrate, MES, HEPES) and 300 mM NaCl. For comparison, low ionic strength (50 mM HEPES) and high ionic strength (10 mM pH 7.6 HEPES/pH 4.0 Acetate + 300 mM NaCl + 1 mM $MgCl_2$) buffers were also prepared.

Table 4.1. List of DNA Sequences Used in Chapter 4.

DNA Names	DNA Sequences (5′→ 3′)
Alexa-12mer	**Alexa Fluor 488-TCA CAG ATG CGT**
Alexa-T_{15}	**Alexa Fluor 647-TTT TTT TTT TTT TTT**
T_{15}	**TTT TTT TTT TTT TTT**
A_{15}	**AAA AAA AAA AAA AAA**
G_{15}	**GGG GGG GGG GGG GGG**
$(C_2T)_6$	**CCT CCT CCT CCT CCT CCT**
$(C_3T)_3C_3$	**CCC TCC CTC CCT CCC**
$(C_4T)_2C_4$	**CCC CTC CCC TCC CC**
C_{12}	**CCC CCC CCC CCC**
C_{15}	**CCC CCC CCC CCC CCC**
C_2T_{13}	**TTT TTT TCC TTT TTT**
C_4T_{11}	**TTT CCT TTC CTT TTT**
C_8T_7	**TTC CCT TCC TCC CTT**
$C_{12}T_3$	**CCC CCT TCC TCC CCC**

Fluorescence Measurements. All fluorescence measurements were performed in a 96-well plate in a Tecan Spark plate reader. For Alexa-T_{15}, the excitation and emission wavelengths were 634 nm and 679 nm respectively. For Alexa-12mer, the excitation and emission wavelengths were 488 nm and 535 nm, respectively. A calibration curve was generated for these two dye-labelled strands by a serial dilution from 20 nM of DNA, and this calibration curve was used for the experiments below.

Adsorption Capacity. To determine the adsorption capacity of DNA on GO, the concentration of DNA (Alexa-T_{15} or Alexa-12mer) was kept constant and titrated with GO and allowed to incubate for 1 h to allow full adsorption. Since adsorption quenches the fluorescence, any measured

fluorescence would be from free DNA. Using the calibration curve, the concentration of free DNA was calculated and further used to find the adsorbed DNA. The capacity was determined to be the first point where adding more DNA did not change the amount of adsorbed DNA.

DNA Desorption. First, GO was diluted to a working concentration of 5 µg/mL in milli-Q water. Then, 2 µL of 500 mM HEPES (pH 7.6) was added to a final concentration of 10 mM, followed by 10 µL of 3 M NaCl (final concentration: 300 mM). This was followed by 2 µL of 1 µM probe DNA (Alexa-12mer or Alexa-T_{15}) to a final concentration of 20 nM. The volume was adjusted 100 µL using water and the sample was incubated for 1 h to allow for full adsorption of the probe DNA with corresponding fluorescence quenching. Then, 1 µL of 100 µM desorbing DNA (e.g. C_{15} or $(C_3T)_3CCC$) was added and further incubation was allowed for 1 h in the dark (final concentration: 1 µM). This 1 h incubation allowed for displacement of dye-labelled DNA by the desorbing DNA, resulting in an increase in fluorescence, and this fluorescence was measured. All samples were tested at different pH: acetate (pH 4), citrate (pH 5), MES (pH 6), tris (pH 8.5), as well as at different ionic strength, in triplicate.

Circular Dichroism (CD). CD measurements were conducted with a Jasco J-715 spectrophotometer. DNA (T_{15}, $(C_2T)_6$ and C_{15}) samples were prepared in 10 mM acetate buffer (pH 6). The final concentration of DNA was 5 µM. Each sample was measured in a continuous scanning mode (from 320 to 220 nm) for 5 cycles.

Model and Molecular Dynamics Simulations. The MD simulations were performed using GROMACS version 5.1.4.[284] The employed supercell was a cuboid box of 60×60×50 $Å^3$, which consisted of saline solution and a GO sheet at the bottom with a dimension of 50×50 $Å^2$. The systems were modeled by the Amber14SB force field for DNA and ions,[285] and the TIP3P model for water molecules.[286] The force field parameters for the GO sheet, including partial charges of functional groups, were taken from Stauffer et al. and the general force field.[287,288] The electrostatic interactions were evaluated using a particle-mesh Ewald (PME) summation,[289] with a real space cut-off of 14 Å, and the Lennard-Jones (L-J) nonbonding interactions were smoothly tapered to zero when the two atoms were close to 14 Å. Three-dimensional periodic boundary conditions were applied in the simulations and all the simulations were carried out with a time step of 2 fs. The systems were relaxed for 1 ns at 300 K under the NVT ensemble via the V-rescale thermostat.

The structure of the ssDNA segment in the canonical B-form was generated using 3DNA.[290] In order to study effects coming from the reduced pH, the cytosines were additionally protonated by adding extra protons to nitrogen atoms (Figure 1C) of C_{10} and C_{15} DNA in pH 4.0.[291,292] The GO model was based on the high correlation between oxidation loci, with structural formula $C_{10}O_1(OH)_1(COOH)_{0.5}$, as reported by Yang et al..[293] The GO carbon atoms were constrained using positional restraints, while the other GO atoms, including oxygen and hydrogen, were free to move. The neutral solution environment consisted of a ssDNA, approximately 6000 water molecules and counterions of Na^+ or Cl^-, in which the optimized ssDNA was initially put at 30 Å above the GO sheet.

Each simulation of a single nucleotide and A_5, C_5, T_5 was run for 100 ns after the system reached equilibrium. For the long-chain polynucleotide ssDNA, the systems were then heated to a target temperature of 550 K (in the case of A_{10}, C_{10}, T_{10}, and A_{15}, C_{15}, T_{15}) and equilibrated for 10 ns.[294] Next, the system was cooled in a stepwise pattern, at a speed of 100 K/10 ns until a final temperature of 300 K was reached. Finally, the system was equilibrated at 300 K for 100 ns to obtain its annealed surface structure,[295] which was used for analysis of the structural details, and adsorption energies.

Analysis of simulations. The adsorption energies between the ssDNA molecules and the GO surface, which consisted of the van der Waals energy and the electrostatic energy, were calculated after the system reached equilibrium. The radius of gyration (*Rg*) for every simulation sample was calculated as follows:

$$R_g = \left(\frac{\sum_i r_i^2 m_i}{\sum_i m_i} \right)^{1/2},$$

where m_i is the mass of atom i and r_i the position of atom i with respect to the center of mass of the molecule. R_g reflects the volume and shape of biomolecules. A larger R_g means a more extended molecular structure. Hydrogen bonds were determined using geometrical criteria: H-A distance <0.27 nm, D-A distance <0.335 nm, and D-H-A angle >90°, in which H, A, and D denote a hydrogen, acceptor, and donor atom, respectively. The geometrical criterion of the π–π stacking structure was defined as vertical separation of less than 0.45 nm and angles of less than 30 degrees between the planes of the GO sheet and the DNA bases.[296] The contact surface area (CSA) is

defined as half of the difference between the solvent accessible surface area (SASA) of the ssDNA/GO complex and the sum of the SASAs of the ssDNA segment and the GO.[155]

4.3 Results and Discussion

4.3.1 Poly-C DNA has a pH-dependant affinity to GO

To measure the relative adsorption affinity of DNA to GO, we adsorbed a random sequenced 12-mer with an Alexa Fluor 488 label (Alexa-12mer) to achieve quenched fluorescence. By adding increasing concentration of GO to 20 nM Alexa-12mer (Figure 4.1A), saturated quenching was achieved with 5 μg/mL GO, which was used for subsequent fluorescence experiments. To the Alexa-12mer/GO complex at pH 7.6, we respectively added 50-fold excessed non-labeled 15-mer DNA homo-oligonucleotides (i.e. A_{15}, T_{15}, C_{15} and G_{15}, 1 μM each). The strand with the highest affinity would displace the most Alexa-12mer, which could be quantified by measuring fluorescence increase. We confirmed that poly-C had the highest affinity to GO, which was followed by A_{15}, G_{15} and T_{15} (Figure 4.1B).

We then sought to determine whether this affinity ranking was true over a wide pH range. Since Alexa Fluor dyes are less sensitive to pH, we were able to directly follow the desorption at different pH (Figure 4.1C). In an alkaline condition (pH 10), C_{15} maintained the highest affinity, but G_{15} replaced A_{15} with the second-highest affinity. Again, T_{15} showed the weakest affinity. We reason that the higher affinity for C_{15} in mildly alkaline conditions is due to the same reason as that at neutral pH, since cytosine has a second pK_a of 12.2 and pH 10 would not change its protonation state. The N1 position of guanine has a pK_a of 9.2, which could explain the stronger adsorption of G_{15} at pH 10.

In acidic conditions (pH 3.0 and 4.0), the affinity of C_{15} and G_{15} (to a lesser extent) drastically decreased, whereas A_{15} became the highest affinity sequence. C_{15} can form the i-motif structure in acidic conditions due to the protonation of the N_3 in cytosine around pH 4.2 (Figure 4.1D).[45] The i-motif has a weaker affinity to GO due to shielding of the bases in the folded structure (less groups on the DNA for interaction with GO). A_{15} presents an interesting case: adenine can also be protonated at low pH (the pK_a of the N_1 is 3.5), while the associated secondary structure (the A-motif formed by two parallel poly-A strands) does not form unless the pH is around 3.[297] Since the A-motif is a rigid duplex, its adsorption would be unfavorable on GO. At pH 3, there was indeed a decrease in the DNA desorbed compared to pH 4, which suggested the effect of A-

motif structure formation. Without stable secondary structures, a DNA is adsorbed more strongly at lower pH due to decreased charge repulsion.[298] However, such effects should favor both the adsorbed Alexa-12mer and the added DNA. The relatively decreased affinity of C_{15} compared to A_{15} upon decreasing pH suggested the i-motif was at least partially responsible for this decrease in C_{15} affinity.

We also adsorbed a T_{15} DNA bearing an Alexa Fluor 647 label (Alexa-T_{15}) and then conducted similar desorption experiments to further confirm the above results (Figure 4.1E). In general, A_{15} induced the most desorption. This was likely due to complementary interactions between A_{15} and the adsorbed Alexa-T_{15}. Beyond this, a difference in the trend across the pH conditions tested was observed. For example: at pH 7.6, the affinity ranking was $A_{15}>C_{15}>G_{15}>T_{15}$, while at pH 4, it was $A_{15}>T_{15}>G_{15}>>C_{15}$. Again, the most striking difference was the excellent affinity of C_{15} at neutral pH compared to the very low affinity at low pH.

It was previously reported that the i-motif structure was stabilized by various nanosized carbon materials, such as single-walled carbon nanotubes,[253,254] fullerene,[255] and graphene quantum dots.[256] In this work, we focused on the adsorption strength (DNA/GO interactions) instead of the stability of i-motif (intramolecular interactions). Our results indicated that formation of i-motif is not the reason for the tighter adsorption of poly-C DNA at neutral pH, but instead it can weaken poly-C adsorption especially at low pH. Another consideration is ionic strength. A high ionic strength is needed to screen the electrostatic repulsion between GO and DNA. Its effect on the stability of the i-motif is more controversial, though recently we observed destabilization at high salt concentrations.[299] We prepared buffers of low and high ionic strength to compare to our main buffer of moderate ionic strength. After adsorbing Alexa-T_{15} on GO at different ionic strength, we added C_{15} to displace it (Figure 4.1F). At neutral pH, more desorption was observed at high ionic strength, likely reflecting the decreased electrostatic repulsion. At low pH, increased ionic strength decreased Alexa-T_{15} desorption by C_{15}, suggesting that even if there was partial destabilization of the i-motif, it was not enough to increase C_{15} affinity to GO. The striking difference of C_{15} at different pH presents an interesting question: what factor drives the high affinity of C_{15} to GO at neutral pH? In the following sections, we attempted to answer this through a systematic change in DNA sequences.

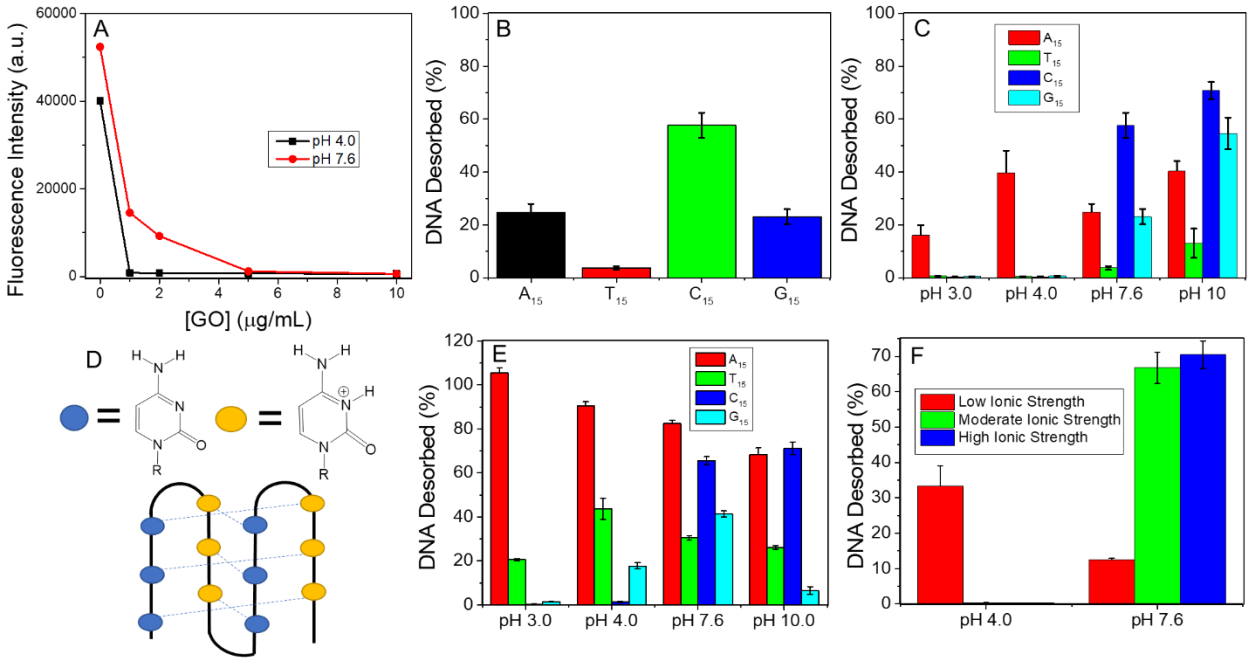

Figure 4.1. Confirming the high adsorption affinity of poly-C DNA on GO. (A) Adsorption capacity of Alexa-12mer DNA on GO at pH 4.0 and pH 7.6. Experiments conducted using [Alexa-12mer] = 20 nM, 10 mM HEPES (pH 7.6) or 10 mM acetate (pH 4.0) buffers and 300 mM NaCl. (B) Adding various 15-mer sequences to GO saturated with Alexa-12mer DNA at pH 7.6 (HEPES, 10 mM). (C) Adding various 15-mer sequences to GO saturated with Alexa-12mer at pH 10 (carbonate, 10 mM), pH 7.6 (HEPES, 10 mM), pH 4.0 (acetate, 10 mM) and pH 3.0 (citrate, 10 mM). (D) A scheme for the i-motif structure. (E) Adding various 15-mer sequences to GO saturated to Alexa-T_{15} at different pH. (F) Desorption of Alexa-T_{15} (20 nM) from GO (5 μg/mL) by C_{15} (1 μM) in buffers of differing ionic strength. Low ionic strength was 50 mM HEPES (pH 7.6)/acetate (pH 4.0). Moderate ionic strength was 10 mM HEPES (pH 7.6)/acetate (pH 4.0) and 300 mM NaCl. High ionic strength was 10 mM HEPES (pH 7.6)/acetate (pH 4.0), 300 mM NaCl and 1 mM $MgCl_2$.

4.3.2 The arrangement of cytosine within DNA sequence does not significantly affect affinity

To rigorously understand pH-dependant changes with poly-C DNA, we first varied the arrangement of the C-bases within a strand. We designed 4 sequences that contained 12 cytosine (C) bases but were arranged differently and spaced by single thymine (T) bases. These are

designated as $(C_2T)_6$, $(C_3T)_3C_3$, $(C_4T)_2C_4$ and C_{12} in Table 1. In these sequences, two, three, four and twelve consecutive C bases are grouped. There were chosen to investigate if consecutive cytosines were responsible for its high affinity to GO. Inserting thymine may potentially result in an altered affinity. These strands were respectively added to induce desorption of Alexa-T_{15} from GO as shown in Figure 4.2A. This time, we also added pH 5, pH 6 and pH 8.5 to construct a more detailed picture of the pH dependence.

All these sequences had a higher displacing ability at a higher pH, while the control sequence, T_{15}, was quite pH-independent. The major jump occurred between pH 6 and 7.6 for C_{12}, and between pH 5 and 6 for $(C_2T)_6$ and $(C_3T)_3C_3$ which were not only slightly longer, but also had more T bases. Therefore, it appeared that the addition of a few T would increase the affinity to GO at low pH. We then conducted circular dichroism (CD) experiments at pH 6 for all the samples. (Figure 4.2B). As expected, T_{15} showed no obvious features indicative of a significant secondary structure. C_{12} displayed the typical spectrum with a sharp positive peak at ca. 288 nm and a weaker negative peak at ca. 260 nm indicative of an i-motif,.[39] With $(C_2T)_6$, $(C_3T)_3C_3$ and $(C_4T)_2C_4$, the spectra were quite similar to C_{12}, indicating that their structures were most likely in its i-motif form. Likely, the C-rich DNA with more thymine insertions can more easily collapse on the GO surface, although the free DNA may fold into i-motif like structures.

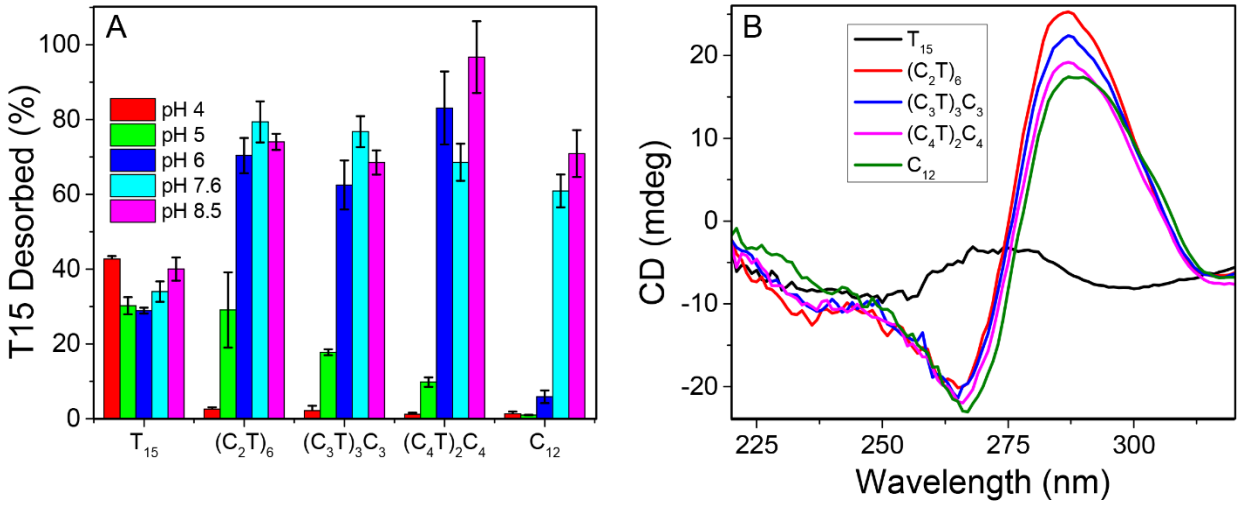

Figure 4.2. Varying the arrangement of C to study adsorption affinity. (A) Adding DNA with various arrangements of a total of 12 cytosine bases to GO saturated with Alexa T_{15} at pH 4

(acetate, 10 mM), pH 5 (citrate, 10 mM), pH 6 (MES, 10 mM), pH 7.6 (HEPES, 10 mM) and pH 8.5 (Tris, 10 mM). (B) CD spectra of the DNAs (5 μM) at pH 6 (10 mM MES).

4.3.3 Adding cytosine to a predominantly thymine strand significantly improves affinity to GO at low pH.

In the previous section, we kept the number of C in the sequence constant but varied the arrangement. We then kept the DNA sequence length the same and varied the C content within it. We designed the sequences with 2, 4, 8 and 12 cytosines, respectively (see Table 1 for sequence), while also comparing them to T_{15} and C_{15}. We chose these sequences to observe if there was a threshold of C needed before the affinity was sharply increased, and whether there was a simple linear increase in affinity with increasing the fraction of C. Again, GO adsorbed with Alexa-T_{15} at pH 4 and pH 7.6 were used as probes (Figure 4.3A). At pH 7.6, the affinity appeared to increase monotonously with the C content, consistent with C interacting more strongly with GO compared with T. However, this trend changed significantly when the pH was lowered to 4, where both T_{15} and C_{15} showed low affinities as was seen previously but adding a small number of C bases (i.e. 2 or 4) to a T-rich strand significantly increased the affinity to GO. We reason that the presence of a few scattered cytosines enhanced the adsorption affinity by their individual contributions. When C became the dominating base in the DNA, the tendency to form the i-motif took over and the affinity then decreased. This trend confirms previous reports that there needs to be a certain number of C within a strand to form a stable i-motif (specifically >10 cytosine).[261] We also repeated this experiment using adsorbed Alexa-12mer (Figure 4.3B). Interestingly, while the pH 7.6 trend was preserved, very little Alexa-12mer desorbed at pH 4, which (combined with the data in Figure 4.1) suggests that Alexa-T_{15} adsorbed much weaker under these conditions than Alexa-12mer. While we were able to systematically confirm the strong adsorption affinity of poly-C DNA to GO at neutral pH, the reason appeared to be elusive experimentally. Therefore, we resorted to computer simulation to gain further insights.

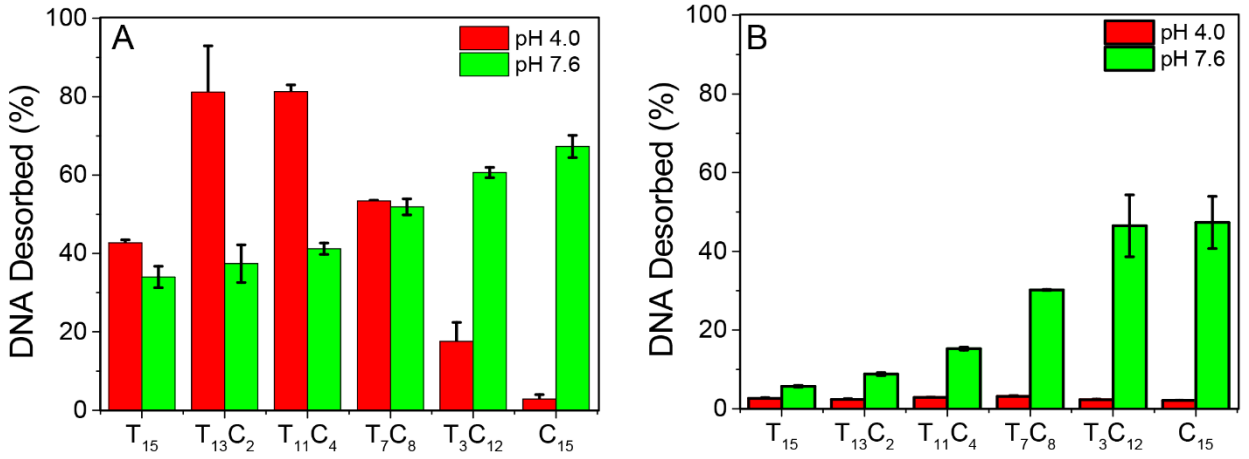

Figure 4.3. Addition of 15-mer DNA with increasing C/T ratios to GO saturated with (A) Alexa-T_{15} and (B) Alexa-12mer at pH 4 (acetate, 10 mM) and pH 7.6 (HEPES, 10 mM).

4.3.4 Phosphate backbone hydrogen bonds potentially responsible for poly-C affinity to GO

To further understand the interactions between polynucleotides and GO, MD simulations were used to calculate the adsorption energies of poly-A, poly-C and poly-T DNA on GO (Figure 4.4A). It was seen that poly-C had the lowest (most favorable) adsorption energy at longer lengths (10- and 15-mers). This was followed by T and A (for the 15-mer), though the difference at 5-mer or shorter DNA was not obvious. Furthermore, we calculated the relative contributions of attractive forces on GO for the 15-mers (Figure 4.4B). The contributing interactions were split into hydrogen bonds (HBs) and π-π stacking interactions. Within HBs, we further split the contributions to the nucleobase and GO (HB-base) and the phosphate backbone and GO (HB-backbone). For poly-C, the most obvious contribution is the HBs between the phosphate backbone and GO, nearly 4-fold higher than poly-T and poly-A (Figure 4.4B, 4.4C). Even though poly-A and poly-T DNA have higher calculated π-π stacking interactions and higher HB-base interactions with GO, the HB-backbone interactions that are predominant in poly-C DNA make it adsorb on GO the most stably. This strong phosphate backbone H-bond contribution with poly-C appears anomalous, since poly-T and poly-A both have the same phosphate backbone and, in principle, should have a similar contribution. The lack of interaction between the cytosine base and GO (compared to adenine and thymine), appeared to make long-chain C DNA more flexible, allowing it to adjust its geometry during adsorption. This was confirmed by the simulated radius of gyration (R_g) and contact surface

area (CSA) for A_{15}, C_{15}, T_{15} upon adsorption to GO, which suggested that adsorbed C_{15} had the most extended conformation since its R_g and CSA were the largest (Figure 4.4 D, E). This extended conformation on GO with exposed bases may be more favorable entropically, forming more HB-backbone interactions than the other polynucleotides.

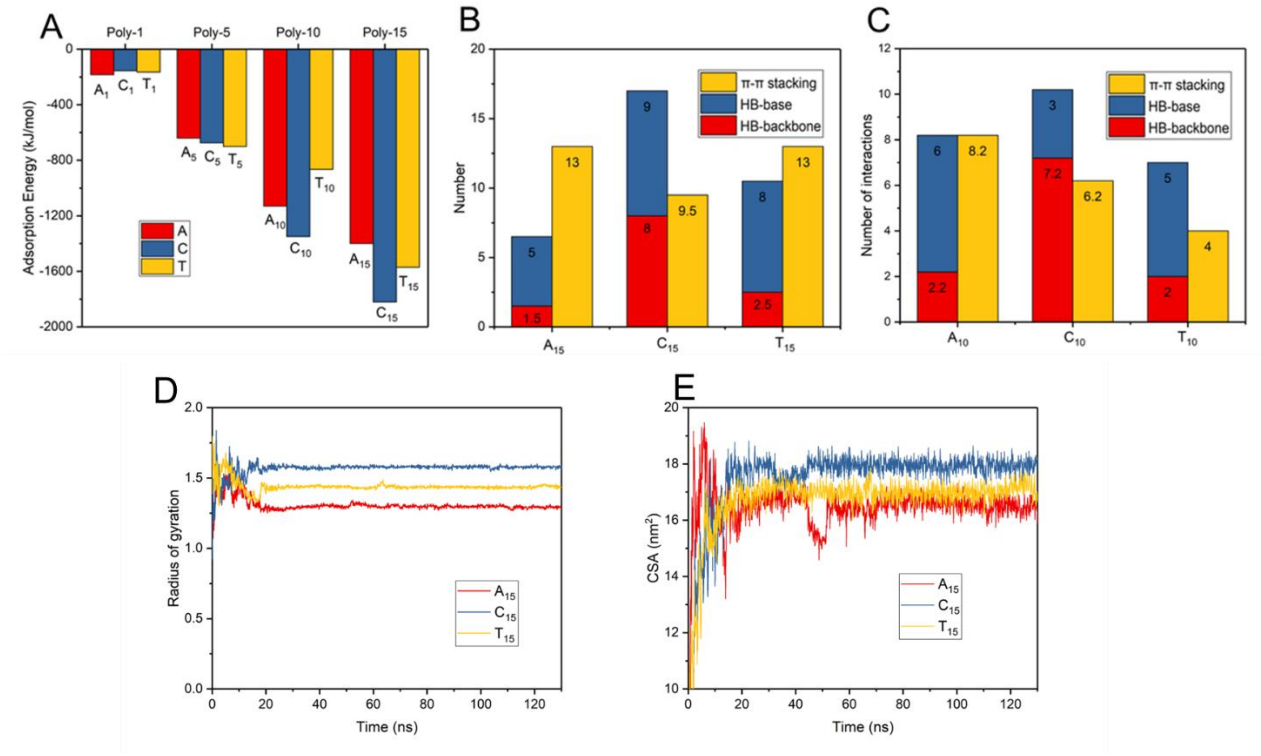

Figure 4.4. MD simulations calculating various parameters of adsorption of DNA 10-mers and 15-mers on GO. (A) Calculated adsorption energies of A, T and C oligomers on GO. (B) Distribution of GO/DNA interactions of the three types of 15-mer oligomers. (C) Distribution of GO/DNA interactions of 10-mer oligonucleotides organized by the type of forces. (D) Simulated radius of gyration (R_g) for A_{15}, C_{15} and T_{15} adsorbed on GO after 130 ns of equilibration at pH 7.0. (E) Contact surface area (CSA) calculations for A_{15}, C_{15} and T_{15} adsorbed on GO after 130 ns of equilibration at pH 7.0.

We also simulated the adsorption energies of C_{10} and C_{15} at neutral (pH 7.0) and low pH (pH 4.0) (Figure 4.5A). As expected, the adsorption at pH 4.0 was less stable than that at pH 7.0 for both polynucleotides. In a similar way to above, we calculated the contributions of HBs and

separated them into HB-inter (GO-DNA) and HB-intra (DNA-DNA) classes (Figure 4.5B). At low pH, the number of HB-intra sites was almost 3-fold higher than at neutral pH. This supports the formation of the i-motif caused by intramolecular HBs between C and C^+. The HB-inter increased significantly from low pH to neutral pH in both C_{10} and C_{15} (6- and 8- fold, respectively), indicating more HBs between GO and these DNA at pH 7.0. To visualize this, we captured the steady state conformations of the pH 7.0 (Figure 4.5C) and pH 4.0 samples (Figure 4.5D). At neutral pH, C_{15} is spread out, occupying a larger area on GO, attributable to the phosphate HBs mentioned above. We should emphasize that since the strands were manually protonated (i.e. protons added at the designated position) in the simulation, the pH 7.0 condition here would be more consistent with the mildly alkaline condition experimentally. In previous sections, we outlined that the reason why C_{15} has a high affinity is the same for neutral and alkaline pH as a result of an extended transition of protonation. At low pH, the interaction between GO and C_{15} was less, with intramolecular HBs resulting in the formation of the i-motif. This explains the decreased affinity of C_{15} to GO at low pH.

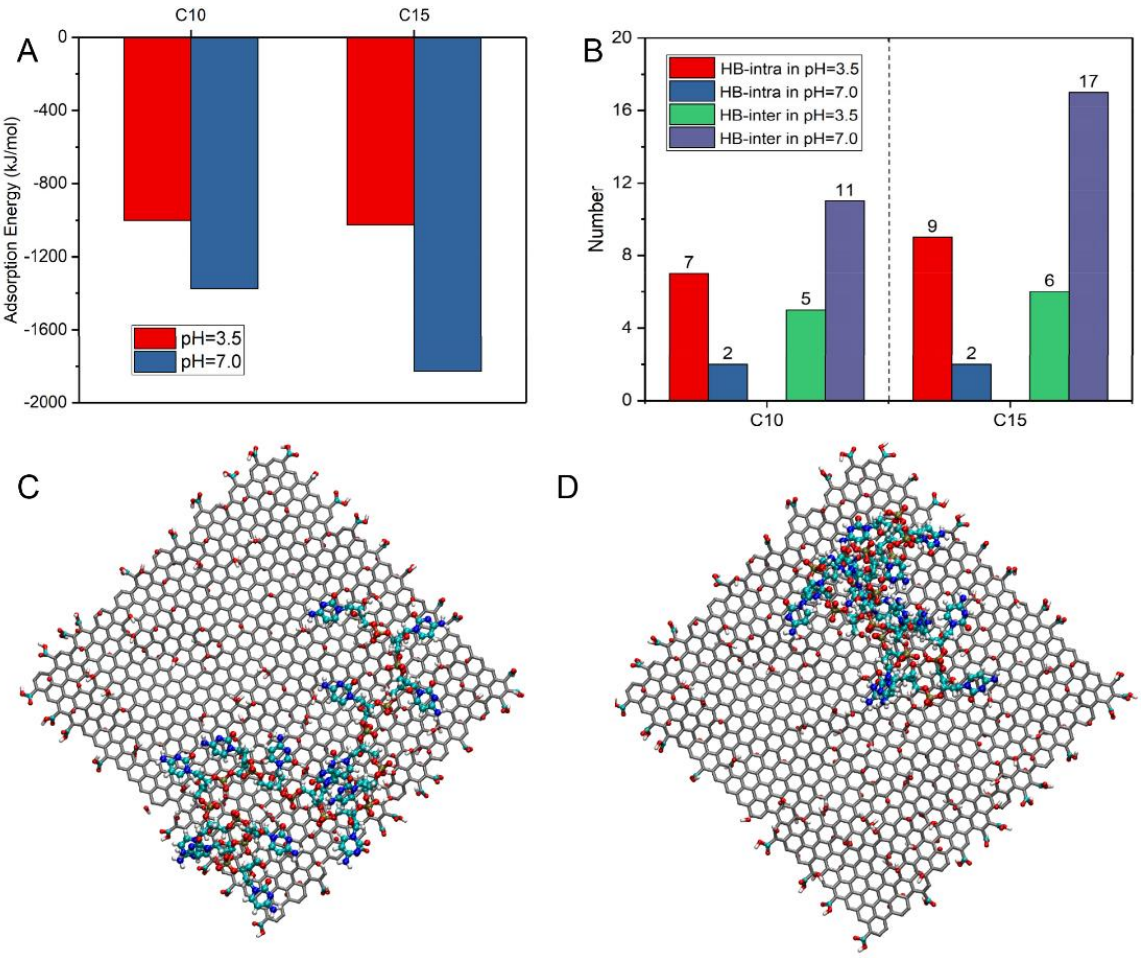

Figure 4.5. pH-dependent MD simulations of C_{10} and C_{15} adsorption on GO. (A) Calculated adsorption energies of C_{10} and C_{15} DNA adsorbed at pH 4.0 and pH 7.0. (B) Distribution of DNA-DNA HB (HB-intra) and GO-DNA HB (HB-inter) at pH 4.0 and pH 7.0. Simulated steady state conformations of C_{15} on GO at (C) pH 7.0, and (D) pH 4.0.

Apart from limiting HBs between the base and GO, it is conceivable that the formation of the i-motif will also limit the HBs between the phosphate backbone and GO. This is because these poly-C strands will be folded (instead of extended), limiting the number of interacting phosphates per strand. This is supported by lower R_g values for both C_{10} and C_{15} at low pH (Figure 4.6A). The consistency between theory and experiment supports our conclusion that the phosphate backbone HBs (coupled with the higher flexibility of C_{15}) has a significant role to play in the anomalously high stability of poly-C DNA.

The above simulations were performed on GO. We further compared the adsorption of C_{15} and A_{15} on pristine graphene in aqueous solution. For both, the conformation was dictated entirely by π-π interactions between the bases and the graphene surface (Figure 4.6B). The adsorption energy of A_{15} was also lower compared to that of C_{15} (Figure 4.6C), indicating stronger binding for the former. This is reasonable due to the larger purine ring for adenosine compared to the smaller pyrimidine ring for cytidine, despite that both form the same number of π-π stacks (Figure 4.6D).

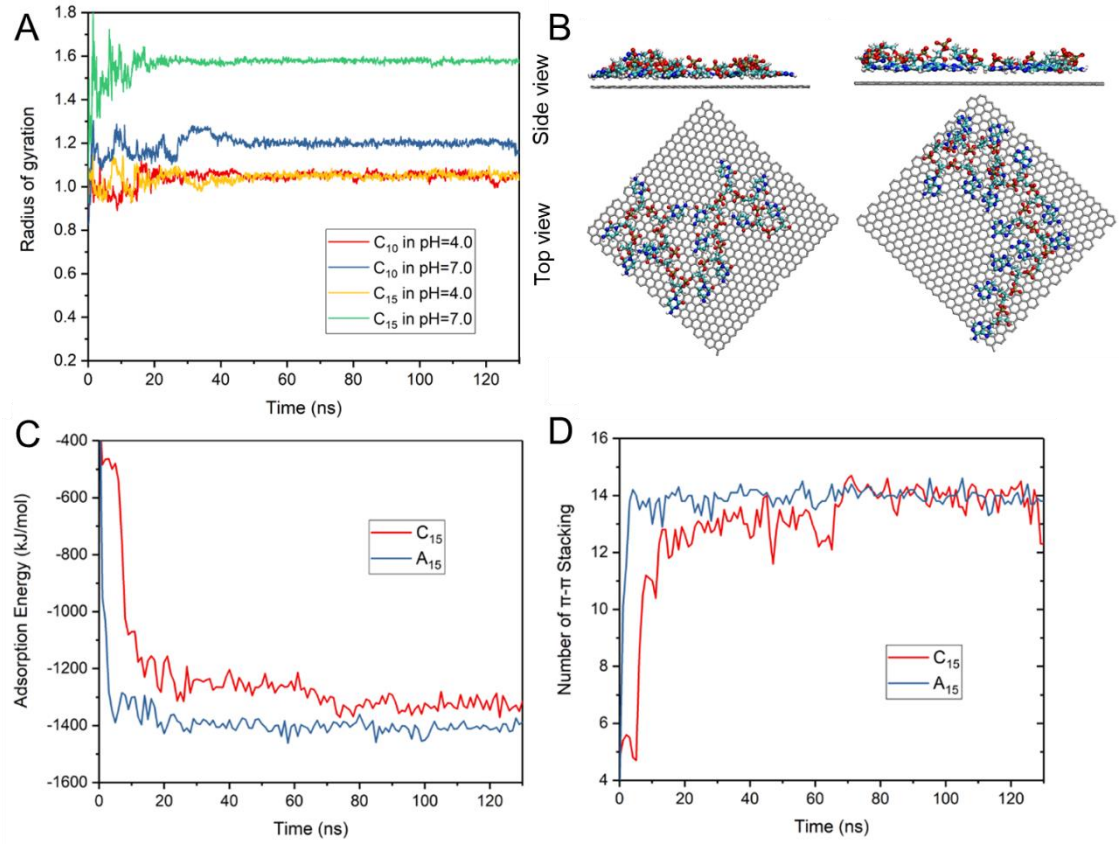

Figure 4.6. MD simulations of C_{10}, C_{15} and A_{15} adsorbed on GO and pristine graphene. (A) Simulated radius of gyration (R_g) for C_{10} and C_{15} adsorbed on GO after 130 ns of equilibration at pH 4.0 and 7.0. (B) Steady state conformations of C_{15} (left) and A_{15} (right) adsorbed on pristine graphene. Adsorption energy (C) and π-π stacking number (D) for C_{15} and A_{15} adsorbed on pristine graphene for 150 ns.

4.4 Discussion

Experimentally, it is known that hydrogen bonding is highly important for the adsorption of DNA on GO.[300] It was thought that the hydrogen bonding was predominantly between the base and the GO surface, as that would account for the differences in affinity between the bases and GO. However, for poly-C DNA, much of the hydrogen bonding contributions at neutral pH is from the phosphate backbone. Based on our simulations, the hydrogen bonds with the phosphate backbone are responsible for the high affinity of poly-C DNA on GO. We previously showed stronger poly-C DNA adsorption on various metal oxides,[186] calcium phosphate,[245] and recently Ge et al. showed stronger poly-C adsorption on upconversion nanoparticles.[277] For all these metal containing materials, they can interact strongly with DNA phosphate backbone, which can also explain the stronger adsorption of poly-C DNA by its flexibility at neutral pH allowing more phosphate backbone interactions. The difference is that, for GO, the phosphate backbone uses hydrogen bonding, while on those metal containing materials, phosphate backbone uses electrostatic and Lewis acid/base interactions.

It should be noted that free inorganic phosphate cannot displace DNA from GO.[18] Furthermore, DNA can be displaced by individual nucleosides (such as adenosine), and some surfactants.[199] The heterogeneity (e.g. pristine hydrophobic vs oxidized hydrophilic) of the GO surface has also been shown to correspond to different binding modes,[150,156] and DNA strands (regardless of the base) utilize a combination of them depending on the degree of oxidation of GO. This is reflected in our simulations with different contributions from HBs and π-π stacking (Figure 4.4B). We speculate that the nucleosides are larger than inorganic phosphate, and they can utilize both π-π stacking and base-GO HBs to form combined interactions to better displace DNA from GO. On the other hand, free phosphate is very small and individually it cannot overcome the combined attractive forces (including π-π stacking and base HBs) between DNA and GO.

Based on this and our previous works, we can now paint a picture of the best methods to physisorb DNA on to GO. It should be noted that "best" in this context is dependent on specific applications and is summarized in Figure 4.7. If a sensing DNA needs to be anchored to the surface of GO, then a poly-C strand is the best option at neutral pH (Figure 4.7A). Due to phosphate backbone HBs, C_{15} interacts with more of the GO surface, leading to very stable adsorption. The sensing probe is not adsorbed as strongly and will be available to bind targets. At low pH, the

sensing probe will be adsorbed too strongly to GO (e.g. the Alexa-12mer used in Figure 4.3B) and will not bind to target. Interfacing C-rich DNA on GO with pH can also be used to make pH-dependent switches (Figure 4.7B), exploiting the difference in binding affinity due to i-motif formation.[257,301] Random/sensing DNA strands simply adsorbed on GO are most effective at neutral pH (Figure 4.7C),[298] since the interaction at low pH is too strong for probe to desorb. Similar designs are also applicable to other nanomaterials interacting with the DNA phosphate backbone.

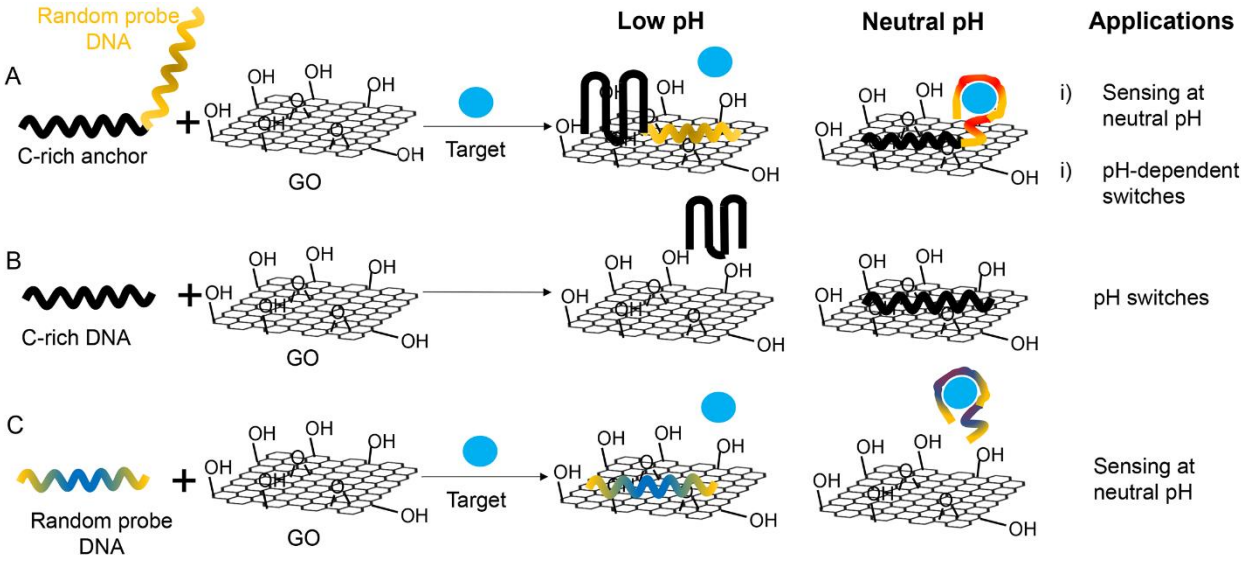

Figure 4.7. General schemes for applying C-rich DNA in various applications. (A) The adsorption of a diblock DNA with a poly-C or C-rich block and a sensing block on GO for the detection of target. Such a system displays pH and block-dependent affinities to GO, with weak poly-C affinity at low vs high pH and vice-versa for the sensing block. Target sensing may only be achieved at neutral pH. (B) The adsorption of simple C-rich DNA on GO useful for pH-dependent switches. (C) The adsorption of a simple sensing probe on GO. Target binding and subsequent desorption may only occur at neutral pH.

4.5 Conclusions

In this work, we sought to gain a fundamental understanding of the nature of poly-C DNA interactions with GO. First, it was confirmed that the i-motif structure formed by C_{15} at low pH had a lower affinity to GO, which was consistent with our previous studies. This affinity was much

lower than any of other DNA tested (T_{15}, A_{15} and G_{15}). Furthermore, we confirmed the anomalously high affinity of poly-C to GO at neutral pH compared to other DNA homo-oligomers of similar length. The arrangement of C within the strand did not affect the affinity, suggesting that intra-strand interactions were not responsible for the high affinity. Increasing C content in a strand monotonously increases the affinity at neutral pH. However, at low pH, there was an increase in affinity at low C content, followed by a sharp decrease once C was >50% of the strand. This confirmed that there was a minimum number of C required for i-motif formation, which correlated well with the decrease in affinity. Using MD simulations, we modeled a series of DNA/GO adsorption events, measuring various useful parameters such as adsorption energy, radius of gyration and contact surface area. We found that poly-C strands had a significantly greater phosphate backbone/GO hydrogen bond contribution to the adsorption, which resulted in a more flexible and spread-out adsorption conformation. This ultimately allowed for a very stable poly-C adsorption on GO. This phosphate interaction also explains why poly-C maintains this high affinity on other surfaces (such as metal oxide nanoparticles), except that the phosphate would interact through Lewis acid/base or electrostatic interactions instead of hydrogen bonding. To summarize, the reason why poly-C has such a high affinity for many nanomaterials may be due to the increased conformational flexibility allowing phosphates being the predominant mode of interaction. This knowledge will allow for the rational design of nanomaterial/DNA hybrid materials.

Chapter 5 - Fluorescence Polarization for Probing DNA Adsorption to Nanomaterials and Fluorophore/DNA Interactions

The results presented in this Chapter have been published as:

Anand Lopez and Juewen Liu "Fluorescence Polarization for Probing DNA Adsorption by Nanomaterials and Fluorophore/DNA Interactions". *Langmuir* **2019**, 35, 30, 9954–9961.

5.1 Introduction

A fluorophore has many properties. While fluorescence intensity or quantum yield is easy to measure, it is affected by lamp intensity, detector gain, and fluorophore concentration. This makes them difficult to calibrate.[302] Fluorescence polarization (FP) measures tumbling of fluorophores during its excited state (typically a few nanoseconds), which is independent of fluorophore concentration but affected by molecular volume. FP is useful for measuring binding, such as DNA-protein and protein-protein interactions, since coupling of a fluorophore-labeled DNA or protein to a larger protein causes an increase in FP. [79,104,303–306]

In recent years, FP has been used to characterize DNA adsorption by nanomaterials.[307–317] Since nanomaterials often have much greater mass and volume than proteins, they are expected to significantly increase FP of adsorbed fluorophores. As an example, fluorescence anisotropy was used to detect ATP using a fluorophore-labeled DNA aptamer (anisotropy and polarization are interconvertible).[318] ATP binding inhibited aptamer adsorption on graphene oxide (GO). Without ATP, the aptamer adsorption resulted in a high anisotropy value. The change in the anisotropy was linearly dependent on the concentration of ATP. A similar method was recently utilized to detect aflatoxin B_1.[319]

DNA adsorption by nanomaterials, such as GO,[157,320–322] gold nanoparticles,[323–325] MoS_2,[235,326] and most metal oxide nanoparticles,[18,327] is accompanied with strong fluorescence quenching of the attached fluorophore. Such quenching has been extensively used for biosensor development.[82,328–332] Quenching may change the contribution of the adsorbed DNA in the total measured FP. In other words, the FP of strongly quenching systems may not linearly correlate with adsorption efficiency. This aspect, however, has yet to be carefully examined. In addition, different fluorophores may interact with the DNA backbone differently, which may further complicate data

analysis. In this work, we systematically measured DNA adsorption by GO as a strong quencher, and by Y_2O_3 as a non-quencher. We mathematically related adsorption efficiency and quenching efficiency to the change in FP. We found that FP measurements from a strong quenching system was dominated by scattering/intrinsic fluorescence of the material, rather than an increase in effective molecular volume of the fluorophore. For non-quenching surfaces or materials, the typical binding model can be used. We also noticed DNA/fluorophore interactions that can be probed by FP.

5.2 Materials and Methods

Chemicals. Carboxyfluorescein (FAM)-labeled A_{15} and T_{15} DNA, as well as TYE^{TM}665-T15 were purchased from Integrated DNA Technologies (Coralville, IA). Fluorescein isocyanate-labeled polyethylene glycol (FITC-PEG, MW 10000 Da) was from Nanocs Inc. (Boston, MA). FITC-bovine serum albumin (FITC-BSA), CeO_2 dispersion (size 5-10 nm, in acetate buffer) and fluorescein were purchased from Sigma-Aldrich. Graphene oxide and Y_2O_3 powders were purchased from ACS Materials LLC.

Dilution experiments. The fluorescent species (e.g. free fluorescein or FAM-T_{15}) were dissolved in 10 mM HEPES buffer (pH 7.6) at a starting concentration of 1 μM in a black 96-well plate. A serial dilution was then performed, with each subsequent concentration being half of the previous one, to achieve sub-nM concentrations. The FP and intensity of each sample were measured by excitation at 485 nm and collecting emission at 535 nm in a plate reader (Tecan Spark). The gain was automatically adjusted by the instrument in cases where there were fluorescent species present. For dilution experiments involving TYE^{TM}665-T_{15}, the excitation was at 621 nm, and emission at 665 nm. For experiments with nanomaterials only (no fluorophores), a 100 nM FAM T_{15} sample was included for gain adjustment. All experiments were run in triplicate, and the error bars represent 1 standard deviation from the mean.

pH-dependent FP. For the pH measurements, the concentration of the fluorescent species was at 20 nM. pH 4, 6, and 7.6 were achieved by using 10 mM acetate, MES, and HEPES, respectively. The samples were then placed in a 96-well plate and the FP was measured in triplicate.

Adsorption on nanomaterials. The fluorophore (e.g. FAM-T_{15} DNA) concentration was kept at 20 nM and varying concentrations of nanomaterials were added. The samples were then transferred to a 96 well plate and the FP was measured. All measurements were performed in 10 mM HEPES

(pH 7.6). For GO, the experiment was performed with (high affinity) and without (low affinity) 300 mM NaCl.

DNA adsorption efficiency on Y_2O_3. Various concentrations of Y_2O_3 were added to 20 nM FAM-T_{15} and allowed to incubate for 30 min, followed by centrifugation. The fluorescence of the supernatant was measured and compared to a calibration curve to get the free DNA concentration. The adsorbed DNA was then calculated by subtracting the free DNA concentration from the total DNA concentration. All measurements were performed in 10 mM HEPES (pH 7.6).

5.3 Results and Discussion

5.3.1 Lower limit of fluorescence intensity for FP

$\mathrm{FP} = (I_{II} - I_{\perp})/(I_{II} + I_{\perp})$, where I_{II} and $I_{\perp}$ are the emission intensities polarized parallel and perpendicular to the excitation light plane, respectively. After excitation by a polarized light, if the excited fluorophore can tumble quickly during its excited state, the emitted fluorescence is depolarized. On the other hand, if it tumbles slowly (e.g. by attaching to a larger moiety), the emitted fluorescence is still highly polarized, yielding a high FP. Therefore, FP is strongly affected by the molecular volume and fluorescence lifetime. FP is a ratio without a unit (typically in the range between -0.3 and 0.5), but it is often expressed in mP (e.g. FP of 0.1 would be expressed as 100 mP).

In principle, FP is independent of fluorescence intensity. This being said, there should still be a limit below which artifacts of low fluorescence may appear. Since we are interested in DNA adsorption by strongly quenching materials, it is important to measure this limit. We prepared a series of free fluorescein solutions (no DNA attached) from 10 pM to 1 μM. Fluorescein derivatives have been widely used for labeling biomolecules, including DNA. A good linearity in fluorescence intensity was found for both the parallel and perpendicular light even at sub-nM concentrations (Figure 5.1A), indicating excellent sensitivity of the instrument. The FP was around 0 when fluorescein was 1 nM or higher (Figure 5.1D), consistent with the low molecular volume of free fluorescein.

We then tested two FAM-labeled DNA: FAM-A_{15} (Figure 5.1B, 5.1E) and FAM-T_{15} (Figure 5.1C, 5.1F). Upon dilution, both DNAs showed very nice linearity in fluorescence intensity. The FP was still quite low, only around 10 mP, indicating that the FAM label could still

tumble quite freely despite conjugation to DNA. Only at extremely low concentrations (below 1 nM) did we observe a significant increase in FP. By comparison with fluorescence intensity, the free fluorescein sample fluoresced stronger than the DNA-labeled ones at the same concentration, although the critical intensity was around 100 fluorescence units.

In our experimental setting, if the total fluorescence intensity was above 100 units (this value could be different for different instruments and settings), the artifacts associated with low fluorescence intensity should not come into play. This translates into a DNA concentration of around 1 nM, and a free fluorescein concentration of about 0.5 nM. At a much lower fluorescence intensity, we cannot make any conclusions on the properties of the fluorophores based on FP. Once a fluorophore is sufficiently diluted, the measured fluorescence would be indistinguishable from the background. Contributions from scattered light then started to show up, which could be highly polarized.[333] This can be interpreted as artifacts associated with low fluorescence intensity. We determined the limit here, and such extreme cases were not quantitatively considered in this work.

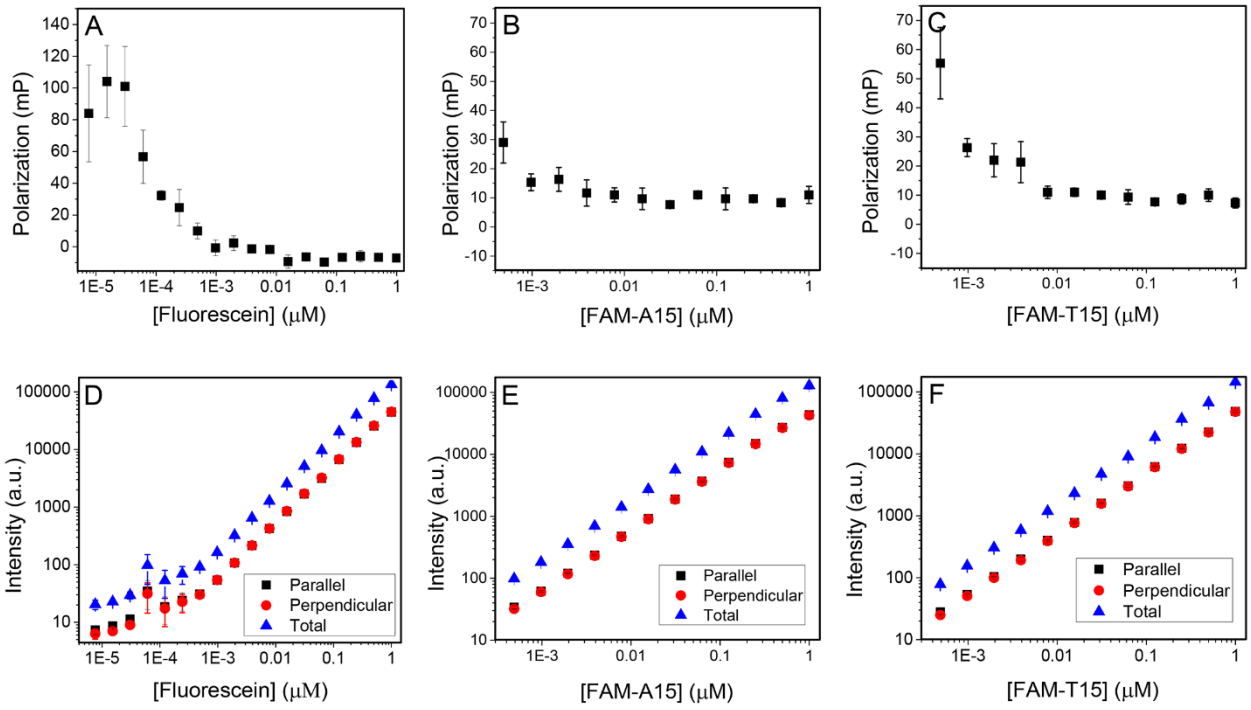

Figure 5.1. Concentration effects on FP for A_{15}, T_{15} and free fluorescein. The effect of dilution on FP for (A) free fluorescein, (B) FAM-A_{15}, and (C) FAM-T_{15}. The effect of dilution on fluorescence intensity for (D) free fluorescein, (E) FAM-A_{15}, and (F) FAM-T_{15}. The total fluorescence and the

perpendicular and parallel intensities used for calculating FP are presented. All measurements were performed in 10 mM HEPES (pH 7.6) buffer with 485 nm excitation and 535 nm emission.

5.3.2 The FP of FAM-labeled DNA is strongly pH-dependent implying FAM/DNA interactions

The above dilution experiments set a basis for our system. Fluorescein is a strongly pH-dependent fluorophore; it is almost non-fluorescent below pH 4.[334] Its highest fluorescent state is the double anion form in basic buffers, and its fluorescence decreases with progressive protonation. By lowering pH from 7.5 to 6.0, the fluorescence of free fluorescein decreased by ~60% (Figure 5.2A, blue curve with the *y*-axis on the right), but its FP remained the same (black curve, *y*-axis on the left). For the same pH drop, the intensity of FAM-A_{15} decreased by 90% (Figure 5.2B), while FAM-T_{15} decreased by 73% (Figure 5.2C). Therefore, the DNA strands led to further fluorescence drops alongside the effects of pH on the fluorophore. For both DNAs, their FP at pH 7.5 was close to 10 mP. At pH 6.0, the FP of FAM-A_{15} and FAM-T_{15} increased to ~40 mP. Since the fluorescence was still strong enough (i.e. >100 units), the increased FP cannot be attributed to the low light artifact. Considering the FP of the free fluorescein did not change much, the increased FP of the DNA samples indicated stronger FAM/DNA interactions, which decreased the tumbling rate of the FAM labels. The three pK_a values of fluorescein are 2.2, 4.4 and 6.7 (Figure 5.2D).[334] At basic pH, fluorescein is in its dianion form with the highest quantum yield and is repelled by the negatively charged DNA backbone. At pH 6.0, a fraction of fluorescein exists as a neutral molecule and may interact with DNA more strongly.

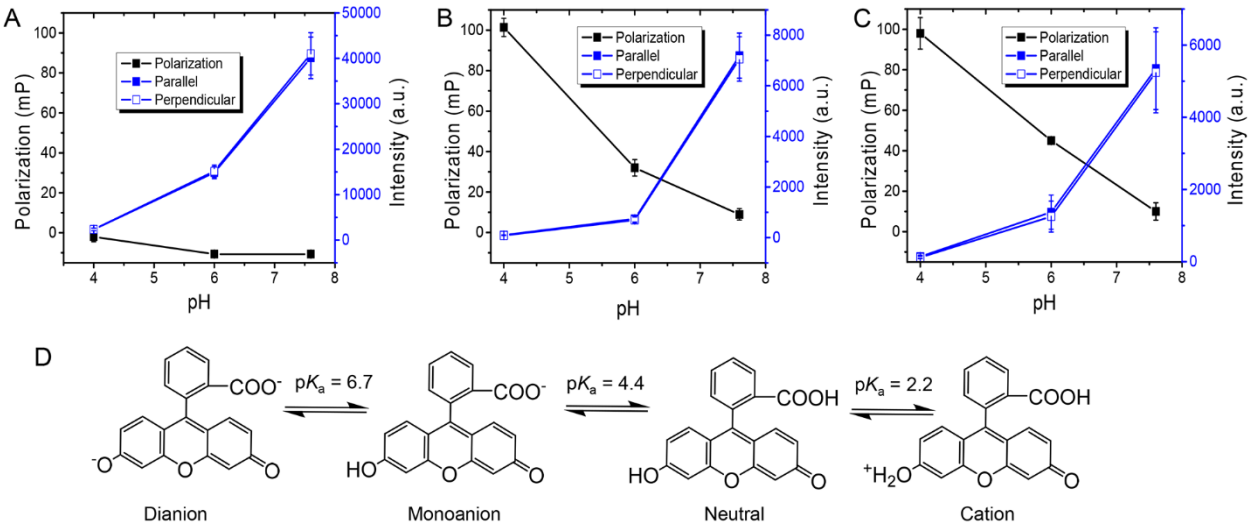

Figure 5.2. pH effects on FP. The effect of pH on FP and fluorescence intensity for (A) free fluorescein, (B) FAM-A_{15}, and (C) FAM-T_{15}. The buffers used were 10 mM acetate (pH 4.0), 10 mM MES (pH 6.0) and 10 mM HEPES (pH 7.6) for adjusting pH. (D) The structure of fluorescein and its protonation.[334]

We then further lowered the pH to 4, and the intensity of the free fluorescein dropped to 2300 units, while that of the two DNA samples were 100 (FAM-A_{15}) and 140 (FAM-T_{15}) respectively. The free fluorescein FP slightly increased to -2 mP, while for the two DNA, both reached ~100 mP. The fluorescence intensities of both DNA samples have approached the low light limit. In addition, further increased FAM/DNA interactions at low pH may also contribute to the increased FP. This trend of increasing polarization with decreasing pH was also seen for FAM-C_{15} and FAM-G_{15} (Figure 5.3).

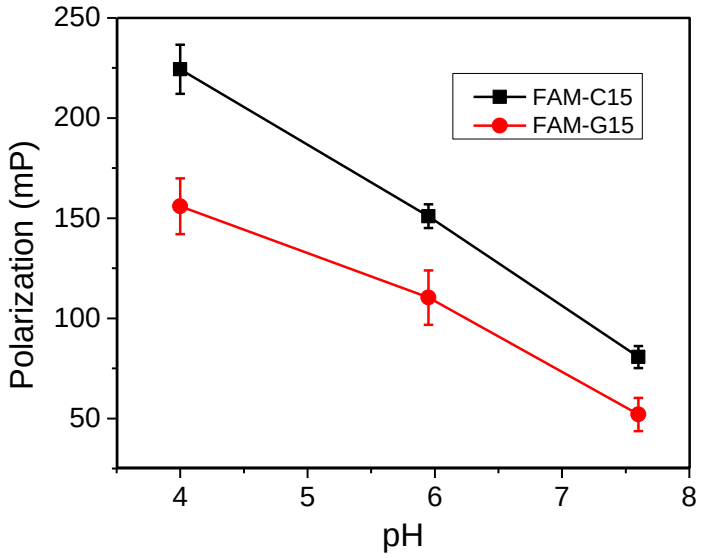

Figure 5.3. Polarization of FAM-C15 and FAM-G15 DNA at different pH. The DNA and buffer concentrations were 20 nM and 10 mM, respectively. Although poly-C DNA may form the i-motif structure at low pH, such folding does not change the molecular weight of the molecule although the volume of the molecule might change slightly. The effect of pH on the interaction between FAM and the DNA backbone is still the main factor.

To further understand this pH effect, we then tested a TYE^{TM} 665 labeled T_{15} DNA, which is much less pH sensitive. From the dilution experiment (Figure 5.4A), it also has good FP consistency at sub-nM concentrations. The pH independency is confirmed in Figure 5.4B (e.g. only 50% drop from pH 7.5 to 4.0), much less drastic compared to FAM. Furthermore, its FP changed very little in this pH range and remained around 0 to 10 mP. Therefore, pH did not change the interaction between the TYE dye and DNA.

We also tested some non-DNA polymers labeled with fluorescein derivatives. Polyethylene glycol (PEG), a non-charged polymer with a molecular weight (MW, 10 000 Da) close to that of a 30-mer DNA, was used. Its initial FP at neutral pH was close to zero (Figure 5.4C), indicating that the PEG chain did not affect the tumbling of the FAM label and motion of FAM was decoupled from the motion of the polymer chain. Even at lower pH, the FP change was very small, also similar to that of free fluorescein. PEG is a very simple polymer that cannot interact strongly with

FAM. Therefore, the observed increase of FP at low pH with DNA was due to the interaction between FAM and the DNA backbone. FAM is a unique fluorophore in this regard due to its pH-dependent multiple protonation reactions, leading to pH-dependent interactions with its covalently linked DNA (a polyanion). FP is also a valuable tool to reveal such interactions.

We finally tested FITC-labeled bovine serum albumin (BSA) which had a much larger FP value of ~140 mP at neutral pH (Figure 5.4D). This was likely due to the large molecular volume of BSA and strong fluorophore/BSA interactions. Interestingly, the FP increased to over 200 mP at pH 4. The isoelectric point of BSA is around pH 4.7,[335,336] and it has a net positive charge at pH 4. Since fluorescein is a mixture of neutral and monoanion form at this pH, it is likely that FAM interacted with the protein quite strongly at pH 4.

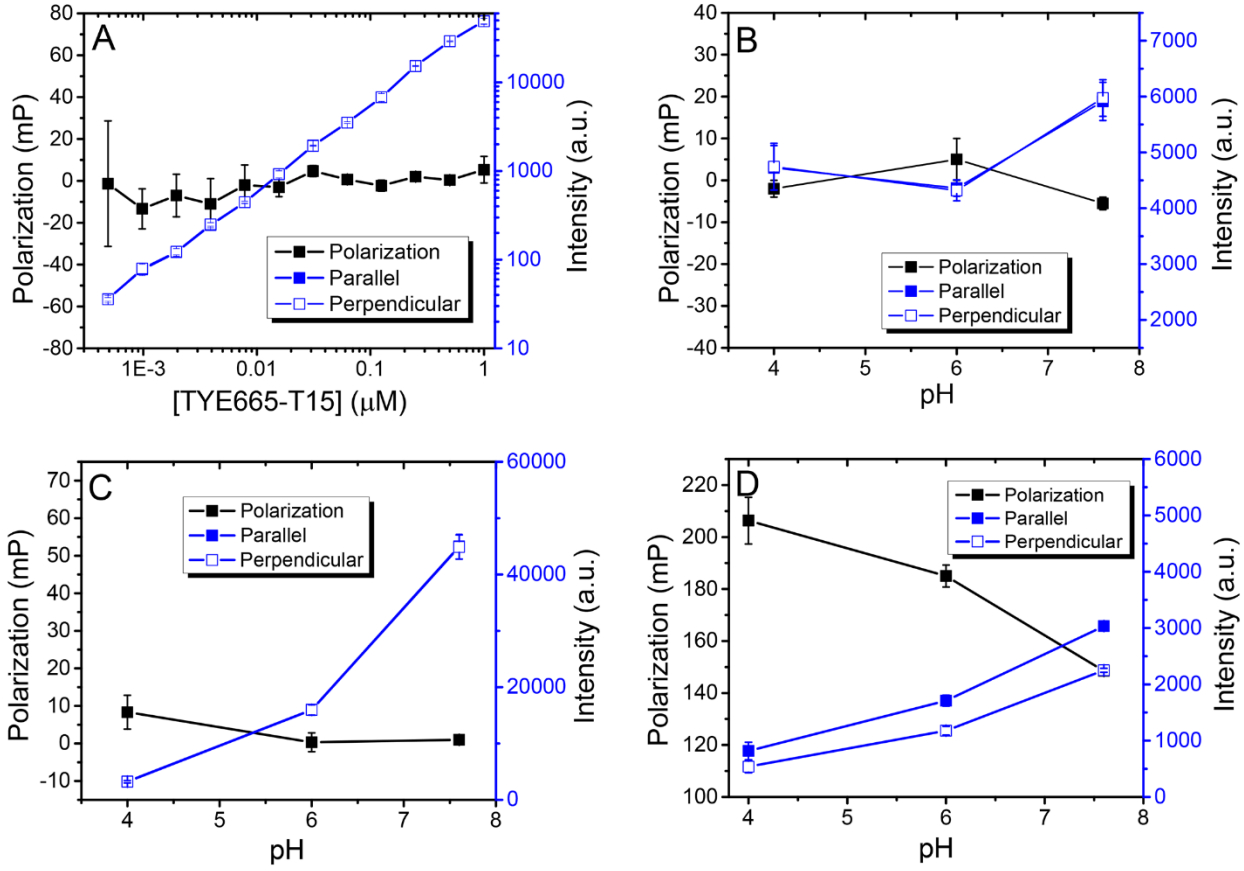

Figure 5.4. Exploring the FP of TYE665-T_{15} and FAM-labelled non-DNA systems at different pH. The effect of (A) dilution and (B) pH on the FP and fluorescence intensity of the less pH-sensitive TYE^{TM} 665 dye labeled T_{15} DNA (final concentration= 100 nM). The effect of pH on the FP and fluorescence intensity of (C) 20 μg/mL FITC-PEG and (D) 1 μg/mL FITC-BSA. The

buffers used to achieve the desired pH were acetate (10 mM, pH 4), MES (10 mM, pH 6), and HEPES (10 mM, pH 7.6).

5.3.3 FP as a function of DNA adsorption efficiency and quenching efficiency

After understanding the basic FP properties of FAM-labeled DNA, we then turned our attention to its adsorption on nanomaterials. FP has been used quite frequently for following adsorption of DNA (and subsequent analytical applications), and the general notion is that adsorption to a nanomaterial can increase the overall molecular volume and thus FP. Many of these nanomaterials, such as GO,[205,337] and gold nanoparticles, are also strong fluorescence quenchers.[323,338] The amount of light emitted from the adsorbed fluorophores would be very low, and what contributes to the FP calculation is mainly the non-adsorbed DNA. Such quenching effect, however, was not considered in most previous work. Herein, we attempted to derive a quantitative relationship between adsorption efficiency, quenching efficiency, and FP (Figure 5.5A). By definition, we can write:

$$P_T = \frac{(F_{II,free} - F_{\perp,free})}{F_{II,free} + F_{\perp,free} + F_{II,adsorbed} + F_{\perp,adsorbed}} + \frac{(F_{II,adsorbed} - F_{\perp,adsorbed})}{F_{II,free} + F_{\perp,free} + F_{II,adsorbed} + F_{\perp,adsorbed}} \quad (Eq.5.1)$$

Where P_T is the measured FP (or total FP), and the 'free' and 'adsorbed' subscripts represent the free and adsorbed species respectively. The denominator can be rewritten as F_T, representing the total fluorescence:

$$P_T = \frac{(F_{II,free} - F_{\perp,free})}{F_T} + \frac{(F_{II,adsorbed} - F_{\perp,adsorbed})}{F_T}$$

$$= \frac{(F_{II,free} - F_{\perp,free})(F_{II,free} + F_{\perp,free})}{F_T(F_{II,free} + F_{\perp,free})} + \frac{(F_{II,adsorbed} - F_{\perp,adsorbed})(F_{II,adsorbed} + F_{\perp,adsorbed})}{F_T(F_{II,adsorbed} + F_{\perp,adsorbed})}$$

$$= \frac{P_{free}(F_{II,free} + F_{\perp,free})}{F_T} + \frac{P_{adsorbed}(F_{II,adsorbed} + F_{\perp,adsorbed})}{F_T}$$

For simplicity, we express F_{ads} and F_{free} as the sum of the parallel and perpendicular components of fluorescence intensity of the adsorbed and free DNA molecule, respectively, and they would be proportional to the total measured fluorescence intensity. Then

$$P_T = \frac{P_{free} * F_{free}}{F_{free} + F_{ads}} + \frac{P_{adsorbed} * F_{ads}}{F_{free} + F_{ads}} \quad (Eq.5.2)$$

We now define θ as adsorption efficiency (i.e. the fraction of DNA adsorbed by nanomaterials). We also define δ as quenching efficiency, and the intensity of fluorescence on the nanomaterials

is only (1-δ) of the same DNA had it not been adsorbed. The fluorescence of the DNA before adding nanomaterials is expressed as F^0_{free}. Therefore, Eq. 5.2 can be written as

$$P_T = \frac{P_{free} * (1-\theta) * F^0_{free}}{(1-\theta) * F^0_{free} + (1-\delta) * \theta * F^0_{free}} + \frac{P_{adsorbed} * (1-\delta) * \theta * F^0_{free}}{(1-\theta) * F^0_{free} + (1-\delta) * \theta * F^0_{free}}$$

$$= P_{free}\frac{(1-\theta)}{1-\theta\delta} + P_{adsorbed}\frac{\theta(1-\delta)}{1-\theta\delta} \qquad (Eq. 5.3)$$

This equation describes the contributions of free DNA and adsorbed DNA to the overall measured FP. The contribution from a quenching surface is decreased by (1-δ). For example, if δ = 0.99, the contribution of adsorbed DNA is decreased 100-fold relative to its free DNA value. In the extreme case of δ = 1 (complete quenching), $P_T = P_{free}$ and adsorbed molecules have zero contribution to the measured FP. In another extreme of δ = 0, $P_T = P_{free}(1-\theta) + P_{adsorbed}\theta$, which is the model used for most binding studies. This equation itself does not consider scattered light. As shown in the above sections, potential scattering effects became important only when the fluorescence was extremely low, and we have determined the limit for such cases. The following sections will use this model to understand experimental results with both quenching and non-quenching materials.

5.3.4 DNA adsorption by Y_2O_3: a non-quenching but strongly adsorbing surface

We first examined DNA adsorption by Y_2O_3 NPs, a metal oxide that is known to not quench FAM fluorescence.[327] Free Y_2O_3 (without added DNA or fluorophores) did not yield much fluorescence, as expected (Figure 5.5B, only ~100 fluorescence units), and the high FP was likely due to scattered light (e.g. the low light artifact). Then, 20 nM FAM-T_{15} was mixed with varying concentrations of Y_2O_3 (Figure 5.5C). The polarization increased with Y_2O_3 concentration, indicating that FAM-T_{15} was adsorbed. In this case, the fluorescence intensity was not affected much by Y_2O_3. We measured the full spectra of FAM-T_{15} adsorbed on different concentrations of Y_2O_3 (Figure 5.5D), and the overall background did not increase, indicating that scattering did not contribute much. Since Y_2O_3 does not quench fluorescence, we determined the adsorption efficiency θ by centrifugation and measurement of the supernatant fluorescence. The fluorescence in the supernatant plateaus at 50 μg/mL Y_2O_3 (Figure 5.5E), where θ was calculated to be 0.95. Since this surface did not affect the FAM fluorescence, δ was 0 for the FAM-T_{15} DNA mixed with

50 µg/mL Y_2O_3. Putting this into Eq. 5.3, $P = 0.05P_{free} + 0.95P_{ads}$ (Table 5.1). Therefore, the main contribution (95%) to the total polarization was from the adsorbed DNA (as would be expected from a low-quenching surface), and its contribution reflected the adsorbed population (95%). By bringing P = 253 mP and P_{free} = 8 mP (from our measurement), we can calculate P_{ads} to be 247 mP. In summary, a non- or low-quenching particle represents the case where an increase in polarization is directly correlated to the adsorption or binding of the fluorophore. Analytically, this corresponds to the binding of the fluorophore by the substrate.

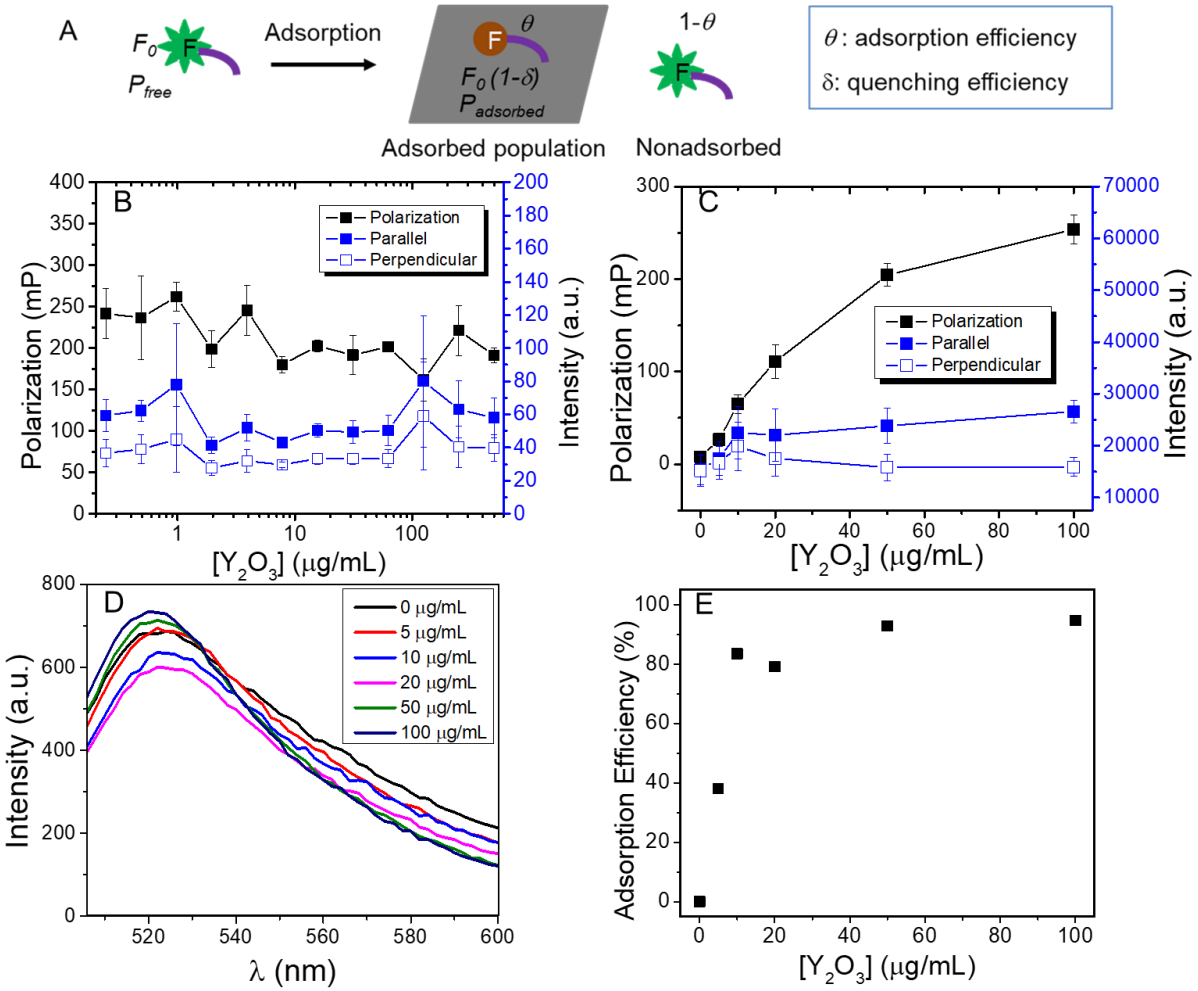

Figure 5.5. Testing the model on a low-quenching surface: Y_2O_3. (A) A scheme showing DNA adsorption efficiency and quenching efficiency, which are two independent parameters. (B) Effect of dilution on polarization and fluorescence intensity of Y_2O_3. Here, the fluorescence intensity was the background without any fluorophores, and it was only around 100 units. (C) Polarization and

fluorescence intensity of 20 nM FAM-T_{15} DNA after the addition of varying concentrations of Y_2O_3. All measurements were performed in 10 mM of pH 7.6 HEPES buffer.

Table 5.1. Determining adsorbed DNA contributions to polarization from the experimentally determined adsorption efficiency: θ and fluorescence quenching efficiency: δ.

	θ	δ	FP	Contribution of adsorbed DNA
Y_2O_3 (50 µg/mL)	95%	0	$=0.05P_{free}+0.95P_{ads}$	95%
GO 10 µg/mL (no salt)	30%	0.97	$=0.93P_{free}+0.07P_{ads}$	7%
GO 10 µg/mL (with salt)	70%	0.97	$=0.98P_{free}+0.02P_{ads}$	2%

5.3.5 DNA adsorption by GO in high salt: a strong quenching and strong adsorbing surface

After understanding non-quenching surfaces, we then studied DNA adsorption by GO, a strongly quenching material.[40,41] This adsorption experiment was first performed with a high salt concentration so that DNA can be efficiently adsorbed.[160,320] By adding increasing concentrations of GO, we observed efficient quenching of FAM-T_{15}, where full fluorescence quenching occurred with just 50 µg/mL of GO. The FP rapidly increased to a value of nearly 200 mP with 500 µg/mL of GO (Figure 5.6A), consistent with literature.[308,309,318,319,339,340]

A closer look at the data calls for a more careful interpretation. For example, with 10 µg/mL of GO, the fluorescence intensity dropped by ~70% (e.g. 70% of the DNA adsorbed), but the FP value only increased from 28 mP to 37 mP. Further increase of GO to 50 µg/mL increased the FP to 120 mP. At this moment, the DNA was fully adsorbed and δ was calculated to be 0.97. Therefore, the change of the FP value does not linearly correlate with DNA adsorption, which was predicted by Eq. 5.3. Further increases in the GO concentration had no effect on DNA fluorescence intensity, but the FP continued to increase, reaching close to 200 mP with 500 µg/mL of GO. This final stage of increase could not correlate with DNA adsorption either. We also saw a similar trend with another strongly quenching surface, CeO_2 (Figure 5.6B).

At a GO concentration of 50 µg/mL, the adsorption saturated and δ was calculated to be 0.97 by comparing the fluorescence intensity at this concentration to that of free DNA (Figure 5.6A).

Applying our model with 10 μg/mL of GO, we found that θ~0.70 (based on fluorescence quenching) and $P = 0.98P_{free} + 0.013P_{ads}$ (Table 5.1). In contrast to Y_2O_3, the adsorbed DNA contributed very little to the total polarization on GO, even at a high coverage.

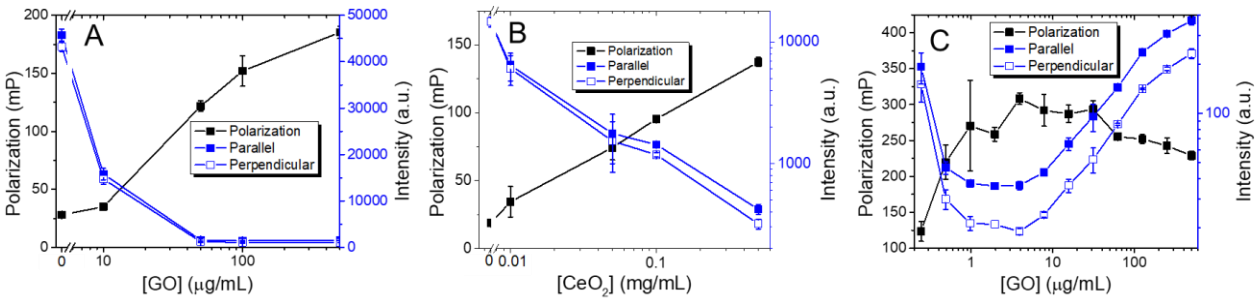

Figure 5.6. Testing the model on strongly quenching surfaces: GO and CeO_2. (A) The adsorption of 20 nM FAM-T_{15} on GO in 10 mM HEPES buffer, pH 7.6 with 300 mM NaCl. (B) Polarization and fluorescence of various concentrations of CeO_2 mixed with 20 nM FAM-T_{15} DNA. All measurements performed in 10 mM HEPES (pH 7.6). (C) Polarization and fluorescence of GO only (no DNA).

5.3.6 Effect of light scattering by nanomaterials

For the last three data points in Figure 5.6A (GO concentration above 50 μg/mL), the fluorescence intensity was around 1000 units, and thus it could not be explained by the low light limit. Nanomaterials may scatter light and sometimes have autofluorescence. To understand this, we measured FP of GO without any DNA. The initial FP value with very dilute GO was still above 100 mP (Figure 5.6C), similar to that of Y_2O_3, which is attributable to the low light artifact. Still, with increased GO concentrations, we observed a similarly high FP, reaching 250 to 300 mP. The GO sample also showed a very weak fluorescence peak at ~540 nm. This fluorescence is well documented in literature,[341] and it is highly polarized, but its contribution to the overall fluorescence is negligible in the presence of other fluorophores. In addition, background scattering emerged with more than 16 μg/mL of GO (Figure 5.7A, see the raised background signal).[333] As such, the autofluorescence and scattered light can contribute to a further increase in FP after full DNA adsorption in Figure 5.6A (with strongly quenched FAM fluorescence).

These two factors complicate interpretation of FP for DNA adsorbed on GO, and data at such high concentrations of GO must be scrutinized carefully. In a more general sense, once a

quenching surface has adsorbed most of the FAM-DNA in solution, polarization will become dominated by scattering events (due to the low light limit) rather than contributions from change in the molecular volume of the DNA (due to immobilization). In analytical applications, therefore, care must be taken when interpreting polarization data for quenching surfaces once a fluorophore is adsorbed. We did not try to include scattering effects in our derivation of the equations in order to keep the discussion simple. This being said, at lower concentrations of GO where the fluorescence of the DNA can dominate scattering events, this effect is negligible. For example, in our study, we mostly used GO at below 50 µg/mL wherein full adsorption of GO could be achieved at this point.

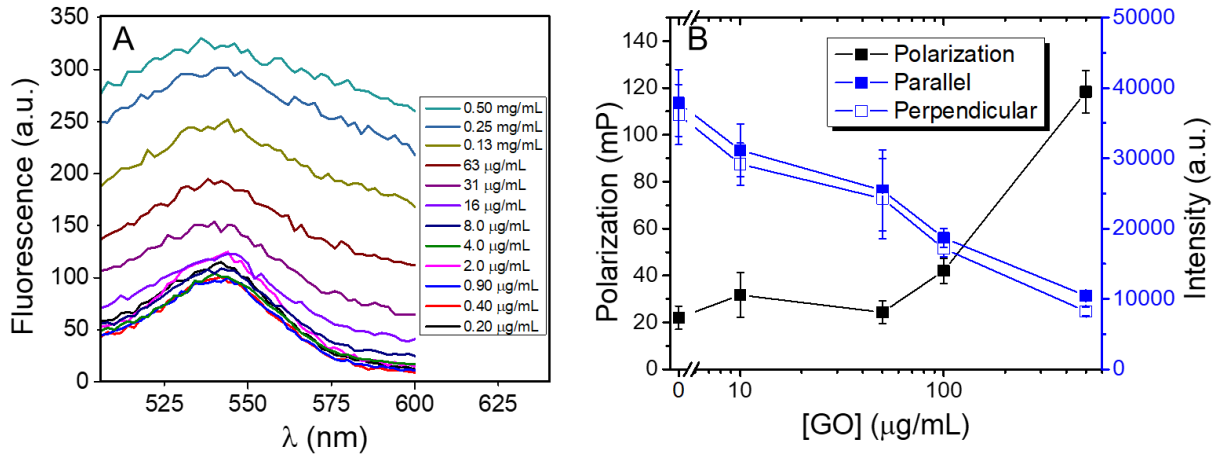

Figure 5.7. Effects of light scattering and low-salt DNA adsorption on GO. (A) Fluorescence spectra of different concentrations of GO. The excitation wavelength was 485 nm, scanning from 505 nm to 600 nm. A broad fluorescence peak was seen, centered on 540 nm and somewhat concentration independent. Increases at higher GO concentrations were likely due to scattering. All measurements performed in 10 mM HEPES (pH 7.6). (B) The adsorption of 20 nM FAM-T_{15} on GO in 10 mM HEPES buffer, pH 7.6 without 300 mM NaCl.

5.3.7 DNA adsorption by GO in low salt: a strong quenching and weak adsorbing surface.

We then repeated the experiment without salt (only 10 mM HEPES buffer, pH 7.6). Under these conditions, GO cannot effectively adsorb DNA (Figure 5.7B, blue traces). Since the surface was the same as that used in the previous section, we still took $\delta = 0.97$. With 50 µg/mL of GO, we see

that the FAM-DNA was 30% quenched (i.e. $\theta \cong 0.30$). At this moment, the FP of the salt-free sample was still about ~20 mP. For a quantitative understanding, we brought the numbers to Eq. 3, and $P = 0.93P_{free} + 0.065P_{ads}$. Thus, the free DNA contribution to the FP was 15 times that of the adsorbed DNA. This is quite similar to the case of high salt, except that there is more free DNA in solution (due to reduced adsorption). Free DNA has a very low polarization compared to adsorbed DNA, and this is reflected in the total polarization.

Therefore, with high salt, there is a reasonable anti-correlation between fluorescence intensity and FP, which might be analytically useful. The reason for the increased FP, however, needs to be carefully analyzed for physical chemistry interpretations. Part of it could be from the remaining free DNA, part of it could be from the adsorbed DNA with partially quenched fluorescence, and part of it could be from light scattering/fluorescence of the added GO nanosheets. In the extreme situation, where the adsorbed fluorophores are fully quenched and no light scattering takes place, one should not observe any change in the FP until adsorption is close to completion and the system reaches the low light threshold.

These examples have covered most representative nanomaterials that can adsorb DNA. For quenching surfaces, the change of FP does not follow a simple linear relationship with adsorption efficiency. For analytical chemists, this is particularly important since interpretation of calibration could result in misunderstandings if such effects are ignored.

5.4 Conclusions

In summary, we have systematically studied the effect of adsorption and fluorescence quenching on FP for FAM-DNA/nanomaterial mixtures. An equation was derived to quantitatively relate these two measurable parameters (adsorption efficiency and quenching efficiency) with FP. To substantiate the application of this equation, we performed a few DNA adsorption experiments to study strongly adsorbing surfaces that either strongly quench fluorescence or do not quench fluorescence. For strongly quenching nanomaterials, adsorbed DNA molecules do not contribute much to the measured total FP. Therefore, care needs to be taken when interpreting such data for related biosensor design and adsorption experiments. In addition, we used FP to study the interaction between fluorophore labels and various polymers. For the FAM label, due to its protonation at low pH, its interaction with poly-A DNA was higher than that with poly-T DNA or

PEG. Increased interaction was reflected from increased FP. Overall, this study supports that FP is a powerful bioanalytical and biophysical tool to understand biopolymers and their interactions with nanomaterials. At the same time, we need to be very careful about data interpretation due to fluorescence quenching property of nanomaterials.

Chapter 6: Concluding Remarks and Future Directions

6.1 Conclusions

Interfacing GO and metal oxide nanoparticles with DNA has shown great promise in the development of fluorescence-based biosensors. In this thesis, I aimed to solve some of the shortcomings of these sensors, as well as provide more fundamental understanding of the processes involved. This ranged from exploring the adsorption mechanism itself to problems with experimental design and interpretation.

In Chapter 2, I explored the role the adsorption mechanism plays in the detection of aptamer targets using fluorescence experiments. Using the adenosine aptamer as a model, its desorption from nanomaterials due to the addition of its targets (adenosine, ATP) and non-targets was studied. It was found that, for GO, its reliance on base stacking and hydrogen bonding (relatively weak interactions) allowed for target binding to be the main driving force for DNA desorption. On the other hand, metal oxide nanoparticles relied on stronger adsorption interactions and only competing ligands can displace DNA from its surface (rather than DNA/target binding).

In Chapter 3, I began my investigation on the enhanced adsorption of poly-C DNA on nanomaterials by first studying the nature of FAM–labeled poly-C (in this case FAM-C_{15}) itself. The fluorescence of the FAM label was strongly quenched at neutral pH in poly C DNA, which was not observed in other DNA homopolymers. The quenched fluorescence was irreversibly recovered by heating, confirming that a DNA secondary structure was responsible for the initial quenching. Using circular dichroism, I saw that the FAM-C_{15} was folded into an i-motif at neutral pH, whereas the non-labeled strand was not, confirming this hypothesis. Furthermore, this unfolded FAM-C_{15} adsorbed even stronger on GO compared to when folded, confirming the i-motif was not responsible for this enhanced adsorption on GO (and indeed, other nanomaterials).

In Chapter 4, I continued experiments with poly-C adsorption on GO in order to determine the reason for its enhanced adsorption. I started by varying the pH and comparing the desorption of either a T_{15} or random 12-mer from GO by the addition of either A_{15}, T_{15}, C_{15} and G_{15}. It was seen that C_{15} only had the highest affinity at neutral pH and higher, while the opposite was true at low pH; its affinity was the lowest. This did not change with arrangement of C within the strand. While these experiments proved what was already known, it did not provide me with an explanation for

the anomalous adsorption of poly-C on GO. Therefore, I collaborated with another student who specialized in molecular dynamics simulations. Here, we found that C_{15} had a maximally extended conformation on GO at neutral pH, with very little intrastrand interactions and many phosphate backbone hydrogen bond contact points with GO. This was compared to A_{15}, which had numerous intrastrand interactions, lower contact points with GO and a less stable adsorption. This was very different at low pH, where poly-C can fold into the i-motif. In this case, C_{15} was highly folded with less contact with GO. On pristine graphene, this picture changed, with π-π stacking the dominating adsorption mechanism. In this case, A_{15} was adsorbed more strongly under the conditions tested. This fundamental understanding delivered by this work provides another framework to design smart DNA biosensors with nanomaterial-dependant adsorption properties.

Finally, in Chapter 5, I conducted experiments using fluorescence polarization with FAM-labelled DNA and nanomaterials. The polarization generally did not vary with DNA concentration, until the detection limit of the instrument. At this point, scattering and other effects artificially increase polarization. Due to this, it was hypothesized that DNA adsorption on quenching surfaces would incorrectly be attributed to adsorption, rather than the low concentration of free DNA. A model was developed accounting for both the quenching effect and the surface coverage, which simplified to a typical binding model for non-quenching surfaces. To test this model, I conducted adsorption polarization experiments with GO (strongly quenching) in high and low salt environments (low and high surface coverage, respectively), as well as Y_2O_3 (a low-quenching surface). In all cases, the calculated polarization from the model accounted for quenching effects accurately, providing another tool for analytical chemists to use while studying these DNA/nanomaterial systems.

Based on the above work, the original contributions I have made to the current understanding of DNA/nanomaterial biosensors can be summarized as follows:

1) Metal oxide nanoparticles adsorb DNA too strongly and can only be displaced by competing ligands, rather than relying on aptamer/target binding
2) FAM can stabilize the formation of the i-motif in many C-rich DNA sequences, even at neutral pH, which should be accounted for in biosensor design
3) Poly-C DNA adsorbs strongly on GO at neutral pH due to flexible phosphate backbone hydrogen bonds, while the formation of the i-motif actually decreases affinity to GO

4) Fluorescence polarization can be used in quenching surfaces for analytical applications, though special care needs to be taken in the interpretations of such results (considering increases due to binding compared to the low fluorescence artifact)

6.2 Future Work

The body of work presented here have answered some fundamental questions related to GO/DNA and oxide/DNA adsorption. In this final section, I provide some avenues for future research based on my findings in this thesis.

Competing nanomaterial/target and target/aptamer interactions were only studied here for GO and a few metal oxide nanoparticles, which adsorb DNA through different mechanisms. Yet, there are still other nanomaterials that adsorb DNA through other means. For example, MoS_2 and WS_2 adsorb DNA through predominantly attractive van der Waals forces.[199] After the work from my group on AuNPs,[111] as well as the work presented here, such a unique interaction for these two materials may present an interesting fourth case for understanding this process.

With regards to poly-C/GO interactions, the explanations provided in Chapter 4 are based on computer simulations, rather than any empirical observation. Although the simulations do model our fluorescence experiments well, to conclusively prove that poly-C is more spread out on GO compared to other DNA strands, an experiment like atomic force microscopy (AFM) could be used to probe the folding once adsorbed on to GO. Such a method has been used to observe DNA arrangements on lipid bilayers,[342] it is therefore plausible that it can be applied here. The main challenge could be the resolution of AFM on DNA oligonucleotides under water.

In addition, labeled-DNA fluorescence polarization experiments can be performed not only with "hard" surfaces like inorganic nanomaterials, but also "soft" surfaces like lipid membranes. The interaction of DNA with cell-like surfaces would likely increase polarization to different degrees depending on the lipid, which would give binding information if it does not quench fluorescence. This increase can provide a simple way to measure the sequence- and length- dependence of DNA adsorption on such membranes (if it occurs).

Finally, the fundamental understandings obtained in this thesis can be used for the design of better biosensors with lower background, lower cost and higher sensitivity. For example, researchers utilizing fluorescence polarization in DNA/nanomaterial sensors can choose non- or low-

quenching nanomaterials so that an accurate appraisal of binding can be obtained. Furthermore, one can exploit the strong binding of poly-C nanomaterials to build di-block DNA sensors on a variety of nanomaterials – a concept already explored by our group for GO.[187] This should not be limited to fluorescence; electrochemical and colorimetric sensors represent a new direction to exploit poly-C anchor-based DNA sensors.

Letters of Copyright Permission

For article used in Chapter 2:

For article used in Chapter 3:

For article used in Chapter 4

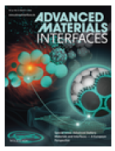

Poly-Cytosine Deoxyribonucleic Acid Strongly Anchoring on Graphene Oxide Due to Flexible Backbone Phosphate Interactions

Author: Juewen Liu, Yu Jia, Shaokang Guan, et al
Publication: Advanced Materials Interfaces
Publisher: John Wiley and Sons
Date: Dec 30, 2020

Order Completed

Thank you for your order.

This Agreement between Anand Lopez ("You") and John Wiley and Sons ("John Wiley and Sons") consists of your license details and the terms and conditions provided by John Wiley and Sons and Copyright Clearance Center.

Your confirmation email will contain your order number for future reference.

License Number	5323170979280
License date	Jun 06, 2022

Printable Details

Licensed Content

Licensed Content Publisher	John Wiley and Sons
Licensed Content Publication	Advanced Materials Interfaces
Licensed Content Title	Poly-Cytosine Deoxyribonucleic Acid Strongly Anchoring on Graphene Oxide Due to Flexible Backbone Phosphate Interactions
Licensed Content Author	Juewen Liu, Yu Jia, Shaokang Guan, et al
Licensed Content Date	Dec 30, 2020
Licensed Content Volume	8
Licensed Content Issue	3
Licensed Content Pages	9

Order Details

Type of use	Dissertation/Thesis
Requestor type	Author of this Wiley article
Format	Print and electronic
Portion	Full article
Will you be translating?	No

About Your Work

Title	Interfacing fluorescent DNA oligonucleotides with graphene oxide and metal oxides: from adsorption to sensing
Institution name	University of Waterloo
Expected presentation date	Aug 2022

Additional Data

For article used in Chapter 5

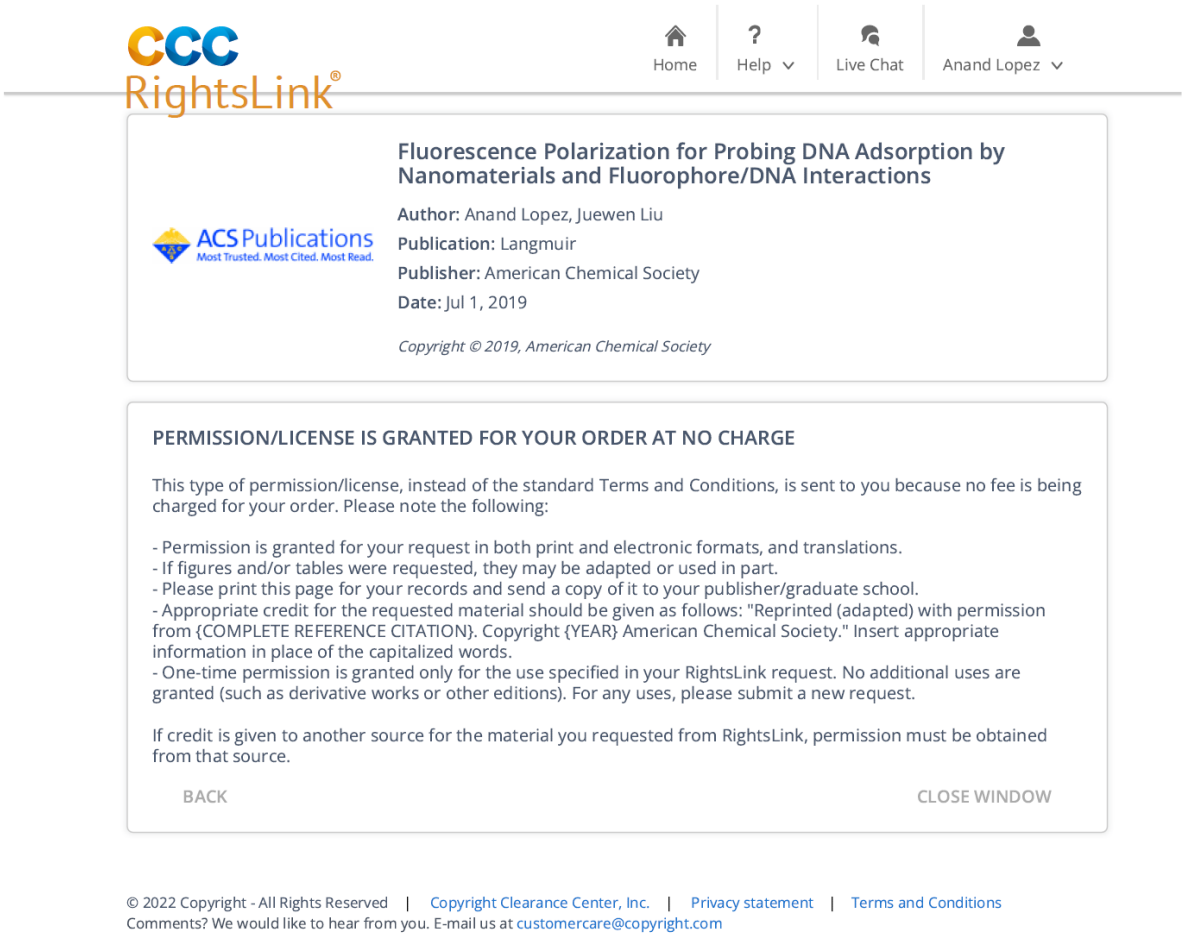

References

(1) Zhou, Q.; Yang, N.; Li, Y.; Ren, B.; Ding, X.; Bian, H.; Yao, X. Total Concentrations and Sources of Heavy Metal Pollution in Global River and Lake Water Bodies from 1972 to 2017. *Glob. Ecol. Conserv.* **2020**, *22*, e00925.

(2) Brown, E. D.; Wright, G. D. New Targets and Screening Approaches in Antimicrobial Drug Discovery. *Chem. Rev.* **2005**, *105* (2), 759–774.

(3) Bridges, A. J. Chemical Inhibitors of Protein Kinases. *Chem. Rev.* **2001**, *101* (8), 2541–2572.

(4) Srinivasarao, M.; Low, P. S. Ligand-Targeted Drug Delivery. *Chem. Rev.* **2017**, *117* (19), 12133–12164.

(5) Ziegler, C.; Göpel, W. Biosensor Development. *Curr. Opin. Chem. Biol.* **1998**, *2* (5), 585–591.

(6) Purohit, B.; Vernekar, P. R.; Shetti, N. P.; Chandra, P. Biosensor Nanoengineering: Design, Operation, and Implementation for Biomolecular Analysis. *Sens. Int.* **2020**, *1*, 100040.

(7) Sassolas, A.; Leca-Bouvier, B. D.; Blum, L. J. DNA Biosensors and Microarrays. *Chem. Rev.* **2008**, *108* (1), 109–139.

(8) Wang, J. SURVEY AND SUMMARY: From DNA Biosensors to Gene Chips. *Nucleic Acids Res.* **2000**, *28* (16), 3011–3016.

(9) Kolahalam, L. A.; Kasi Viswanath, I. V.; Diwakar, B. S.; Govindh, B.; Reddy, V.; Murthy, Y. L. N. Review on Nanomaterials: Synthesis and Applications. *Mater. Today Proc.* **2019**, *18*, 2182–2190.

(10) Baig, N.; Kammakakam, I.; Falath, W. Nanomaterials: A Review of Synthesis Methods, Properties, Recent Progress, and Challenges. *Mater. Adv.* **2021**, *2* (6), 1821–1871.

(11) Roduner, E. Size Matters: Why Nanomaterials Are Different. *Chem. Soc. Rev.* **2006**, *35* (7), 583–592.

(12) Mirkin, C. A.; Letsinger, R. L.; Mucic, R. C.; Storhoff, J. J. A DNA-Based Method for Rationally Assembling Nanoparticles into Macroscopic Materials. *Nature* **1996**, *382* (6592), 607–609.

(13) Liu, J.; Lu, Y. Preparation of Aptamer-Linked Gold Nanoparticle Purple Aggregates for Colorimetric Sensing of Analytes. *Nat. Protoc.* **2006**, *1* (1), 246–252.

(14) Liu, J.; Lu, Y. A Colorimetric Lead Biosensor Using DNAzyme-Directed Assembly of Gold Nanoparticles. *J. Am. Chem. Soc.* **2003**, *125* (22), 6642–6643.

(15) Schroeder, V.; Savagatrup, S.; He, M.; Lin, S.; Swager, T. M. Carbon Nanotube Chemical Sensors. *Chem. Rev.* **2019**, *119* (1), 599–663.

(16) Sun, H.; Ren, J.; Qu, X. Carbon Nanomaterials and DNA: From Molecular Recognition to Applications. *Acc. Chem. Res.* **2016**, *49* (3), 461–470.

(17) Liu, B.; Liu, J. Sensors and Biosensors Based on Metal Oxide Nanomaterials. *TrAC Trends Anal. Chem.* **2019**, *121*, 115690.

(18) Liu, B.; Ma, L.; Huang, Z.; Hu, H.; Wu, P.; Liu, J. Janus DNA Orthogonal Adsorption of Graphene Oxide and Metal Oxide Nanoparticles Enabling Stable Sensing in Serum. *Mater. Horiz.* **2018**, *5* (1), 65–69.

(19) Borst, P. Structure and Function of Mitochondrial DNA. *Trends Biochem. Sci.* **1977**, *2* (2), 31–34.

(20) Oliver, S. G. From DNA Sequence to Biological Function. *Nature* **1996**, *379* (6566), 597–600.
(21) Travers, A.; Muskhelishvili, G. DNA Structure and Function. *FEBS J.* **2015**, *282* (12), 2279–2295.
(22) Thaplyal, P.; Bevilacqua, P. C. Experimental Approaches for Measuring PKa's in RNA and DNA. *Methods Enzymol.* **2014**, *549*, 189–219.
(23) Liu, J. Adsorption of DNA onto Gold Nanoparticles and Graphene Oxide: Surface Science and Applications. *Phys. Chem. Chem. Phys.* **2012**, *14* (30), 10485–10496.
(24) Yakovchuk, P.; Protozanova, E.; Frank-Kamenetskii, M. D. Base-Stacking and Base-Pairing Contributions into Thermal Stability of the DNA Double Helix. *Nucleic Acids Res.* **2006**, *34* (2), 564–574.
(25) Lane, M. J.; Paner, T.; Kashin, I.; Faldasz, B. D.; Li, B.; Gallo, F. J.; Benight, A. S. The Thermodynamic Advantage of DNA Oligonucleotide 'Stacking Hybridization' Reactions: Energetics of a DNA Nick. *Nucleic Acids Res.* **1997**, *25* (3), 611–616.
(26) Tan, Z.-J.; Chen, S.-J. Nucleic Acid Helix Stability: Effects of Salt Concentration, Cation Valence and Size, and Chain Length. *Biophys. J.* **2006**, *90* (4), 1175–1190.
(27) Breslauer, K. J.; Frank, R.; Blöcker, H.; Marky, L. A. Predicting DNA Duplex Stability from the Base Sequence. *Proc. Natl. Acad. Sci.* **1986**, *83* (11), 3746–3750.
(28) Khan, G. S.; Shah, A.; Zia-ur-Rehman; Barker, D. Chemistry of DNA Minor Groove Binding Agents. *J. Photochem. Photobiol. B* **2012**, *115*, 105–118.
(29) Wing, R.; Drew, H.; Takano, T.; Broka, C.; Tanaka, S.; Itakura, K.; Dickerson, R. E. Crystal Structure Analysis of a Complete Turn of B-DNA. *Nature* **1980**, *287* (5784), 755–758.
(30) Peters, J. P.; Maher, L. J. DNA Curvature and Flexibility in Vitro and in Vivo. *Q. Rev. Biophys.* **2010**, *43* (1), 23–63.
(31) Hogan, M.; LeGrange, J.; Austin, B. Dependence of DNA Helix Flexibility on Base Composition. *Nature* **1983**, *304* (5928), 752–754.
(32) Alberti, P.; Mergny, J.-L. DNA Duplex–Quadruplex Exchange as the Basis for a Nanomolecular Machine. *Proc. Natl. Acad. Sci.* **2003**, *100* (4), 1569–1573.
(33) Varshney, D.; Spiegel, J.; Zyner, K.; Tannahill, D.; Balasubramanian, S. The Regulation and Functions of DNA and RNA G-Quadruplexes. *Nat. Rev. Mol. Cell Biol.* **2020**, *21* (8), 459–474.
(34) Bochman, M. L.; Paeschke, K.; Zakian, V. A. DNA Secondary Structures: Stability and Function of G-Quadruplex Structures. *Nat. Rev. Genet.* **2012**, *13* (11), 770–780.
(35) Robinson, J.; Raguseo, F.; Nuccio, S. P.; Liano, D.; Di Antonio, M. DNA G-Quadruplex Structures: More than Simple Roadblocks to Transcription? *Nucleic Acids Res.* **2021**, *49* (15), 8419–8431.
(36) Spiegel, J.; Adhikari, S.; Balasubramanian, S. The Structure and Function of DNA G-Quadruplexes. *Trends Chem.* **2020**, *2* (2), 123–136.
(37) Abou Assi, H.; Garavís, M.; González, C.; Damha, M. J. I-Motif DNA: Structural Features and Significance to Cell Biology. *Nucleic Acids Res.* **2018**, *46* (16), 8038–8056.
(38) Dong, Y.; Yang, Z.; Liu, D. DNA Nanotechnology Based on I-Motif Structures. *Acc. Chem. Res.* **2014**, *47* (6), 1853–1860.
(39) Dvořáková, Z.; Renčiuk, D.; Kejnovská, I.; Školáková, P.; Bednářová, K.; Sagi, J.; Vorlíčková, M. I-Motif of Cytosine-Rich Human Telomere DNA Fragments Containing Natural Base Lesions. *Nucleic Acids Res.* **2018**, *46* (4), 1624–1634.

(40) Pages, B. J.; Gurung, S. P.; McQuaid, K.; Hall, J. P.; Cardin, C. J.; Brazier, J. A. Stabilization of Long-Looped i-Motif DNA by Polypyridyl Ruthenium Complexes. *Front. Chem.* **2019**, *7*.
(41) Day, H. A.; Huguin, C.; Waller, Z. A. E. Silver Cations Fold I-Motif at Neutral PH. *Chem. Commun.* **2013**, *49* (70), 7696–7698.
(42) Gao, J.; Berden, G.; Rodgers, M. T.; Oomens, J. Interaction of Cu+ with Cytosine and Formation of I-Motif-like C–M+–C Complexes: Alkali versus Coinage Metals. *Phys. Chem. Chem. Phys.* **2016**, *18* (10), 7269–7277.
(43) Wright, E. P.; Day, H. A.; Ibrahim, A. M.; Kumar, J.; Boswell, L. J. E.; Huguin, C.; Stevenson, C. E. M.; Pors, K.; Waller, Z. A. E. Mitoxantrone and Analogues Bind and Stabilize I-Motif Forming DNA Sequences. *Sci. Rep.* **2016**, *6* (1), 39456.
(44) Rajendran, A.; Nakano, S.; Sugimoto, N. Molecular Crowding of the Cosolutes Induces an Intramolecular I-Motif Structure of Triplet Repeat DNA Oligomers at Neutral PH. *Chem. Commun.* **2010**, *46* (8), 1299–1301.
(45) Assi, H. A.; Harkness, R. W.; Martin-Pintado, N.; Wilds, C. J.; Campos-Olivas, R.; Mittermaier, A. K.; González, C.; Damha, M. J. Stabilization of I-Motif Structures by 2′-β-Fluorination of DNA. *Nucleic Acids Res.* **2016**, *44* (11), 4998–5009.
(46) Kikuta, K.; Piao, H.; Brazier, J.; Taniguchi, Y.; Onizuka, K.; Nagatsugi, F.; Sasaki, S. Stabilization of the I-Motif Structure by the Intra-Strand Cross-Link Formation. *Bioorg. Med. Chem. Lett.* **2015**, *25* (16), 3307–3310.
(47) Edwards, D. N.; Machwe, A.; Wang, Z.; Orren, D. K. Intramolecular Telomeric G-Quadruplexes Dramatically Inhibit DNA Synthesis by Replicative and Translesion Polymerases, Revealing Their Potential to Lead to Genetic Change. *PLOS ONE* **2014**, *9* (1), e80664.
(48) Gouda, A. S.; Amine, M. S.; Pedersen, E. B. Improved I-Motif Thermal Stability by Insertion of Anthraquinone Monomers. *Org. Biomol. Chem.* **2017**, *15* (31), 6613–6621.
(49) Ellington, A. D.; Szostak, J. W. In Vitro Selection of RNA Molecules That Bind Specific Ligands. *Nature* **1990**, *346* (6287), 818–822.
(50) Ellington, A. D.; Szostak, J. W. Selection in Vitro of Single-Stranded DNA Molecules That Fold into Specific Ligand-Binding Structures. *Nature* **1992**, *355* (6363), 850–852.
(51) Huizenga, D. E.; Szostak, J. W. A DNA Aptamer That Binds Adenosine and ATP. *Biochemistry* **1995**, *34* (2), 656–665.
(52) Zhang, Z.; Oni, O.; Liu, J. New Insights into a Classic Aptamer: Binding Sites, Cooperativity and More Sensitive Adenosine Detection. *Nucleic Acids Res.* **2017**, *45* (13), 7593–7601.
(53) Kruger, K.; Grabowski, P. J.; Zaug, A. J.; Sands, J.; Gottschling, D. E.; Cech, T. R. Self-Splicing RNA: Autoexcision and Autocyclization of the Ribosomal RNA Intervening Sequence of Tetrahymena. *Cell* **1982**, *31* (1), 147–157.
(54) Hutchins, C. J.; Rathjen, P. D.; Forster, A. C.; Symons, R. H. Self-Cleavage of plus and Minus RNA Transcripts of Avocado Sunblotch Viroid. *Nucleic Acids Res.* **1986**, *14* (9), 3627–3640.
(55) Birikh, K. R.; Heaton, P. A.; Eckstein, F. The Structure, Function and Application of the Hammerhead Ribozyme. *Eur. J. Biochem.* **1997**, *245* (1), 1–16.
(56) Doudna, J. A.; Cech, T. R. The Chemical Repertoire of Natural Ribozymes. *Nature* **2002**, *418* (6894), 222–228.

(57) Breaker, R. R.; Joyce, G. F. A DNA Enzyme That Cleaves RNA. *Chem. Biol.* **1994**, *1* (4), 223–229.
(58) Cuenoud, B.; Szostak, J. W. A DNA Metalloenzyme with DNA Ligase Activity. *Nature* **1995**, *375* (6532), 611–614.
(59) Flynn-Charlebois, A.; Wang, Y.; Prior, T. K.; Rashid, I.; Hoadley, K. A.; Coppins, R. L.; Wolf, A. C.; Silverman, S. K. Deoxyribozymes with 2‘−5‘ RNA Ligase Activity. *J. Am. Chem. Soc.* **2003**, *125* (9), 2444–2454.
(60) Purtha, W. E.; Coppins, R. L.; Smalley, M. K.; Silverman, S. K. General Deoxyribozyme-Catalyzed Synthesis of Native 3‘−5‘ RNA Linkages. *J. Am. Chem. Soc.* **2005**, *127* (38), 13124–13125.
(61) Wang, M.; Zhang, H.; Zhang, W.; Zhao, Y.; Yasmeen, A.; Zhou, L.; Yu, X.; Tang, Z. In Vitro Selection of DNA-Cleaving Deoxyribozyme with Site-Specific Thymidine Excision Activity. *Nucleic Acids Res.* **2014**, *42* (14), 9262–9269.
(62) Saran, R.; Kleinke, K.; Zhou, W.; Yu, T.; Liu, J. A Silver-Specific DNAzyme with a New Silver Aptamer and Salt-Promoted Activity. *Biochemistry* **2017**, *56* (14), 1955–1962.
(63) Rothemund, P. W. K. Folding DNA to Create Nanoscale Shapes and Patterns. *Nature* **2006**, *440* (7082), 297–302.
(64) Hong, F.; Zhang, F.; Liu, Y.; Yan, H. DNA Origami: Scaffolds for Creating Higher Order Structures. *Chem. Rev.* **2017**, *117* (20), 12584–12640.
(65) Zhang, Q.; Jiang, Q.; Li, N.; Dai, L.; Liu, Q.; Song, L.; Wang, J.; Li, Y.; Tian, J.; Ding, B.; et al. DNA Origami as an In Vivo Drug Delivery Vehicle for Cancer Therapy. *ACS Nano* **2014**, *8* (7), 6633–6643.
(66) Wang, S.; Zhou, Z.; Ma, N.; Yang, S.; Li, K.; Teng, C.; Ke, Y.; Tian, Y. DNA Origami-Enabled Biosensors. *Sensors* **2020**, *20* (23), 6899.
(67) Hernández-Ainsa, S.; Keyser, U. F. DNA Origami Nanopores: Developments, Challenges and Perspectives. *Nanoscale* **2014**, *6* (23), 14121–14132.
(68) Kuzuya, A.; Komiyama, M. DNA Origami: Fold, Stick, and Beyond. *Nanoscale* **2010**, *2* (3), 309–321.
(69) Naresh, V.; Lee, N. A Review on Biosensors and Recent Development of Nanostructured Materials-Enabled Biosensors. *Sensors* **2021**, *21* (4), 1109.
(70) Bhalla, N.; Jolly, P.; Formisano, N.; Estrela, P. Introduction to Biosensors. *Essays Biochem.* **2016**, *60* (1), 1–8.
(71) Introduction to Fluorescence. In *Principles of Fluorescence Spectroscopy*; Lakowicz, J. R., Ed.; Springer US: Boston, MA, 2006; pp 1–26.
(72) Mineno, T.; Ueno, T.; Urano, Y.; Kojima, H.; Nagano, T. Creation of Superior Carboxyfluorescein Dyes by Blocking Donor-Excited Photoinduced Electron Transfer. *Org. Lett.* **2006**, *8* (26), 5963–5966.
(73) Aschi, M.; D’Archivio, A. A.; Fontana, A.; Formiglio, A. Physicochemical Properties of Fluorescent Probes: Experimental and Computational Determination of the Overlapping PKa Values of Carboxyfluorescein. *J. Org. Chem.* **2008**, *73* (9), 3411–3417.
(74) Kretschy, N.; Sack, M.; Somoza, M. M. Sequence-Dependent Fluorescence of Cy3- and Cy5-Labeled Double-Stranded DNA. *Bioconjug. Chem.* **2016**, *27* (3), 840–848.
(75) Instrumentation for Fluorescence Spectroscopy. In *Principles of Fluorescence Spectroscopy*; Lakowicz, J. R., Ed.; Springer US: Boston, MA, 2006; pp 27–61.
(76) Aswani, K.; Jinadasa, T.; Brown, C. M. Fluorescence Microscopy Light Sources. *Microsc. Today* **2012**, *20* (4), 22–28.

(77) Lakowicz, J. R. Fluorescence Anisotropy. In *Principles of Fluorescence Spectroscopy*; Lakowicz, J. R., Ed.; Springer US: Boston, MA, 1999; pp 291–319.
(78) Dantus, M.; Bowman, R. M.; Zewail, A. H. Femtosecond Laser Observations of Molecular Vibration and Rotation. *Nature* **1990**, *343* (6260), 737–739.
(79) Jameson, D. M.; Ross, J. A. Fluorescence Polarization/Anisotropy in Diagnostics and Imaging. *Chem. Rev.* **2010**, *110* (5), 2685–2708.
(80) Quenching of Fluorescence. In *Principles of Fluorescence Spectroscopy*; Lakowicz, J. R., Ed.; Springer US: Boston, MA, 2006; pp 277–330.
(81) Sahoo, H. Förster Resonance Energy Transfer – A Spectroscopic Nanoruler: Principle and Applications. *J. Photochem. Photobiol. C Photochem. Rev.* **2011**, *12* (1), 20–30.
(82) Zheng, J.; Yang, R.; Shi, M.; Wu, C.; Fang, X.; Li, Y.; Li, J.; Tan, W. Rationally Designed Molecular Beacons for Bioanalytical and Biomedical Applications. *Chem. Soc. Rev.* **2015**, *44* (10), 3036–3055.
(83) Tyagi, S.; Kramer, F. R. Molecular Beacons: Probes That Fluoresce upon Hybridization. *Nat. Biotechnol.* **1996**, *14* (3), 303–308.
(84) Zhang, P.; Beck, T.; Tan, W. Design of a Molecular Beacon DNA Probe with Two Fluorophores. *Angew. Chem.* **2001**, *113* (2), 416–419.
(85) Mao, S.; Ying, Y.; Wu, R.; Chen, A. K. Recent Advances in the Molecular Beacon Technology for Live-Cell Single-Molecule Imaging. *iScience* **2020**, *23* (12), 101801.
(86) Bratu, D. P.; Cha, B.-J.; Mhlanga, M. M.; Kramer, F. R.; Tyagi, S. Visualizing the Distribution and Transport of MRNAs in Living Cells. *Proc. Natl. Acad. Sci.* **2003**, *100* (23), 13308–13313.
(87) Kang, W. J.; Cho, Y. L.; Chae, J. R.; Lee, J. D.; Choi, K.-J.; Kim, S. Molecular Beacon-Based Bioimaging of Multiple MicroRNAs during Myogenesis. *Biomaterials* **2011**, *32* (7), 1915–1922.
(88) Cioni, J.-M.; Lin, J. Q.; Holtermann, A. V.; Koppers, M.; Jakobs, M. A. H.; Azizi, A.; Turner-Bridger, B.; Shigeoka, T.; Franze, K.; Harris, W. A.; et al. Late Endosomes Act as MRNA Translation Platforms and Sustain Mitochondria in Axons. *Cell* **2019**, *176* (1), 56-72.e15.
(89) Oliveira, G. P. de; Zigon, E.; Rogers, G.; Davodian, D.; Lu, S.; Jovanovic-Talisman, T.; Jones, J.; Tigges, J.; Tyagi, S.; Ghiran, I. C. Detection of Extracellular Vesicle RNA Using Molecular Beacons. *iScience* **2020**, *23* (1), 100782.
(90) Santangelo, P. J.; Nix, B.; Tsourkas, A.; Bao, G. Dual FRET Molecular Beacons for MRNA Detection in Living Cells. *Nucleic Acids Res.* **2004**, *32* (6), e57.
(91) Moutsiopoulou, A.; Broyles, D.; Dikici, E.; Daunert, S.; Deo, S. K. Molecular Aptamer Beacons and Their Applications in Imaging and Diagnostics. *Small Weinh. Bergstr. Ger.* **2019**, *15* (35), e1902248.
(92) Li, J. J.; Fang, X.; Tan, W. Molecular Aptamer Beacons for Real-Time Protein Recognition. *Biochem. Biophys. Res. Commun.* **2002**, *292* (1), 31–40.
(93) Kim, B.; Jung, I. H.; Kang, M.; Shim, H.-K.; Woo, H. Y. Cationic Conjugated Polyelectrolytes-Triggered Conformational Change of Molecular Beacon Aptamer for Highly Sensitive and Selective Potassium Ion Detection. *J. Am. Chem. Soc.* **2012**, *134* (6), 3133–3138.
(94) Hamaguchi, N.; Ellington, A.; Stanton, M. Aptamer Beacons for the Direct Detection of Proteins. *Anal. Biochem.* **2001**, *294* (2), 126–131.

(95) Zhang, X.-B.; Wang, Z.; Xing, H.; Xiang, Y.; Lu, Y. Catalytic and Molecular Beacons for Amplified Detection of Metal Ions and Organic Molecules with High Sensitivity. *Anal. Chem.* **2010**, *82* (12), 5005–5011.
(96) Li, J.; Lu, Y. A Highly Sensitive and Selective Catalytic DNA Biosensor for Lead Ions. *J. Am. Chem. Soc.* **2000**, *122* (42), 10466–10467.
(97) Liu, J.; Lu, Y. A DNAzyme Catalytic Beacon Sensor for Paramagnetic Cu2+ Ions in Aqueous Solution with High Sensitivity and Selectivity. *J. Am. Chem. Soc.* **2007**, *129* (32), 9838–9839.
(98) Liu, J.; Lu, Y. Improving Fluorescent DNAzyme Biosensors by Combining Inter- and Intramolecular Quenchers. *Anal. Chem.* **2003**, *75* (23), 6666–6672.
(99) Torabi, S.-F.; Wu, P.; McGhee, C. E.; Chen, L.; Hwang, K.; Zheng, N.; Cheng, J.; Lu, Y. In Vitro Selection of a Sodium-Specific DNAzyme and Its Application in Intracellular Sensing. *Proc. Natl. Acad. Sci.* **2015**, *112* (19), 5903–5908.
(100) Moon, W. J.; Yang, Y.; Liu, J. Zn2+-Dependent DNAzymes: From Solution Chemistry to Analytical, Materials and Therapeutic Applications. *ChemBioChem* **2021**, *22* (5), 779–789.
(101) Ren, W.; Jimmy Huang, P.-J.; de Rochambeau, D.; Moon, W. J.; Zhang, J.; Lyu, M.; Wang, S.; Sleiman, H.; Liu, J. Selection of a Metal Ligand Modified DNAzyme for Detecting Ni2+. *Biosens. Bioelectron.* **2020**, *165*, 112285.
(102) Zhou, W.; Zhang, Y.; Huang, P.-J. J.; Ding, J.; Liu, J. A DNAzyme Requiring Two Different Metal Ions at Two Distinct Sites. *Nucleic Acids Res.* **2016**, *44* (1), 354–363.
(103) Hong, X.; Huang, H.; Chen, M.; Liu, F.; Li, N. A Fluorescence Anisotropy Study of the DNA Hybridization Reaction Mediated by Formation of the C–Ag+–C Structure. *Anal. Methods* **2016**, *8* (15), 3156–3162.
(104) Rinken, A.; Lavogina, D.; Kopanchuk, S. Assays with Detection of Fluorescence Anisotropy: Challenges and Possibilities for Characterizing Ligand Binding to GPCRs. *Trends Pharmacol. Sci.* **2018**, *39* (2), 187–199.
(105) Li, Y.; Zhao, Q. Aptamer Structure Switch Fluorescence Anisotropy Assay for Small Molecules Using Streptavidin as an Effective Signal Amplifier Based on Proximity Effect. *Anal. Chem.* **2019**, *91* (11), 7379–7384.
(106) Gokulrangan, G.; Unruh, J. R.; Holub, D. F.; Ingram, B.; Johnson, C. K.; Wilson, G. S. DNA Aptamer-Based Bioanalysis of IgE by Fluorescence Anisotropy. *Anal. Chem.* **2005**, *77* (7), 1963–1970.
(107) Li, Y.; Yu, H.; Zhao, Q. Aptamer Fluorescence Anisotropy Assays for Detection of Aflatoxin B1 and Adenosine Triphosphate Using Antibody to Amplify Signal Change. *RSC Adv.* **2022**, *12* (12), 7464–7468.
(108) Zhao, Q.; Tao, J.; Uppal, J. S.; Peng, H.; Wang, H.; Le, X. C. Nucleic Acid Aptamers Improving Fluorescence Anisotropy and Fluorescence Polarization Assays for Small Molecules. *TrAC Trends Anal. Chem.* **2019**, *110*, 401–409.
(109) Liu, Y.; Zhao, Q. Direct Fluorescence Anisotropy Assay for Cocaine Using Tetramethylrhodamine-Labeled Aptamer. *Anal. Bioanal. Chem.* **2017**, *409* (16), 3993–4000.
(110) Yagub, M. T.; Sen, T. K.; Afroze, S.; Ang, H. M. Dye and Its Removal from Aqueous Solution by Adsorption: A Review. *Adv. Colloid Interface Sci.* **2014**, *209*, 172–184.

(111) Zhang, F.; Wang, S.; Liu, J. Gold Nanoparticles Adsorb DNA and Aptamer Probes Too Strongly and a Comparison with Graphene Oxide for Biosensing. *Anal. Chem.* **2019**, *91* (22), 14743–14750.
(112) Liu, Z.; Chen, S.; Liu, B.; Wu, J.; Zhou, Y.; He, L.; Ding, J.; Liu, J. Intracellular Detection of ATP Using an Aptamer Beacon Covalently Linked to Graphene Oxide Resisting Nonspecific Probe Displacement. *Anal. Chem.* **2014**, *86* (24), 12229–12235.
(113) Liu, B.; Salgado, S.; Maheshwari, V.; Liu, J. DNA Adsorbed on Graphene and Graphene Oxide: Fundamental Interactions, Desorption and Applications. *Curr. Opin. Colloid Interface Sci.* **2016**, *26*, 41–49.
(114) Lopez, A.; Liu, J. Covalent and Noncovalent Functionalization of Graphene Oxide with DNA for Smart Sensing. *Adv. Intell. Syst. n/a* (n/a), 2000123.
(115) Choi, W.; Lahiri, I.; Seelaboyina, R.; Kang, Y. S. Synthesis of Graphene and Its Applications: A Review. *Crit. Rev. Solid State Mater. Sci.* **2010**, *35* (1), 52–71.
(116) Allen, M. J.; Tung, V. C.; Kaner, R. B. Honeycomb Carbon: A Review of Graphene. *Chem. Rev.* **2010**, *110* (1), 132–145.
(117) Chen, D.; Feng, H.; Li, J. Graphene Oxide: Preparation, Functionalization, and Electrochemical Applications. *Chem. Rev.* **2012**, *112* (11), 6027–6053.
(118) Smith, A. T.; LaChance, A. M.; Zeng, S.; Liu, B.; Sun, L. Synthesis, Properties, and Applications of Graphene Oxide/Reduced Graphene Oxide and Their Nanocomposites. *Nano Mater. Sci.* **2019**, *1* (1), 31–47.
(119) Zaaba, N. I.; Foo, K. L.; Hashim, U.; Tan, S. J.; Liu, W.-W.; Voon, C. H. Synthesis of Graphene Oxide Using Modified Hummers Method: Solvent Influence. *Procedia Eng.* **2017**, *184*, 469–477.
(120) Ramesha, G. K.; Vijaya Kumara, A.; Muralidhara, H. B.; Sampath, S. Graphene and Graphene Oxide as Effective Adsorbents toward Anionic and Cationic Dyes. *J. Colloid Interface Sci.* **2011**, *361* (1), 270–277.
(121) Liu, J.; Xue, Y.; Dai, L. Sulfated Graphene Oxide as a Hole-Extraction Layer in High-Performance Polymer Solar Cells. *J. Phys. Chem. Lett.* **2012**, *3* (14), 1928–1933.
(122) Ma, Y.; Gao, W.; Zhang, Z.; Zhang, S.; Tian, Z.; Liu, Y.; Ho, J. C.; Qu, Y. Regulating the Surface of Nanoceria and Its Applications in Heterogeneous Catalysis. *Surf. Sci. Rep.* **2018**, *73* (1), 1–36.
(123) Montini, T.; Melchionna, M.; Monai, M.; Fornasiero, P. Fundamentals and Catalytic Applications of CeO2-Based Materials. *Chem. Rev.* **2016**, *116* (10), 5987–6041.
(124) Dhall, A.; Self, W. Cerium Oxide Nanoparticles: A Brief Review of Their Synthesis Methods and Biomedical Applications. *Antioxidants* **2018**, *7* (8), 97.
(125) Xu, C.; Qu, X. Cerium Oxide Nanoparticle: A Remarkably Versatile Rare Earth Nanomaterial for Biological Applications. *NPG Asia Mater.* **2014**, *6* (3), e90.
(126) Liu, B.; Huang, Z.; Liu, J. Boosting the Oxidase Mimicking Activity of Nanoceria by Fluoride Capping: Rivaling Protein Enzymes and Ultrasensitive F− Detection. *Nanoscale* **2016**, *8* (28), 13562–13567.
(127) Ali, A.; Zafar, H.; Zia, M.; Haq, I. ul; Phull, A. R.; Ali, J. S.; Hussain, A. Synthesis, Characterization, Applications, and Challenges of Iron Oxide Nanoparticles. *Nanotechnol. Sci. Appl.* **2016**, *9*, 49.
(128) Wu, W.; He, Q.; Jiang, C. Magnetic Iron Oxide Nanoparticles: Synthesis and Surface Functionalization Strategies. *Nanoscale Res. Lett.* **2008**, *3* (11), 397–415.

(129) Stankic, S.; Suman, S.; Haque, F.; Vidic, J. Pure and Multi Metal Oxide Nanoparticles: Synthesis, Antibacterial and Cytotoxic Properties. *J. Nanobiotechnology* **2016**, *14* (1), 73.
(130) LaGrow, A. P.; Besenhard, M. O.; Hodzic, A.; Sergides, A.; Bogart, L. K.; Gavriilidis, A.; Thanh, N. T. K. Unravelling the Growth Mechanism of the Co-Precipitation of Iron Oxide Nanoparticles with the Aid of Synchrotron X-Ray Diffraction in Solution. *Nanoscale* **2019**, *11* (14), 6620–6628.
(131) Zhao, Y.; Li, H.; Wang, Y.; Wang, Y.; Huang, Z.; Su, H.; Liu, J. CeO2 Nanoparticle Transformation to Nanorods and Nanoflowers in Acids with Boosted Oxidative Catalytic Activity. *ACS Appl. Nano Mater.* **2021**, *4* (2), 2098–2107.
(132) Devan, R. S.; Patil, R. A.; Lin, J.-H.; Ma, Y.-R. One-Dimensional Metal-Oxide Nanostructures: Recent Developments in Synthesis, Characterization, and Applications. *Adv. Funct. Mater.* **2012**, *22* (16), 3326–3370.
(133) Liu, B.; Liu, J. Comprehensive Screen of Metal Oxide Nanoparticles for DNA Adsorption, Fluorescence Quenching, and Anion Discrimination. *ACS Appl. Mater. Interfaces* **2015**, *7* (44), 24833–24838.
(134) Fréchette, J.; Vanderlick, T. K. Double Layer Forces over Large Potential Ranges as Measured in an Electrochemical Surface Forces Apparatus. *Langmuir* **2001**, *17* (24), 7620–7627.
(135) Walker, D. A.; Kowalczyk, B.; Cruz, M. O. de la; Grzybowski, B. A. Electrostatics at the Nanoscale. *Nanoscale* **2011**, *3* (4), 1316–1344.
(136) Zareei, M.; Yoozbashizadeh, H.; Madaah Hosseini, H. R. Investigating the Effects of PH, Surfactant and Ionic Strength on the Stability of Alumina/Water Nanofluids Using DLVO Theory. *J. Therm. Anal. Calorim.* **2019**, *135* (2), 1185–1196.
(137) Vladilo, G.; Hassanali, A. Hydrogen Bonds and Life in the Universe. *Life* **2018**, *8* (1), 1.
(138) Wagner, J. P.; Schreiner, P. R. London Dispersion in Molecular Chemistry—Reconsidering Steric Effects. *Angew. Chem. Int. Ed.* **2015**, *54* (42), 12274–12296.
(139) Zhang, J.; Zeng, H. Intermolecular and Surface Interactions in Engineering Processes. *Engineering* **2021**, *7* (1), 63–83.
(140) Leckband, D.; Israelachvili, J. Intermolecular Forces in Biology. *Q. Rev. Biophys.* **2001**, *34* (2), 105–267.
(141) Wu, X.; Ge, X.; Wang, D.; Tang, H. Distinct Mechanisms of Particle Aggregation Induced by Alum and PACl: Floc Structure and DLVO Evaluation. *Colloids Surf. Physicochem. Eng. Asp.* **2009**, *347* (1), 56–63.
(142) Boström, M.; Williams, D. R. M.; Ninham, B. W. Specific Ion Effects: Why DLVO Theory Fails for Biology and Colloid Systems. *Phys. Rev. Lett.* **2001**, *87* (16), 168103.
(143) Grasso*, D.; Subramaniam, K.; Butkus, M.; Strevett, K.; Bergendahl, J. A Review of Non-DLVO Interactions in Environmental Colloidal Systems. *Rev. Environ. Sci. Biotechnol.* **2002**, *1* (1), 17–38.
(144) Zhao, Y.; Li, J.; Gu, H.; Wei, D.; Xu, Y.; Fu, W.; Yu, Z. Conformational Preferences of π–π Stacking Between Ligand and Protein, Analysis Derived from Crystal Structure Data Geometric Preference of π–π Interaction. *Interdiscip. Sci. Comput. Life Sci.* **2015**, *7* (3), 211–220.
(145) Herschlag, D.; Pinney, M. M. Hydrogen Bonds: Simple after All? *Biochemistry* **2018**, *57* (24), 3338–3352.
(146) Grabowski, S. J. What Is the Covalency of Hydrogen Bonding? *Chem. Rev.* **2011**, *111* (4), 2597–2625.

(147) Chen, T.; Li, M.; Liu, J. π–π Stacking Interaction: A Nondestructive and Facile Means in Material Engineering for Bioapplications. *Cryst. Growth Des.* **2018**, *18* (5), 2765–2783.
(148) Grimme, S. Do Special Noncovalent π–π Stacking Interactions Really Exist? *Angew. Chem. Int. Ed.* **2008**, *47* (18), 3430–3434.
(149) Martinez, C. R.; Iverson, B. L. Rethinking the Term "Pi-Stacking." *Chem. Sci.* **2012**, *3* (7), 2191–2201.
(150) Lu, C.; Huang, P.-J. J.; Liu, B.; Ying, Y.; Liu, J. Comparison of Graphene Oxide and Reduced Graphene Oxide for DNA Adsorption and Sensing. *Langmuir* **2016**, *32* (41), 10776–10783.
(151) Kushalkar, M. P.; Liu, B.; Liu, J. Promoting DNA Adsorption by Acids and Polyvalent Cations: Beyond Charge Screening. *Langmuir* **2020**, *36* (38), 11183–11195.
(152) Zeng, S.; Chen, L.; Wang, Y.; Chen, J. Exploration on the Mechanism of DNA Adsorption on Graphene and Graphene Oxide via Molecular Simulations. *J. Phys. Appl. Phys.* **2015**, *48* (27), 275402.
(153) Antony, J.; Grimme, S. Structures and Interaction Energies of Stacked Graphene–Nucleobase Complexes. *Phys. Chem. Chem. Phys.* **2008**, *10* (19), 2722–2729.
(154) Varghese, N.; Mogera, U.; Govindaraj, A.; Das, A.; Maiti, P. K.; Sood, A. K.; Rao, C. N. R. Binding of DNA Nucleobases and Nucleosides with Graphene. *ChemPhysChem* **2009**, *10* (1), 206–210.
(155) Xu, Z.; Lei, X.; Tu, Y.; Tan, Z.-J.; Song, B.; Fang, H. Dynamic Cooperation of Hydrogen Binding and π Stacking in SsDNA Adsorption on Graphene Oxide. *Chem. Weinh. Bergstr. Ger.* **2017**, *23* (53), 13100–13104.
(156) Liu, B.; Zhao, Y.; Jia, Y.; Liu, J. Heating Drives DNA to Hydrophobic Regions While Freezing Drives DNA to Hydrophilic Regions of Graphene Oxide for Highly Robust Biosensors. *J. Am. Chem. Soc.* **2020**, *142* (34), 14702–14709.
(157) He, S.; Song, B.; Li, D.; Zhu, C.; Qi, W.; Wen, Y.; Wang, L.; Song, S.; Fang, H.; Fan, C. A Graphene Nanoprobe for Rapid, Sensitive, and Multicolor Fluorescent DNA Analysis. *Adv. Funct. Mater.* **2010**, *20* (3), 453–459.
(158) Pautler, R.; Kelly, E. Y.; Huang, P.-J. J.; Cao, J.; Liu, B.; Liu, J. Attaching DNA to Nanoceria: Regulating Oxidase Activity and Fluorescence Quenching. *ACS Appl. Mater. Interfaces* **2013**, *5* (15), 6820–6825.
(159) Liu, B.; Liu, J. DNA Adsorption by Magnetic Iron Oxide Nanoparticles and Its Application for Arsenate Detection. *Chem. Commun.* **2014**, *50* (62), 8568–8570.
(160) Wu, M.; Kempaiah, R.; Huang, P.-J. J.; Maheshwari, V.; Liu, J. Adsorption and Desorption of DNA on Graphene Oxide Studied by Fluorescently Labeled Oligonucleotides. *Langmuir* **2011**, *27* (6), 2731–2738.
(161) Liu, B.; Sun, Z.; Zhang, X.; Liu, J. Mechanisms of DNA Sensing on Graphene Oxide. *Anal. Chem.* **2013**, *85* (16), 7987–7993.
(162) Chinnappan, R.; AlAmer, S.; Eissa, S.; Rahamn, A. A.; Abu Salah, K. M.; Zourob, M. Fluorometric Graphene Oxide-Based Detection of Salmonella Enteritis Using a Truncated DNA Aptamer. *Microchim. Acta* **2017**, *185* (1), 61.
(163) Liang, L.; Su, M.; Li, L.; Lan, F.; Yang, G.; Ge, S.; Yu, J.; Song, X. Aptamer-Based Fluorescent and Visual Biosensor for Multiplexed Monitoring of Cancer Cells in Microfluidic Paper-Based Analytical Devices. *Sens. Actuators B Chem.* **2016**, *229*, 347–354.

(164) Xia, N.; Wang, X.; Liu, L. A Graphene Oxide-Based Fluorescent Method for the Detection of Human Chorionic Gonadotropin. *Sensors* **2016**, *16* (10), 1699.
(165) Fang, B.-Y.; Yao, M.-H.; Wang, C.-Y.; Wang, C.-Y.; Zhao, Y.-D.; Chen, F. Detection of Adenosine Triphosphate in HeLa Cell Using Capillary Electrophoresis-Laser Induced Fluorescence Detection Based on Aptamer and Graphene Oxide. *Colloids Surf. B Biointerfaces* **2016**, *140*, 233–238.
(166) Mao, Y.; Chen, Y.; Li, S.; Lin, S.; Jiang, Y. A Graphene-Based Biosensing Platform Based on Regulated Release of an Aptameric DNA Biosensor. *Sensors* **2015**, *15* (11), 28244–28256.
(167) Cheng, X.; Cen, Y.; Xu, G.; Wei, F.; Shi, M.; Xu, X.; Sohail, M.; Hu, Q. Aptamer Based Fluorometric Determination of ATP by Exploiting the FRET between Carbon Dots and Graphene Oxide. *Microchim. Acta* **2018**, *185* (2), 144.
(168) Lu, Z.; Chen, X.; Wang, Y.; Zheng, X.; Li, C. M. Aptamer Based Fluorescence Recovery Assay for Aflatoxin B1 Using a Quencher System Composed of Quantum Dots and Graphene Oxide. *Microchim. Acta* **2015**, *182* (3), 571–578.
(169) Fang, B.-Y.; Wang, C.-Y.; Li, C.; Wang, H.-B.; Zhao, Y.-D. Amplified Using DNase I and Aptamer/Graphene Oxide for Sensing Prostate Specific Antigen in Human Serum. *Sens. Actuators B Chem.* **2017**, *244*, 928–933.
(170) Zhu, Y.; Cai, Y.; Xu, L.; Zheng, L.; Wang, L.; Qi, B.; Xu, C. Building An Aptamer/Graphene Oxide FRET Biosensor for One-Step Detection of Bisphenol A. *ACS Appl. Mater. Interfaces* **2015**, *7* (14), 7492–7496.
(171) Tomita, S.; Ishihara, S.; Kurita, R. A Multi-Fluorescent DNA/Graphene Oxide Conjugate Sensor for Signature-Based Protein Discrimination. *Sensors* **2017**, *17* (10), 2194.
(172) Tan, X.; Chen, T.; Xiong, X.; Mao, Y.; Zhu, G.; Yasun, E.; Li, C.; Zhu, Z.; Tan, W. Semiquantification of ATP in Live Cells Using Nonspecific Desorption of DNA from Graphene Oxide as the Internal Reference. *Anal. Chem.* **2012**, *84* (20), 8622–8627.
(173) Liu, B.; Huang, P.-J. J.; Kelly, E. Y.; Liu, J. Graphene Oxide Surface Blocking Agents Can Increase the DNA Biosensor Sensitivity. *Biotechnol. J.* **2016**, *11* (6), 780–787.
(174) Hata, Y.; Sawada, T.; Serizawa, T. Confined Reduced Graphene Oxides as a Platform for DNA Sensing in Solutions Crowded with Biomolecules. *ACS Appl. Bio Mater.* **2020**, *3* (5), 3210–3216.
(175) He, S.; Song, B.; Li, D.; Zhu, C.; Qi, W.; Wen, Y.; Wang, L.; Song, S.; Fang, H.; Fan, C. A Graphene Nanoprobe for Rapid, Sensitive, and Multicolor Fluorescent DNA Analysis. *Adv. Funct. Mater.* **2010**, *20* (3), 453–459.
(176) Yun, W.; Wu, H.; Liu, X.; Fu, M.; Jiang, J.; Du, Y.; Yang, L.; Huang, Y. Simultaneous Fluorescent Detection of Multiple Metal Ions Based on the DNAzymes and Graphene Oxide. *Anal. Chim. Acta* **2017**, *986*, 115–121.
(177) Zhen, S. J.; Yu, Y.; Li, C. M.; Huang, C. Z. Graphene Oxide Amplified Fluorescence Anisotropy for Label-Free Detection of Potassium Ion. *Analyst* **2014**, *140* (1), 353–357.
(178) Guo, H.; Li, J.; Li, Y.; Wu, D.; Ma, H.; Wei, Q.; Du, B. A Turn-on Fluorescent Sensor for Hg2+ Detection Based on Graphene Oxide and DNA Aptamers. *New J. Chem.* **2018**, *42* (13), 11147–11152.
(179) Liu, Z.; Luo, D.; Ren, F.; Ran, F.; Chen, W.; Zhang, B.; Wang, C.; Chen, H.; Wei, J.; Chen, Q. Ultrasensitive Fluorescent Aptasensor for CRP Detection Based on the RNase H Assisted DNA Recycling Signal Amplification Strategy. *RSC Adv.* **2019**, *9* (21), 11960–11967.

(180) Zhang, Y.; Wu, Q.; Wei, X.; Zhang, J.; Mo, S. DNA Aptamer for Use in a Fluorescent Assay for the Shrimp Allergen Tropomyosin. *Microchim. Acta* **2017**, *184* (2), 633–639.
(181) Tang, L.; Wang, Y.; Liu, Y.; Li, J. DNA-Directed Self-Assembly of Graphene Oxide with Applications to Ultrasensitive Oligonucleotide Assay. *ACS Nano* **2011**, *5* (5), 3817–3822.
(182) Wang, J.; Zhang, L.; Lu, L.; Kang, T. Molecular Beacon Immobilized on Graphene Oxide for Enzyme-Free Signal Amplification in Electrochemiluminescent Determination of MicroRNA. *Microchim. Acta* **2019**, *186* (3), 142.
(183) Xiao, X.; Tao, J.; Zhang, H. Z.; Huang, C. Z.; Zhen, S. J. Exonuclease III-Assisted Graphene Oxide Amplified Fluorescence Anisotropy Strategy for Ricin Detection. *Biosens. Bioelectron.* **2016**, *85*, 822–827.
(184) Xiao, X.; Li, Y. F.; Huang, C. Z.; Zhen, S. J. A Novel Graphene Oxide Amplified Fluorescence Anisotropy Assay with Improved Accuracy and Sensitivity. *Chem. Commun.* **2015**, *51* (89), 16080–16083.
(185) Zhen, S. J.; Xiao, X.; Li, C. H.; Huang, C. Z. An Enzyme-Free DNA Circuit-Assisted Graphene Oxide Enhanced Fluorescence Anisotropy Assay for MicroRNA Detection with Improved Sensitivity and Selectivity. *Anal. Chem.* **2017**, *89* (17), 8766–8771.
(186) Lu, C.; Huang, Z.; Liu, B.; Liu, Y.; Ying, Y.; Liu, J. Poly-Cytosine DNA as a High-Affinity Ligand for Inorganic Nanomaterials. *Angew. Chem. Int. Ed.* **2017**, *56* (22), 6208–6212.
(187) Huang, Z.; Liu, J. Length-Dependent Diblock DNA with Poly-Cytosine (Poly-C) as High-Affinity Anchors on Graphene Oxide. *Langmuir ACS J. Surf. Colloids* **2018**, *34* (3), 1171–1177.
(188) Wang, X.; Lopez, A.; Liu, J. Adsorption of Phosphate and Polyphosphate on Nanoceria Probed by DNA Oligonucleotides. *Langmuir* **2018**, *34* (26), 7899–7905.
(189) Yu, T.; Liu, B.; Liu, J. Adsorption of Selenite and Selenate by Metal Oxides Studied with Fluorescent DNA Probes for Analytical Application. *J. Anal. Test.* **2017**, *1* (1), 2.
(190) Lopez, A.; Zhang, Y.; Liu, J. Tuning DNA Adsorption Affinity and Density on Metal Oxide and Phosphate for Improved Arsenate Detection. *J. Colloid Interface Sci.* **2017**, *493*, 249–256.
(191) Li, F.; Pei, H.; Wang, L.; Lu, J.; Gao, J.; Jiang, B.; Zhao, X.; Fan, C. Nanomaterial-Based Fluorescent DNA Analysis: A Comparative Study of the Quenching Effects of Graphene Oxide, Carbon Nanotubes, and Gold Nanoparticles. *Adv. Funct. Mater.* **2013**, *23* (33), 4140–4148.
(192) Lu, C.-H.; Yang, H.-H.; Zhu, C.-L.; Chen, X.; Chen, G.-N. A Graphene Platform for Sensing Biomolecules. *Angew. Chem. Int. Ed.* **2009**, *48* (26), 4785–4787.
(193) Liu, M.; Chang, D.; Li, Y. Discovery and Biosensing Applications of Diverse RNA-Cleaving DNAzymes. *Acc. Chem. Res.* **2017**, *50* (9), 2273–2283.
(194) Fluorescence Sensing. In *Principles of Fluorescence Spectroscopy*; Lakowicz, J. R., Ed.; Springer US: Boston, MA, 2006; pp 623–673.
(195) Wang, Q.; Wang, W.; Lei, J.; Xu, N.; Gao, F.; Ju, H. Fluorescence Quenching of Carbon Nitride Nanosheet through Its Interaction with DNA for Versatile Fluorescence Sensing. *Anal. Chem.* **2013**, *85* (24), 12182–12188.
(196) Liang, H.; Zhang, X.-B.; Lv, Y.; Gong, L.; Wang, R.; Zhu, X.; Yang, R.; Tan, W. Functional DNA-Containing Nanomaterials: Cellular Applications in Biosensing, Imaging, and Targeted Therapy. *Acc. Chem. Res.* **2014**, *47* (6), 1891–1901.
(197) Zhong, W. Nanomaterials in Fluorescence-Based Biosensing. *Anal. Bioanal. Chem.* **2009**, *394* (1), 47–59.

(198) Meng, Y.; Liu, P.; Zhou, W.; Ding, J.; Liu, J. Bioorthogonal DNA Adsorption on Polydopamine Nanoparticles Mediated by Metal Coordination for Highly Robust Sensing in Serum and Living Cells. *ACS Nano* **2018**, *12* (9), 9070–9080.
(199) Lu, C.; Liu, Y.; Ying, Y.; Liu, J. Comparison of MoS2, WS2, and Graphene Oxide for DNA Adsorption and Sensing. *Langmuir* **2017**, *33* (2), 630–637.
(200) Park, J. S.; Goo, N.-I.; Kim, D.-E. Mechanism of DNA Adsorption and Desorption on Graphene Oxide. *Langmuir* **2014**, *30* (42), 12587–12595.
(201) Li, Y.; Liu, J. Aptamer-Based Strategies for Recognizing Adenine, Adenosine, ATP and Related Compounds. *Analyst* **2020**.
(202) Zhang, F.; Liu, J. Label-Free Colorimetric Biosensors Based on Aptamers and Gold Nanoparticles: A Critical Review. *Anal. Sens. n/a* (n/a).
(203) Jeng, E. S.; Moll, A. E.; Roy, A. C.; Gastala, J. B.; Strano, M. S. Detection of DNA Hybridization Using the Near-Infrared Band-Gap Fluorescence of Single-Walled Carbon Nanotubes. *Nano Lett.* **2006**, *6* (3), 371–375.
(204) Gao, L.; Lian, C.; Zhou, Y.; Yan, L.; Li, Q.; Zhang, C.; Chen, L.; Chen, K. Graphene Oxide–DNA Based Sensors. *Biosens. Bioelectron.* **2014**, *60*, 22–29.
(205) Huang, P.-J. J.; Liu, J. DNA-Length-Dependent Fluorescence Signaling on Graphene Oxide Surface. *Small* **2012**, *8* (7), 977–983.
(206) Zhang, Z.; Liu, J. An Engineered One-Site Aptamer with Higher Sensitivity for Label-Free Detection of Adenosine on Graphene Oxide. *Can. J. Chem.* **2018**.
(207) Liu, B.; Sun, Z.; Huang, P.-J. J.; Liu, J. Hydrogen Peroxide Displacing DNA from Nanoceria: Mechanism and Detection of Glucose in Serum. *J. Am. Chem. Soc.* **2015**, *137* (3), 1290–1295.
(208) Wang, X.; Liu, B.; Liu, J. DNA-Functionalized Nanoceria for Probing Oxidation of Phosphorus Compounds. *Langmuir* **2018**, *34* (51), 15871–15877.
(209) Li, S.; Zhao, X.; Yu, X.; Wan, Y.; Yin, M.; Zhang, W.; Cao, B.; Wang, H. Fe3O4 Nanozymes with Aptamer-Tuned Catalysis for Selective Colorimetric Analysis of ATP in Blood. *Anal. Chem.* **2019**, *91* (22), 14737–14742.
(210) Wu, J.; Wang, X.; Wang, Q.; Lou, Z.; Li, S.; Zhu, Y.; Qin, L.; Wei, H. Nanomaterials with Enzyme-like Characteristics (Nanozymes): Next-Generation Artificial Enzymes (II). *Chem. Soc. Rev.* **2019**, *48* (4), 1004–1076.
(211) Huang, Y.; Ren, J.; Qu, X. Nanozymes: Classification, Catalytic Mechanisms, Activity Regulation, and Applications. *Chem. Rev.* **2019**, *119* (6), 4357–4412.
(212) Li, Y.; Liu, J. Nanozyme's Catching up: Activity, Specificity, Reaction Conditions and Reaction Types. *Mater. Horiz.* **2020**.
(213) Bülbül, G.; Hayat, A.; Andreescu, S. SsDNA-Functionalized Nanoceria: A Redox-Active Aptaswitch for Biomolecular Recognition. *Adv. Healthc. Mater.* **2016**, *5* (7), 822–828.
(214) Zhang, F.; Huang, P.-J. J.; Liu, J. Sensing Adenosine and ATP by Aptamers and Gold Nanoparticles: Opposite Trends of Color Change from Domination of Target Adsorption Instead of Aptamer Binding. *ACS Sens.* **2020**, *5* (9), 2885–2893.
(215) Zhao, Y.; Wang, Y.; Mathur, A.; Wang, Y.; Maheshwari, V.; Su, H.; Liu, J. Fluoride-Capped Nanoceria as a Highly Efficient Oxidase-Mimicking Nanozyme: Inhibiting Product Adsorption and Increasing Oxygen Vacancies. *Nanoscale* **2019**, *11* (38), 17841–17850.

(216) Li, F.; Hu, X.; Wang, F.; Zheng, B.; Du, J.; Xiao, D. A Fluorescent "on-off-on" Probe for Sensitive Detection of ATP Based on ATP Displacing DNA from Nanoceria. *Talanta* **2018**, *179*, 285–291.
(217) Herne, T. M.; Tarlov, M. J. Characterization of DNA Probes Immobilized on Gold Surfaces. *J. Am. Chem. Soc.* **1997**, *119* (38), 8916–8920.
(218) Wang, Y.; Li, Z.; Hu, D.; Lin, C.-T.; Li, J.; Lin, Y. Aptamer/Graphene Oxide Nanocomplex for in Situ Molecular Probing in Living Cells. *J. Am. Chem. Soc.* **2010**, *132* (27), 9274–9276.
(219) Mukherjee, S.; Meshik, X.; Choi, M.; Farid, S.; Datta, D.; Lan, Y.; Poduri, S.; Sarkar, K.; Baterdene, U.; Huang, C.; et al. A Graphene and Aptamer Based Liquid Gated FET-Like Electrochemical Biosensor to Detect Adenosine Triphosphate. *IEEE Trans. NanoBioscience* **2015**, *14* (8), 967–972.
(220) Datta, D.; Meshik, X.; Mukherjee, S.; Sarkar, K.; Choi, M. S.; Mazouchi, M.; Farid, S.; Wang, Y. Y.; Burke, P. J.; Dutta, M.; et al. Submillimolar Detection of Adenosine Monophosphate Using Graphene-Based Electrochemical Aptasensor. *IEEE Trans. Nanotechnol.* **2017**, *16* (2), 196–202.
(221) Yu, J.; Yang, L.; Liang, X.; Dong, T.; Liu, H. Bare Magnetic Nanoparticles as Fluorescence Quenchers for Detection of Thrombin. *Analyst* **2015**, *140* (12), 4114–4120.
(222) Song, C.; Wang, G.-Y.; Kong, D.-M. A Facile Fluorescence Method for Versatile Biomolecular Detection Based on Pristine α-Fe2O3 Nanoparticle-Induced Fluorescence Quenching. *Biosens. Bioelectron.* **2015**, *68*, 239–244.
(223) Chinen, A. B.; Guan, C. M.; Ferrer, J. R.; Barnaby, S. N.; Merkel, T. J.; Mirkin, C. A. Nanoparticle Probes for the Detection of Cancer Biomarkers, Cells, and Tissues by Fluorescence. *Chem. Rev.* **2015**, *115* (19), 10530–10574.
(224) Liu, J.; Cao, Z.; Lu, Y. Functional Nucleic Acid Sensors. *Chem. Rev.* **2009**, *109* (5), 1948–1998.
(225) Song, S.; Qin, Y.; He, Y.; Huang, Q.; Fan, C.; Chen, H.-Y. Functional Nanoprobes for Ultrasensitive Detection of Biomolecules. *Chem. Soc. Rev.* **2010**, *39* (11), 4234–4243.
(226) Wilner, O. I.; Willner, I. Functionalized DNA Nanostructures. *Chem. Rev.* **2012**, *112* (4), 2528–2556.
(227) Liu, B.; Liu, J. Interface Driven Hybrid Materials Based on DNA-Functionalized Gold Nanoparticles. *Matter In Press*.
(228) Zhang, L.; Lu, Z.; Zhao, Q.; Huang, J.; Shen, H.; Zhang, Z. Enhanced Chemotherapy Efficacy by Sequential Delivery of SiRNA and Anticancer Drugs Using PEI-Grafted Graphene Oxide. *Small* **2011**, *7* (4), 460–464.
(229) Ding, Y.; Jiang, Z.; Saha, K.; Kim, C. S.; Kim, S. T.; Landis, R. F.; Rotello, V. M. Gold Nanoparticles for Nucleic Acid Delivery. *Mol. Ther.* **2014**, *22* (6), 1075–1083.
(230) Feng, L.; Zhang, S.; Liu, Z. Graphene Based Gene Transfection. *Nanoscale* **2011**, *3* (3), 1252–1257.
(231) Lu, C.-H.; Willner, B.; Willner, I. DNA Nanotechnology: From Sensing and DNA Machines to Drug-Delivery Systems. *ACS Nano* **2013**, *7* (10), 8320–8332.
(232) Jones, M. R.; Seeman, N. C.; Mirkin, C. A. Programmable Materials and the Nature of the DNA Bond. *Science* **2015**, *347* (6224), 1260901.
(233) Tan, L. H.; Xing, H.; Lu, Y. DNA as a Powerful Tool for Morphology Control, Spatial Positioning, and Dynamic Assembly of Nanoparticles. *Acc. Chem. Res.* **2014**, *47* (6), 1881–1890.

(234) Li, H.; Zhang, Y.; Luo, Y.; Sun, X. Nano-C60: A Novel, Effective, Fluorescent Sensing Platform for Biomolecular Detection. *Small* **2011**, *7* (11), 1562–1568.
(235) Zhu, C.; Zeng, Z.; Li, H.; Li, F.; Fan, C.; Zhang, H. Single-Layer MoS2-Based Nanoprobes for Homogeneous Detection of Biomolecules. *J. Am. Chem. Soc.* **2013**, *135* (16), 5998–6001.
(236) Zhou, Y.; Huang, Z.; Yang, R.; Liu, J. Selection and Screening of DNA Aptamers for Inorganic Nanomaterials. *Chem. Weinh. Bergstr. Ger.* **2018**, *24* (11), 2525–2532.
(237) He, Y.; Lopez, A.; Zhang, Z.; Chen, D.; Yang, R.; Liu, J. Nucleotide and DNA Coordinated Lanthanides: From Fundamentals to Applications. *Coord. Chem. Rev.* **2019**, *387*, 235–248.
(238) Ranganathan, S. V.; Halvorsen, K.; Myers, C. A.; Robertson, N. M.; Yigit, M. V.; Chen, A. A. Complex Thermodynamic Behavior of Single-Stranded Nucleic Acid Adsorption to Graphene Surfaces. *Langmuir* **2016**, *32* (24), 6028–6034.
(239) Kimura-Suda, H.; Petrovykh, D. Y.; Tarlov, M. J.; Whitman, L. J. Base-Dependent Competitive Adsorption of Single-Stranded DNA on Gold. *J. Am. Chem. Soc.* **2003**, *125* (30), 9014–9015.
(240) Storhoff, J. J.; Elghanian, R.; Mirkin, C. A.; Letsinger, R. L. Sequence-Dependent Stability of DNA-Modified Gold Nanoparticles. *Langmuir* **2002**, *18* (17), 6666–6670.
(241) Pei, H.; Li, F.; Wan, Y.; Wei, M.; Liu, H.; Su, Y.; Chen, N.; Huang, Q.; Fan, C. Designed Diblock Oligonucleotide for the Synthesis of Spatially Isolated and Highly Hybridizable Functionalization of DNA–Gold Nanoparticle Nanoconjugates. *J. Am. Chem. Soc.* **2012**, *134* (29), 11876–11879.
(242) Liu, B.; Wu, P.; Huang, Z.; Ma, L.; Liu, J. Bromide as a Robust Backfiller on Gold for Precise Control of Dna Conformation and High Stability of Spherical Nucleic Acids. *J. Am. Chem. Soc.* **2018**, *140* (13), 4499–4502.
(243) Yao, G.; Pei, H.; Li, J.; Zhao, Y.; Zhu, D.; Zhang, Y.; Lin, Y.; Huang, Q.; Fan, C. Clicking DNA to Gold Nanoparticles: Poly-Adenine-Mediated Formation of Monovalent DNA-Gold Nanoparticle Conjugates with Nearly Quantitative Yield. *NPG Asia Mater.* **2015**, *7* (1), e159.
(244) Xu, L.; Zhang, P.; Liu, Y.; Fang, X.; Zhang, Z.; Liu, Y.; Peng, L.; Liu, J. Continuously Tunable Nucleotide/Lanthanide Coordination Nanoparticles for DNA Adsorption and Sensing. *ACS Omega* **2018**, *3* (8), 9043–9051.
(245) Wang, L.; Zhang, Z.; Liu, B.; Liu, Y.; Lopez, A.; Wu, J.; Liu, J. Interfacing DNA Oligonucleotides with Calcium Phosphate and Other Metal Phosphates. *Langmuir* **2018**, *34* (49), 14975–14982.
(246) Liu, D.; Balasubramanian, S. A Proton-Fuelled DNA Nanomachine. *Angew. Chem. Int. Ed.* **2003**, *42* (46), 5734–5736.
(247) Lupták, A.; Ferré-D'Amaré, A. R.; Zhou, K.; Zilm, K. W.; Doudna, J. A. Direct PKa Measurement of the Active-Site Cytosine in a Genomic Hepatitis Delta Virus Ribozyme. *J. Am. Chem. Soc.* **2001**, *123* (35), 8447–8452.
(248) Asensio, J. L.; Lane, A. N.; Dhesi, J.; Bergqvist, S.; Brown, T. The Contribution of Cytosine Protonation to the Stability of Parallel DNA Triple Helices. *J. Mol. Biol.* **1998**, *275* (5), 811–822.
(249) Zhou, J.; Wei, C.; Jia, G.; Wang, X.; Feng, Z.; Li, C. Formation of I-Motif Structure at Neutral and Slightly Alkaline PH. *Mol. Biosyst.* **2010**, *6* (3), 580–586.
(250) Sun, D.; Hurley, L. H. The Importance of Negative Superhelicity in Inducing the Formation of G-Quadruplex and i-Motif Structures in the c-Myc Promoter: Implications

for Drug Targeting and Control of Gene Expression. *J. Med. Chem.* **2009**, *52* (9), 2863–2874.
(251) Cui, J.; Waltman, P.; Le, V. H.; Lewis, E. A. The Effect of Molecular Crowding on the Stability of Human C-MYC Promoter Sequence I-Motif at Neutral PH. *Molecules* **2013**, *18* (10), 12751–12767.
(252) Wright, E. P.; Huppert, J. L.; Waller, Z. A. E. Identification of Multiple Genomic DNA Sequences Which Form I-Motif Structures at Neutral PH. *Nucleic Acids Res.* **2017**, *45* (6), 2951–2959.
(253) Peng, Y.; Wang, X.; Xiao, Y.; Feng, L.; Zhao, C.; Ren, J.; Qu, X. I-Motif Quadruplex DNA-Based Biosensor for Distinguishing Single- and Multiwalled Carbon Nanotubes. *J. Am. Chem. Soc.* **2009**, *131* (38), 13813–13818.
(254) Li, X.; Peng, Y.; Ren, J.; Qu, X. Carboxyl-Modified Single-Walled Carbon Nanotubes Selectively Induce Human Telomeric i-Motif Formation. *Proc. Natl. Acad. Sci. U. S. A.* **2006**, *103* (52), 19658–19663.
(255) Jin, K. S.; Shin, S. R.; Ahn, B.; Jin, S.; Rho, Y.; Kim, H.; Kim, S. J.; Ree, M. Effect of C60 Fullerene on the Duplex Formation of I-Motif DNA with Complementary DNA in Solution. *J. Phys. Chem. B* **2010**, *114* (14), 4783–4788.
(256) Chen, X.; Zhou, X.; Han, T.; Wu, J.; Zhang, J.; Guo, S. Stabilization and Induction of Oligonucleotide I-Motif Structure via Graphene Quantum Dots. *ACS Nano* **2013**, *7* (1), 531–537.
(257) Shao, C.; Liang, J.; He, S.; Luan, T.; Yu, J.; Zhao, H.; Xu, J.; Tian, L. PH-Responsive Graphene Oxide–DNA Nanosystem for Live Cell Imaging and Detection. *Anal. Chem.* **2017**, *89* (10), 5445–5452.
(258) Lavis, L. D.; Rutkoski, T. J.; Raines, R. T. Tuning the PKa of Fluorescein to Optimize Binding Assays. *Anal. Chem.* **2007**, *79* (17), 6775–6782.
(259) Torimura, M.; Kurata, S.; Yamada, K.; Yokomaku, T.; Kamagata, Y.; Kanagawa, T.; Kurane, R. Fluorescence-Quenching Phenomenon by Photoinduced Electron Transfer between a Fluorescent Dye and a Nucleotide Base. *Anal. Sci.* **2001**, *17* (1), 155–160.
(260) Mao, H.; Luo, G.; Zhan, Y.; Zhang, J.; Yao, S.; Yu, Y. The Mechanism and Regularity of Quenching the Effect of Bases on Fluorophores: The Base-Quenched Probe Method. *Analyst* **2018**, *143* (14), 3292–3301.
(261) Fleming, A. M.; Ding, Y.; Rogers, R. A.; Zhu, J.; Zhu, J.; Burton, A. D.; Carlisle, C. B.; Burrows, C. J. 4n–1 Is a "Sweet Spot" in DNA i-Motif Folding of 2′-Deoxycytidine Homopolymers. *J. Am. Chem. Soc.* **2017**, *139* (13), 4682–4689.
(262) Schubert, S.; Gül, D. C.; Grunert, H.-P.; Zeichhardt, H.; Erdmann, V. A.; Kurreck, J. RNA Cleaving '10-23' DNAzymes with Enhanced Stability and Activity. *Nucleic Acids Res.* **2003**, *31* (20), 5982–5992.
(263) Samanta, D.; Ebrahimi, S. B.; Mirkin, C. A. Nucleic-Acid Structures as Intracellular Probes for Live Cells. *Adv. Mater.* **2020**, *32* (13), 1901743.
(264) Lake, R. J.; Yang, Z.; Zhang, J.; Lu, Y. DNAzymes as Activity-Based Sensors for Metal Ions: Recent Applications, Demonstrated Advantages, Current Challenges, and Future Directions. *Acc. Chem. Res.* **2019**, *52* (12), 3275–3286.
(265) Hu, Q.; Li, H.; Wang, L.; Gu, H.; Fan, C. DNA Nanotechnology-Enabled Drug Delivery Systems. *Chem. Rev.* **2019**, *119* (10), 6459–6506.
(266) Kahn, J. S.; Hu, Y.; Willner, I. Stimuli-Responsive DNA-Based Hydrogels: From Basic Principles to Applications. *Acc. Chem. Res.* **2017**, *50* (4), 680–690.

(267) Li, L.; Xu, S.; Yan, H.; Li, X.; Yazd, H. S.; Li, X.; Huang, T.; Cui, C.; Jiang, J.; Tan, W. Nucleic Acid Aptamers for Molecular Diagnostics and Therapeutics: Advances and Perspectives. *Angew. Chem. Int. Ed. n/a* (n/a).
(268) Zhou, W.; Saran, R.; Liu, J. Metal Sensing by DNA. *Chem. Rev.* **2017**, *117* (12), 8272–8325.
(269) Zhou, Y.; Tang, L.; Zeng, G.; Zhang, C.; Zhang, Y.; Xie, X. Current Progress in Biosensors for Heavy Metal Ions Based on DNAzymes/DNA Molecules Functionalized Nanostructures: A Review. *Sens. Actuators B Chem.* **2016**, *223*, 280–294.
(270) Tan, W.; Fang, X.; Li, J.; Liu, X. Molecular Beacons: A Novel DNA Probe for Nucleic Acid and Protein Studies. *Chem. – Eur. J.* **2000**, *6* (7), 1107–1111.
(271) Mo, L.; Li, J.; Liu, Q.; Qiu, L.; Tan, W. Nucleic Acid-Functionalized Transition Metal Nanosheets for Biosensing Applications. *Biosens. Bioelectron.* **2017**, *89*, 201–211.
(272) Chen, W.-H.; Yu, X.; Liao, W.-C.; Sohn, Y. S.; Cecconello, A.; Kozell, A.; Nechushtai, R.; Willner, I. ATP-Responsive Aptamer-Based Metal–Organic Framework Nanoparticles (NMOFs) for the Controlled Release of Loads and Drugs. *Adv. Funct. Mater.* **2017**, *27* (37), 1702102.
(273) Wang, W.; Satyavolu, N. S. R.; Wu, Z.; Zhang, J.-R.; Zhu, J.-J.; Lu, Y. Near-Infrared Photothermally Activated DNAzyme–Gold Nanoshells for Imaging Metal Ions in Living Cells. *Angew. Chem. Int. Ed.* **2017**, *56* (24), 6798–6802.
(274) Saha, K.; Agasti, S. S.; Kim, C.; Li, X.; Rotello, V. M. Gold Nanoparticles in Chemical and Biological Sensing. *Chem. Rev.* **2012**, *112* (5), 2739–2779.
(275) Ebrahimi, S. B.; Samanta, D.; Mirkin, C. A. DNA-Based Nanostructures for Live-Cell Analysis. *J. Am. Chem. Soc.* **2020**, *142* (26), 11343–11356.
(276) Yao, G.; Li, J.; Li, Q.; Chen, X.; Liu, X.; Wang, F.; Qu, Z.; Ge, Z.; Narayanan, R. P.; Williams, D.; et al. Programming Nanoparticle Valence Bonds with Single-Stranded DNA Encoders. *Nat. Mater.* **2019**, 1–8.
(277) Ge, H.; Wang, D.; Pan, Y.; Guo, Y.; Li, H.; Zhang, F.; Zhu, X.; Li, Y.; Zhang, C.; Huang, L. Sequence-Dependent DNA Functionalization of Upconversion Nanoparticles and Their Programmable Assemblies. *Angew. Chem. Int. Ed.* **2020**, *59* (21), 8133–8137.
(278) Parvin, N.; Jin, Q.; Wei, Y.; Yu, R.; Zheng, B.; Huang, L.; Zhang, Y.; Wang, L.; Zhang, H.; Gao, M.; et al. Few-Layer Graphdiyne Nanosheets Applied for Multiplexed Real-Time DNA Detection. *Adv. Mater.* **2017**, *29* (18), 1606755.
(279) Sina, A. A. I.; Carrascosa, L. G.; Liang, Z.; Grewal, Y. S.; Wardiana, A.; Shiddiky, M. J. A.; Gardiner, R. A.; Samaratunga, H.; Gandhi, M. K.; Scott, R. J.; et al. Epigenetically Reprogrammed Methylation Landscape Drives the DNA Self-Assembly and Serves as a Universal Cancer Biomarker. *Nat. Commun.* **2018**, *9* (1), 4915.
(280) Wang, L.; Zhang, H.; Wang, C.; Xu, Y.; Su, J.; Wang, X.; Liu, X.; Feng, D.; Wang, L.; Zuo, X.; et al. Poly-Adenine-Mediated Spherical Nucleic Acids for Strand Displacement-Based DNA/RNA Detection. *Biosens. Bioelectron.* **2019**, *127*, 85–91.
(281) Georgakilas, V.; Tiwari, J. N.; Kemp, K. C.; Perman, J. A.; Bourlinos, A. B.; Kim, K. S.; Zboril, R. Noncovalent Functionalization of Graphene and Graphene Oxide for Energy Materials, Biosensing, Catalytic, and Biomedical Applications. *Chem. Rev.* **2016**, *116* (9), 5464–5519.
(282) Lee, J.; Yim, Y.; Kim, S.; Choi, M.-H.; Choi, B.-S.; Lee, Y.; Min, D.-H. In-Depth Investigation of the Interaction between DNA and Nano-Sized Graphene Oxide. *Carbon* **2016**, *97*, 92–98.

(283) Akca, S.; Foroughi, A.; Frochtzwajg, D.; Postma, H. W. C. Competing Interactions in DNA Assembly on Graphene. *PLOS ONE* **2011**, *6* (4), e18442.
(284) Hess, B.; Kutzner, C.; van der Spoel, D.; Lindahl, E. GROMACS 4: Algorithms for Highly Efficient, Load-Balanced, and Scalable Molecular Simulation. *J. Chem. Theory Comput.* **2008**, *4* (3), 435–447.
(285) Maier, J. A.; Martinez, C.; Kasavajhala, K.; Wickstrom, L.; Hauser, K. E.; Simmerling, C. Ff14SB: Improving the Accuracy of Protein Side Chain and Backbone Parameters from Ff99SB. *J. Chem. Theory Comput.* **2015**, *11* (8), 3696–3713.
(286) Jorgensen, W. L.; Chandrasekhar, J.; Madura, J. D.; Impey, R. W.; Klein, M. L. Comparison of Simple Potential Functions for Simulating Liquid Water. *J. Chem. Phys.* **1983**, *79* (2), 926–935.
(287) Stauffer, D.; Dragneva, N.; Floriano, W. B.; Mawhinney, R. C.; Fanchini, G.; French, S.; Rubel, O. An Atomic Charge Model for Graphene Oxide for Exploring Its Bioadhesive Properties in Explicit Water. *J. Chem. Phys.* **2014**, *141* (4), 044705.
(288) Wang, J.; Wolf, R. M.; Caldwell, J. W.; Kollman, P. A.; Case, D. A. Development and Testing of a General Amber Force Field. *J. Comput. Chem.* **2004**, *25* (9), 1157–1174.
(289) Darden, T.; York, D.; Pedersen, L. Particle Mesh Ewald: An N·log(N) Method for Ewald Sums in Large Systems. *J. Chem. Phys.* **1993**, *98* (12), 10089–10092.
(290) Li, S.; Olson, W. K.; Lu, X.-J. Web 3DNA 2.0 for the Analysis, Visualization, and Modeling of 3D Nucleic Acid Structures. *Nucleic Acids Res.* **2019**, *47* (W1), W26–W34.
(291) Wolski, P.; Nieszporek, K.; Panczyk, T. G-Quadruplex and I-Motif Structures within the Telomeric DNA Duplex. A Molecular Dynamics Analysis of Protonation States as Factors Affecting Their Stability. *J. Phys. Chem. B* **2019**, *123* (2), 468–479.
(292) Goh, G. B.; Knight, J. L.; Brooks, C. L. Constant PH Molecular Dynamics Simulations of Nucleic Acids in Explicit Solvent. *J. Chem. Theory Comput.* **2012**, *8* (1), 36–46.
(293) Yang, J.; Shi, G.; Tu, Y.; Fang, H. High Correlation between Oxidation Loci on Graphene Oxide. *Angew. Chem. Int. Ed.* **2014**, *53* (38), 10190–10194.
(294) Pawlak, R.; Vilhena, J. G.; Hinaut, A.; Meier, T.; Glatzel, T.; Baratoff, A.; Gnecco, E.; Pérez, R.; Meyer, E. Conformations and Cryo-Force Spectroscopy of Spray-Deposited Single-Strand DNA on Gold. *Nat. Commun.* **2019**, *10* (1), 685.
(295) Liñán-García, E.; Gallegos-Araiza, L. M. Simulated Annealing with Previous Solutions Applied to DNA Sequence Alignment. **2012**.
(296) Ma, H.; Xu, Z.; Fang, H.; Lei, X. Unexpected Sequence Adsorption Features of Polynucleotide SsDNA on Graphene Oxide. *Phys. Chem. Chem. Phys.* **2020**, *22* (20), 11740–11746.
(297) Huang, Z.; Liu, B.; Liu, J. Parallel Polyadenine Duplex Formation at Low PH Facilitates DNA Conjugation onto Gold Nanoparticles. *Langmuir* **2016**, *32* (45), 11986–11992.
(298) Huang, P.-J. J.; Kempaiah, R.; Liu, J. Synergistic PH Effect for Reversible Shuttling Aptamer-Based Biosensors between Graphene Oxide and Target Molecules. *J. Mater. Chem.* **2011**, *21* (25), 8991–8993.
(299) Zhang, F.; Liu, B.; Lopez, A.; Wang, S.; Liu, J. Opposite Salt-Dependent Stability of i-Motif and Duplex Reflected in a Single DNA Hairpin Nanomachine. *Nanotechnology* **2020**, *31* (19), 195503.
(300) Park, J. S.; Na, H.-K.; Min, D.-H.; Kim, D.-E. Desorption of Single-Stranded Nucleic Acids from Graphene Oxide by Disruption of Hydrogen Bonding. *Analyst* **2013**, *138* (6), 1745–1749.

(301) He, S.; Yu, J.; Wang, F.; Tian, L. Well-Optimized Conjugated GO-DNA Nanosystem for Sensitive Ratiometric PH Detection in Live Cells. *Langmuir* **2019**, *35* (42), 13745–13752.
(302) Lakowicz, J. R. *Principles of Fluorescence Spectroscopy*, 3rd ed.; Springer US, 2006.
(303) Choi, J.-W.; Kang, D.-K.; Park, H.; deMello, A. J.; Chang, S.-I. High-Throughput Analysis of Protein–Protein Interactions in Picoliter-Volume Droplets Using Fluorescence Polarization. *Anal. Chem.* **2012**, *84* (8), 3849–3854.
(304) Lundblad, J. R.; Laurance, M.; Goodman, R. H. Fluorescence Polarization Analysis of Protein-DNA and Protein-Protein Interactions. *Mol. Endocrinol. Baltim. Md* **1996**, *10* (6), 607–612.
(305) Choi, J.-W.; Jo, B.-G.; deMello, A. J.; Choo, J.; Kim, H. Y. Streptavidin-Triggered Signal Amplified Fluorescence Polarization for Analysis of DNA–Protein Interactions. *Analyst* **2016**, *141* (24), 6499–6502.
(306) Anderson, B. J.; Larkin, C.; Guja, K.; Schildbach, J. F. Using Fluorophore-Labeled Oligonucleotides to Measure Affinities of Protein-DNA Interactions. *Methods Enzymol.* **2008**, *450*, 253–272.
(307) Wang, L.; Tian, J.; Huang, Y.; Lin, X.; Yang, W.; Zhao, Y.; Zhao, S. Homogenous Fluorescence Polarization Assay for the DNA of HIV A T7 by Exploiting Exonuclease-Assisted Quadratic Recycling Amplification and the Strong Interaction between Graphene Oxide and SsDNA. *Microchim. Acta* **2016**, *183* (7), 2147–2153.
(308) Yu, Y.; Liu, Y.; Zhen, S. J.; Huang, C. Z. A Graphene Oxide Enhanced Fluorescence Anisotropy Strategy for DNAzyme-Based Assay of Metal Ions. *Chem. Commun.* **2013**, *49* (19), 1942–1944.
(309) Zhen, S. J.; Yu, Y.; Li, C. M.; Huang, C. Z. Graphene Oxide Amplified Fluorescence Anisotropy for Label-Free Detection of Potassium Ion. *Analyst* **2014**, *140* (1), 353–357.
(310) Liang, S.; He, G.; Tian, J.; Zhao, Y.; Zhao, S. Fluorescence Polarization Gene Assay for HIV-DNA Based on the Use of Dendrite-Modified Gold Nanoparticles Acting as Signal Amplifiers. *Microchim. Acta* **2018**, *185* (2), 119.
(311) Ye, B.-C.; Yin, B.-C. Highly Sensitive Detection of Mercury(II) Ions by Fluorescence Polarization Enhanced by Gold Nanoparticles. *Angew. Chem. Int. Ed.* **2008**, *47* (44), 8386–8389.
(312) Chen, Z.; Li, H.; Jia, W.; Liu, X.; Li, Z.; Wen, F.; Zheng, N.; Jiang, J.; Xu, D. Bivalent Aptasensor Based on Silver-Enhanced Fluorescence Polarization for Rapid Detection of Lactoferrin in Milk. *Anal. Chem.* **2017**, *89* (11), 5900–5908.
(313) Zhao, J.; Chu, Z.; Jin, X.; Zhao, S. A Fluorescence Polarization Assay for Nucleic Acid Based on the Amplification of Hybridization Chain Reaction and Nanoparticles. *Sens. Actuators B Chem.* **2015**, *209*, 116–121.
(314) Qi, L.; Yan, Z.; Huo, Y.; Hai, X.-M.; Zhang, Z.-Q. MnO2 Nanosheet-Assisted Ligand-DNA Interaction-Based Fluorescence Polarization Biosensor for the Detection of Ag+ Ions. *Biosens. Bioelectron.* **2017**, *87*, 566–571.
(315) Gao, Y.; Xu, J.; Li, B.; Jin, Y. Nanoparticle-Aided Amplification of Fluorescence Polarization for Ultrasensitively Monitoring Activity of Telomerase. *ACS Appl. Mater. Interfaces* **2016**, *8* (22), 13707–13713.
(316) Chen, J.; Chen, Q.; Gao, C.; Zhang, M.; Qin, B.; Qiu, H. A SiO2 NP–DNA/Silver Nanocluster Sandwich Structure-Enhanced Fluorescence Polarization Biosensor for Amplified Detection of Hepatitis B Virus DNA. *J. Mater. Chem. B* **2015**, *3* (6), 964–967.

(317) Chen, J.; Liu, J.; Chen, X.; Qiu, H. Recent Progress in Nanomaterial-Enhanced Fluorescence Polarization/Anisotropy Sensors. *Chin. Chem. Lett.* **2019**.
(318) Liu, J.; Wang, C.; Jiang, Y.; Hu, Y.; Li, J.; Yang, S.; Li, Y.; Yang, R.; Tan, W.; Huang, C. Z. Graphene Signal Amplification for Sensitive and Real-Time Fluorescence Anisotropy Detection of Small Molecules. *Anal. Chem.* **2013**, *85* (3), 1424–1430.
(319) Ye, H.; Lu, Q.; Duan, N.; Wang, Z. GO-Amplified Fluorescence Polarization Assay for High-Sensitivity Detection of Aflatoxin B1 with Low Dosage Aptamer Probe. *Anal. Bioanal. Chem.* **2019**, *411* (5), 1107–1115.
(320) Liu, B.; Salgado, S.; Maheshwari, V.; Liu, J. DNA Adsorbed on Graphene and Graphene Oxide: Fundamental Interactions, Desorption and Applications. *Curr. Opin. Colloid Interface Sci.* **2016**, *26*, 41–49.
(321) Lu, C.-H.; Yang, H.-H.; Zhu, C.-L.; Chen, X.; Chen, G.-N. A Graphene Platform for Sensing Biomolecules. *Angew. Chem. Int. Ed.* **2009**, *48* (26), 4785–4787.
(322) Liu, M.; Song, J.; Shuang, S.; Dong, C.; Brennan, J. D.; Li, Y. A Graphene-Based Biosensing Platform Based on the Release of DNA Probes and Rolling Circle Amplification. *ACS Nano* **2014**, *8* (6), 5564–5573.
(323) Dubertret, B.; Calame, M.; Libchaber, A. J. Single-Mismatch Detection Using Gold-Quenched Fluorescent Oligonucleotides. *Nat. Biotechnol.* **2001**, *19* (4), 365–370.
(324) Liu, B.; Liu, J. Methods for Preparing DNA-Functionalized Gold Nanoparticles, a Key Reagent of Bioanalytical Chemistry. *Anal. Methods* **2017**, *9* (18), 2633–2643.
(325) Maxwell, D. J.; Taylor, J. R.; Nie, S. Self-Assembled Nanoparticle Probes for Recognition and Detection of Biomolecules. *J. Am. Chem. Soc.* **2002**, *124* (32), 9606–9612.
(326) Lu, C.; Liu, Y.; Ying, Y.; Liu, J. Comparison of MoS2, WS2, and Graphene Oxide for DNA Adsorption and Sensing. *Langmuir* **2017**, *33* (2), 630–637.
(327) Liu, B.; Liu, J. Comprehensive Screen of Metal Oxide Nanoparticles for DNA Adsorption, Fluorescence Quenching, and Anion Discrimination. *ACS Appl. Mater. Interfaces* **2015**, *7* (44), 24833–24838.
(328) Wang, H.; Yang, R.; Yang, L.; Tan, W. Nucleic Acid Conjugated Nanomaterials for Enhanced Molecular Recognition. *ACS Nano* **2009**, *3* (9), 2451–2460.
(329) Prigodich, A. E.; Randeria, P. S.; Briley, W. E.; Kim, N. J.; Daniel, W. L.; Giljohann, D. A.; Mirkin, C. A. Multiplexed Nanoflares: MRNA Detection in Live Cells. *Anal. Chem.* **2012**, *84* (4), 2062–2066.
(330) Liu, Z.; Liu, B.; Ding, J.; Liu, J. Fluorescent Sensors Using DNA-Functionalized Graphene Oxide. *Anal. Bioanal. Chem.* **2014**, *406* (27), 6885–6902.
(331) Tan, L. H.; Xing, H.; Lu, Y. DNA as a Powerful Tool for Morphology Control, Spatial Positioning, and Dynamic Assembly of Nanoparticles. *Acc. Chem. Res.* **2014**, *47* (6), 1881–1890.
(332) Ma, J.-L.; Yin, B.-C.; Wu, X.; Ye, B.-C. Simple and Cost-Effective Glucose Detection Based on Carbon Nanodots Supported on Silver Nanoparticles. *Anal. Chem.* **2017**, *89* (2), 1323–1328.
(333) Ameloot, M.; vandeVen, M.; Acuña, A. U.; Valeur, B. Fluorescence Anisotropy Measurements in Solution: Methods and Reference Materials (IUPAC Technical Report). *Pure Appl. Chem.* **2013**, *85* (3), 589–608.
(334) Martin, M. The PH Dependence of Fluorescein Fluorescence. *J. Lumin.* **1975**, *10*, 381–390.

(335) Peng, Z. G.; Hidajat, K.; Uddin, M. S. Selective and Sequential Adsorption of Bovine Serum Albumin and Lysozyme from a Binary Mixture on Nanosized Magnetic Particles. *J. Colloid Interface Sci.* **2005**, *281* (1), 11–17.
(336) Medda, L.; Monduzzi, M.; Salis, A. The Molecular Motion of Bovine Serum Albumin under Physiological Conditions Is Ion Specific. *Chem. Commun.* **2015**, *51* (30), 6663–6666.
(337) Kim, J.; Cote, L. J.; Kim, F.; Huang, J. Visualizing Graphene Based Sheets by Fluorescence Quenching Microscopy. *J. Am. Chem. Soc.* **2010**, *132* (1), 260–267.
(338) Yun, C. S.; Javier, A.; Jennings, T.; Fisher, M.; Hira, S.; Peterson, S.; Hopkins, B.; Reich, N. O.; Strouse, G. F. Nanometal Surface Energy Transfer in Optical Rulers, Breaking the FRET Barrier. *J. Am. Chem. Soc.* **2005**, *127* (9), 3115–3119.
(339) Becheru, D. F.; Vlăsceanu, G. M.; Banciu, A.; Vasile, E.; Ioniţă, M.; Burns, J. S. Optical Graphene-Based Biosensor for Nucleic Acid Detection; Influence of Graphene Functionalization and Ionic Strength. *Int. J. Mol. Sci.* **2018**, *19* (10), 3230.
(340) Tang, Z.; Wu, H.; Cort, J. R.; Buchko, G. W.; Zhang, Y.; Shao, Y.; Aksay, I. A.; Liu, J.; Lin, Y. Constraint of DNA on Functionalized Graphene Improves Its Biostability and Specificity. *Small* **2010**, *6* (11), 1205–1209.
(341) Shang, J.; Ma, L.; Li, J.; Ai, W.; Yu, T.; Gurzadyan, G. G. The Origin of Fluorescence from Graphene Oxide. *Sci. Rep.* **2012**, *2*, 792.
(342) Avakyan, N.; Conway, J. W.; Sleiman, H. F. Long-Range Ordering of Blunt-Ended DNA Tiles on Supported Lipid Bilayers. *J. Am. Chem. Soc.* **2017**, *139* (34), 12027–12034.